UNIVERSITY OF SCIENCE AND TECHNOLOGY OF CHINA

Hefei, CHINA

Higher Moments of Event-by-Event Net-proton Multiplicity Distributions in Ultra-relativistic Heavy Ion Collision

A dissertation submitted

for the degree of

Doctor of Philosophy in Physics

by

Xiaofeng Luo

Co-supervisors: Cheng Li, Hans Georg Ritter, Nu Xu

2011

Dedicated to my family

谨献给我的家人

ABSTRACT OF THE DISSERTATION

Higher Moments of Event-by-Event Net-proton Multiplicity Distributions in Ultra-relativistic Heavy Ion Collision

by

Xiaofeng Luo

Doctor of Philosophy in Physics

University of Science and Technology of China, Hefei, 2011

The strong interaction, one of the four fundamental forces found in the nature, confines the quarks and gluons in the hadrons. Quantum Chromodynamics (QCD), which can successfully explain plenty of physics phenomena, is believed to be the correct theory to describe the strong interaction. The phase structure of nuclear matter, described by strong interaction, can be demonstrated by QCD phase diagram, which is two dimensional diagram with parameters temperature (T) and baryon chemical potential (μ_B). A new form of matter-Quark Gluon Plasma (QGP) dominated by quark and gluon degree of freedom is believed to exist in the early Universe after few tens microseconds of Big Bang, when the energy density and temperature is extremely high. Finite temperature Lattice QCD calculations predict a smooth cross-over transition from hadronic phase to the Quarak Gluons Plasma (QGP) phase at high temperature and small μ_B region, and a first order phase transition at large μ_B region. The end point of the first order phase boundary toward the cross-over region is the so called QCD Critical Point (CP). Although many efforts have been made by theorist and experimentalist to locate the CP, its location or even existence is still not confirmed yet.

The Relativistic Heavy Ion Collider (RHIC) locating at Brookheaven Nation

Lab (BNL) can create hot dense nuclear matter by accelerating and colliding gold nuclei up to center of mass energy $\sqrt{s_{\mathrm{NN}}} = 200$ GeV per nucleon pair. It provides us an ideal experimental tool to explore the phase structure of nuclear matter and study the properties of QGP. After more than ten years' experimental study, there are strong evidences that the strongly coupled QGP has already been formed in the heavy ion collisions at top energy of RHIC, such as the hydrodynamic behavior and number of quarks scaling of the elliptic flow (v_2), comparable v_2 of multi-strange hadrons to the light hadrons, high p_T particle suppression-jet quenching.

Recently, it was found that the higher order fluctuation observables-higher moments (Variance (σ^2), Skewness (S), Kurtosis (κ)) of conserved quantities, such as net-baryon, net-charge, and net-strangeness, distributions can be directly connected to the corresponding thermodynamic susceptibilities in Lattice QCD and Hadron Resonance Gas (HRG) model. Theoretical calculations demonstrate that the experimental measurable net-proton (proton number minus anti-proton number) number fluctuations can effectively reflect the fluctuations of the net-baryon and net-charge number in heavy ion collision experiments. Thus, it is of great interest to measure the higher moments of event-by-event net-proton multiplicity distributions in the heavy ion collision experiment. It allows us to probe the bulk properties of the hot dense nuclear matter and test the QCD theory at non-perturbative domain, which is rarely tested by experiments. Meanwhile, model calculations demonstrate that the higher moments of net-proton distributions are also proportional to the higher power of the QCD critical point related correlation length (ξ). It motivates us to search for the QCD critical point with the higher moments of the net-proton distributions, experimentally, as a direct application of the higher moments observable. The experimental confirmation of the QCD critical point will largely improve our knowledge and understanding of properties of the nuclear matter at finite temperature as well as the QCD theory.

In this thesis, we have performed the world's first comprehensive and systematical measurements of the higher moments of event-by-event net-proton multiplicity distributions in heavy ion collision. It opens a completely new domain and effective way for probing the bulk properties of hot dense nuclear matter through the heavy ion collision experiments. Those higher moments are also used to search for the QCD critical point for the first time. It is indicated that the QCD critical point should not be in the $\mu_B < 200$ MeV region. On the other hand, by comparing the higher moments of net-proton distributions with the results from first principle Lattice QCD calculations, we can test the QCD theory in the non-perturbative domain and constrain fundamental parameters of the QCD. Based on this method, the scale for the QCD phase diagram, the transition temperature T_c at $\mu_B = 0$, for the first time, have been extracted from our experimental data. We conclude that the transition temperature T_c at $\mu_B = 0$, $T_c = 175^{+1}_{-7}$ MeV. This result has been published on *Science*.

In the year 2010 (Run 10), RHIC has started its Beam Energy Scan (BES) program and tuned the Au+Au collision energy from $\sqrt{s_{\mathrm{NN}}} = 39$ GeV down to 7.7 GeV with the corresponding μ_B coverage $112 < \mu_B < 410$ MeV. This allows us to access and probe broad region of the QCD phase diagram. The characteristic signatures for the appearance of QCD critical point are the non-monotonic dependence of the observations with the collision energy ($\sqrt{s_{\mathrm{NN}}}$). With our large uniform acceptance and good capability of particle identification STAR detector at RHIC, it provides us very good opportunities to find the QCD critical point with sensitive observable, if the existence of QCD critical point is true. In this thesis, we will present the world's first comprehensive and systematical measurements for the higher moments of net-proton distributions in the heavy ion collision. Specifically, those are the beam energy and system size dependence results for higher moment (σ, S, κ) as well as moment products ($\kappa\sigma^2, S\sigma$) of net-proton multiplicity distributions for Au+Au collisions at $\sqrt{s_{\mathrm{NN}}} = 200, 130, 62.4,$

39, 19.6, 11.5 and 7.7 GeV (including BES energies), Cu+Cu collisions at $\sqrt{s_{\text{NN}}}$ = 200, 62.4 and 22.4 GeV, d+Au collisions at $\sqrt{s_{\text{NN}}}$ = 200 GeV, p+p collisions at $\sqrt{s_{\text{NN}}}$ = 200 and 62.4 GeV.

To ensure the purity and similar efficiency, the protons and anti-protons are identified with the ionization energy loss (dE/dx) measured by Time Projection Champer (TPC) of STAR detector within $0.4 < p_T < 0.8$ GeV/c and mid-rapidity ($|y| < 0.5$). It was found that the centrality dependence of various moments (M, σ, S, κ) are consistent with the expectations evaluated from Central Limit Theorem (CLT) by assuming superposition of many independent emission sources. Meanwhile, the volume independent baryon number susceptibility ratio can be related to the moment products of net-proton number distributions as $\kappa\sigma^2 = \chi_B^{(4)}/\chi_B^{(2)}$ and $S\sigma = \chi_B^{(3)}/\chi_B^{(2)}$. The measured moment product $\kappa\sigma^2$ shows no centrality dependence while the $S\sigma$ shows a weak centrality dependence. The energy dependence of the $\kappa\sigma^2$ and $S\sigma$ for Au+Au central collisions are compared with the Lattice QCD and HRG model calculations within grand canonical ensemble framwork. At high energy (200, 130 and 62.4 GeV), the $\kappa\sigma^2$ and $S\sigma$ of net-proton distributions are consistent with Lattice QCD and HRG model calculations while smaller than HRG model calculations at energies $\sqrt{s_{\text{NN}}}$ = 39, 19.6 , 11.5 and 7.7 GeV. Recent model calculations demonstrate that the $\kappa\sigma^2$ value will be always smaller than its Poisson statistical expectation value 1, when the QCD critical point is approached from the high energy cross-over side. The $\kappa\sigma^2$ from Lattice QCD calculations at 19.6 GeV shows negative value while the experimental results of 19.6 GeV are with large errors due to the limited statistics. Fortunately, this trend can be confirmed soon by Run11 19.6 GeV data with higher statistics. The Time-Of-Flight (TOF) detector is also used to identify proton and anti-proton at higher p_T, this allows us to study the phase space (p_T, y) coverage dependence of our observables.

Whether the matter created in the heavy ion collision is thermalization or

not, is a long standing question. The $S\sigma$ of net-proton distributions is found to be related to the thermodynamics parameters of T, μ_B in the grand canonical ensemble description of the collision system, as $S\sigma = tanh(\mu_B/T)$. The $S\sigma$ also scale with mid-rapidity charged particle density $(dN_{ch}/d\eta)$ and the collision energy $(\sqrt{s_{NN}})$ with a double power law form. This in turn predicts the similar scaling properties of μ_B/T ratio, which is confirmed by the μ_B/T extracted from the thermal model fits of measured particle ratios. The particle yields and fluctuations in heavy ion collision can be seen as two sides of coin. The mutual agreements between the μ_B/T extracted from thermal model fits of particle ratio and from the event-by-event fluctuation observable $S\sigma$ of net-proton distributions provides a further evidence of thermalization of the matter created in the heavy ion collisions.

Finally, let's summarize three new results for the higher moments of net-proton distributions obtained in the heavy ion collision experiment.

1. First time, those higher moments of net-proton distributions are used to search for the QCD critical point in the heavy ion collision experiments. It is observed that the moment products $\kappa\sigma^2$ and $S\sigma$ of net-proton distributions for Au+Au collisions are consistent with Lattice QCD and HRG model calculations at high energy 200, 130 and 62.4 GeV, while deviating from the HRG model expectations at 39, 19.6, 11.5 and 7.7 GeV. Those deviations could potentially be related to chiral phase transition and QCD critical point. For $\kappa\sigma^2$, the Lattice QCD calculations at 19.6 GeV shows negative value while the experimental results of 19.6 GeV are with large errors due to the limited statistics. Fortunately, this ambiguity can be clarified soon by Run11 19.6 GeV data with higher statistics.

2. First time, the thermalization issue in heavy ion collision is addressed with the higher moments of net-proton number distributions measurement. The

results strongly support the thermalization of the matter created in the high energy heavy ion collisions.

3. First time, the transition temperature T_c at $\mu_B = 0$ for the QCD phase diagram is determined by comparing our experimental higher order net-proton fluctuations with first principle Lattice QCD calculations. This temperature is a basic scale for QCD phase diagram. It opens a new domain for probing the bulk properties of nuclear matters and find a new method to test the QCD theory at non-perturbative region. This research has been published in *Science*.

The experimental study of higher moments of net-proton distributions in heavy ion collisions open a new domain and provide an effective way for probing the bulk properties of nuclear matter. Thus, it is of great significance for nuclear physics and heavy ion collision physics research.

极端相对论重离子碰撞中逐事件
净质子数分布的高阶矩测量

罗晓峰

中国科学技术大学

摘　要

自然界中四大基本作用力的强相互作用把夸克和胶子禁闭在强子中。能成功解释许多物理现象的量子色动力学(QCD)被人们认为是描述强相互作用的正确理论。强相互作用描述的核物质的相结构可以用二维QCD相图表示，纵坐标参数是温度(T)，横坐标是重子化学势(μ_B)。由自由夸克和胶子自由度组成的夸克胶子等离子体(QGP) 被人们认为存在于宇宙大爆炸以后几十微秒的能量密度和温度都极高的早期宇宙。格点QCD预言在高温低重子密度区域发生的从强子物质到夸克胶子等离子体的相变是平滑穿越，然而在高重子密度区域发生的相变是一阶相变。这个一阶相变边界有一个终点，这个终点是一个QCD二阶相变临界点，被简称为QCD 临界点(QCD Critical Point)，同时它也是穿越区的起点。尽管理论家和实验家做过许多努力去标定这个相变临界点的位置，但是它的位置甚至是存在性始终没有被确定。

布鲁克海汶国家实验室(BNL)的相对论重离子对撞机(RHIC)通过加速重离子以及让它们每对核子以上限200 GeV的质心能量对撞,产生出高温高密的核物质。这给我们提供了理想的实验工具去研究QCD相结构和夸克胶子等离子体的性质. 在进行了大约十多年研究之后，RHIC实验上发现了许多证明强耦合夸克胶子等离子已经实现的证据，比如：椭圆流(v_2) 的流体行为以及夸克数标度，数量级与轻强子椭圆流可比拟的多奇异强子椭圆流以及高横动量(p_T)粒子产额压低-喷注淬火现象。

最近，一系列研究发现高阶涨落-守恒量，例如重子数，电荷数和奇异数，

分布的高阶矩 (方差(σ^2),偏度(S),峰度(κ)) 能够直接与相应的格点QCD和强子共振气体模型的热力学感受(Susceptibility)系数联系起来。理论计算表明实验可观测的净质子数（质子数减去反质子数）的涨落能够很好的反应出净重子数和净电荷数的涨落。这样使得从实验上探测高温高密核物质的整体性质以及检验QCD非微扰区域成为可能。同时，理论模型计算表明，净质子数分布的高阶矩正比于QCD临界点相关的关联长度(ξ)的高阶指数，比如三阶累积量 $<(\delta N)^3>\sim \xi^{4.5}$ 和四阶累积量 $<(\delta N)^4>-3<(\delta N)^2>^2\sim \xi^7$)。高阶矩观测量对关联长度的高灵敏度启发我们，可以通过将净质子数分布的高阶矩测量直接应用到核物质的QCD临界点的寻找。QCD临界点的实验确认能够大大的增进人们对有限温度下核物质性质以及QCD理论的理解和认识。因此在高能重离子对撞实验中开展净质子数分布的高阶矩测量对研究高温高密核物质的性质有着重大的科学意义。

在这篇论文中，首次在高能重离子对撞实验中对净质子数分布的高阶矩进行了全面系统地测量。这项研究开创了通过重离子对撞实验来探测高温高密核物质的整体性质的全新领域和有效方法。并且首次将净质子数分布的高阶矩测量直接应用到核物质相变中QCD临界点的寻找，研究结果表明QCD临界点存在于重子化学势大于200 MeV区域，相应的研究成果已经发表在美国物理学会物理评论快报上，并获得了国际同行的高度认可。另一方面，通过将实验数据与第一性原理格点QCD计算结果比较，能够检验QCD理论在非微扰区域的性质以及给出QCD基本参数的限制。通过这种方法，在世界上首次直接从净质子数分布的高阶矩的实验测量中确定了QCD相图的标度，也就是在零重子化学势下对应的相变穿越温度$T_c = 175^{+1}_{-7}$ MeV，从实验数据提取得到的这个相变穿越温度与格点QCD理论计算得到温度符合得很好，相应研究成果已经被发表在《科学》杂志上。

在2010年(Run 10)，RHIC已经启动了它的能量扫描计划，它将金金碰撞的能量从39 GeV降低到7.7 GeV，对应的重子化学势覆盖范围是$112 < \mu_B < 410$ MeV。这样使得我们能够访问和探测到QCD相图中比较宽广的区域。QCD临界点出现的特征信号是对碰撞能量的非单调依赖行为。如果QCD临界点

真实存在于自然界中，那么在具有均匀大接受度以及好的粒子鉴别能力的RHIC中的STAR探测器上，将有很好的机会利用灵敏的探针在重离子对撞实验中发现QCD临界点。这篇论文中，在世界上首次对净质子数分布的各阶矩(M, σ^2, S, κ)以及矩乘积$(\kappa\sigma^2, S\sigma)$对能量以及系统大小的依赖进行系统地测量。这些碰撞系统包括金金碰撞，质心碰撞能量分别是$\sqrt{s_{\text{NN}}} = 200, 130,$ 62.4, 39, 19.6, 11.5 和 7.7 GeV (包含能量扫描的3个能量点)，铜铜碰撞，$\sqrt{s_{\text{NN}}}$ = 200, 62.4 和 22.4 GeV，氘金碰撞，$\sqrt{s_{\text{NN}}}$ = 200 GeV，以及质子质子碰撞，$\sqrt{s_{\text{NN}}}$ = 200 和 62.4 GeV。

为了保证质子和反质子的纯度和相似的探测效率，我们利用STAR探测器上的时间投影室(TPC)测量到的电离能损来鉴别横动量范围在 $0.4 < p_T < 0.8$ GeV/c 以及中心快度区域$(|y| < 0.5)$的质子和反质子。研究发现各阶矩 (M, σ, S, κ) 的碰撞中心度依赖符合中心极限定理(CLT)的预期结果(在多独立发射源假设下)。同时，体积无关的重子感受(Susceptibility)系数比可以和实验中的净质子数分布的高阶矩乘积联系起来$(\kappa\sigma^2 = \chi_B^{(4)}/\chi_B^{(2)}$ 和 $S\sigma = \chi_B^{(3)}/\chi_B^{(2)})$。实验上观测到矩乘积 $\kappa\sigma^2$ 没有显示出碰撞中心度依赖，然而 $S\sigma$ 有弱的碰撞中心度依赖性。在金金中心碰撞中，矩乘积的能量依赖显示，在高能量区 (200, 130 和 62.4 GeV) 矩乘积 $\kappa\sigma^2$ 和 $S\sigma$ 与格点QCD和强子共振气体模型的结果一致，然而在能量点39，19.6，11.5 和 7.7 GeV，它们偏离强子共振气体模型的预期结果。最近基于线性 σ 模型计算显示，当QCD临界点被从高能的平滑穿越区逼近的时候，矩乘积 $\kappa\sigma^2$ 将会一直小于它的泊松统计的期望值1。对$\kappa\sigma^2$，格点QCD在19.6 GeV能量点计算得到的结果是负值，然而由于有限的事件量，实验结果具有较大的误差。幸运的是，这个不确定性可以很快被Run 11的19.6 GeV大统计量数据澄清。飞行时间探测器(TOF)被用来鉴别高横动量的质子与反质子，这样可以研究观测量的相空间依赖。

高能重离子碰撞中系统的热化与否是一个长期被关注的问题，但是始终没有最终的结论。碰撞中产生物质的热化被认为是在高能重离子碰撞中形成夸克胶子等离子体的两个必要条件之一，另外一个是夸克的解禁闭。通过研究发现净质子数分布的矩乘积 $S\sigma$ 与用热力学巨正则系综描述碰撞系统时用到的

13

热力学参数能够直接关联起来：$S\sigma = tanh(\mu_B/T)$，并且它对中心快度电荷密度$(dN_{ch}/d\eta)$和碰撞能量的依赖关系有指数形式的标度。这个标度接下来就可以预言热力学参数比μ_B/T也同样具有相似的标度性质，这个已经被从热模型拟合实验观测粒子产额得到的热力学参数所验证。重离子碰撞中粒子产额和涨落可以看作是一个硬币的两面。从热模型提取出来的热力学参数比μ_B/T与从涨落观测量$S\sigma$提取出来的比互相吻合给重离子碰撞中产生出来的热密介质的热化假设提供了一个有力的证据。同时，实验结果与格点QCD理论计算结果的一致也为系统的热化提供了进一步的证据。

论文详细描述了对高能重离子对撞实验中净质子数的数据处理和计算方法,特别是对净质子数分布的高阶矩的分析获得了三个最新研究结果。

1. 首次将其应用到高能重离子对撞实验中寻找QCD临界点，观察到金金碰撞中的高能量点200，130 和 62.4 GeV实验结果与格点QCD和热模型计算结果符合，但是在能量点39，19.6，11.5 和 7.7 GeV，实验结果偏离热模型的预期值。这个偏离可能与QCD手征相变和QCD临界点有关。同时，格点QCD在19.6 GeV能量点计算得到的$\kappa\sigma^2$结果为负值，然而STAR/RHIC实验Run 2, 19.6 GeV的实验结果由于统计量小而具有较大的误差。这个不确定性可以很快被Run 11的大统计量19.6 GeV数据澄清。

2. 首次将其应用到碰撞系统的热化问题研究上，得到的结果强有力的支持了高能量重离子对撞系统的热化假设。

3. 首次将实验分析得到的净质子分布高阶矩结果用于验证非微绕QCD理论，并通过对实验数据和格点QCD的比较确定了QCD相图的一个重要标度-在零重子化学势下的相变温度T_c。我们得出的结论是$T_c = 175^{+1}_{-7}$ MeV。这个穿越温度是强相互作用物质的一个重要基本参数。这个研究成果已经发表在《科学》杂志。

高能重离子碰撞中净质子数分布的高阶矩测量为探测核物质整体性质开创

了一个全新的研究领域以及提供了有效的研究方法。对高能重离子碰撞物理以及核物理研究有着重大的科学意义。

TABLE OF CONTENTS

LIST OF FIGURES

21

LIST OF TABLES

CHAPTER 1

Introduction

1.1 Quantum Chromodynamics

During million years of evolution, human beings are always questing for the secretes of nature. One of the most fundamental questions is what is the ultimate building blocks of the matter as well as their interaction mechanisms. In the past hundred years, there were several milestones of our knowledge about this fundamental question, such as the discovery of the internal structure of atom consisting of atomic nuclus and electrons [1]. Then, the aomic nuclus was found to be composed of the nucleons (proton and neutron), which are bounded together with short-range strong interaction [2]. By performing the Deep inelastic scattering (DIS) experiment in the late 1960's, we found that the hadrons also have internal structure and constituents, the so called partons [3]. Hence, the quark parton model was in turn built up to describe the composition of the hadrons, in which the quarks are the constituents and gluons propagate the interactions between quarks. The interactions between those partons are through the so called strong interaction, which is one of the four fundamental interactions discovered in the nature: Gravity, electro-magnetic, weak and strong interactions. Quantum Chrmodynamics (QCD) introduced by Gell-Mann in 1972 [4] is devoleped to describe the strong interaction, which is one of the two parts of the Standard Model theory of particle physics. The other one is so called the eletroweak theory, in which the electro-magnetic and weak interactions can be described in a unified way.

QCD [5] is a renomalizable non-abelian gauge theory based on the $SU(3)_C$ group. The subscript C denotes the quantum number - color, which is an exact symmetry. Quarks belong to a color triplet representation in this symmetry while the hadronic states are assumed to be color singlets in QCD. There are three different charges ("colors"): red, green and blue, compared to only one charge (electric) in quantum electrodynamics (QED)-the gauge theory describing electromagnetic interaction. Due to the non-abelian character of the $SU(3)_C$ group, the invariant QCD Lagrangian requires gauge (gluon) self-interactions, which do not appear in QED. There are eight different gluons, and the gluon exchange can change the color of a quark but not its flavor. Multi-gluons, such as 3 or 4 gluons interactions, are allowed in QCD. The most of the two basic properties of the QCD theory are: 1) Asymptotic freedom; and 2) Confinement.

1.1.1 Asymptotic Freedom

The strong interaction between quarks and gluons at large distances and asymptotic freedom at short distance are the two remarkable features of QCD, called asymptotic freedom, discovered by Gross, Politzer and Wilczek in 1973 [6]. According to the behavior of short distance and large distance, the static QCD potential can be described as:

$$V_s = -\frac{4}{3} \times \frac{\alpha_s}{r} + k \times r \qquad (1.1)$$

, where the first term dominating at small distance, arises from single-gluon exchange, similar to the Coulomb potential between two charges in QED, while the second term is presumably linked to the confinement of quarks and gluons inside hadrons.

The renormalized effective QCD coupling $\alpha_s(\mu) = g_s^2/4\pi$ depends on the renormalization scale (running coupling), similar to that in QED. However,

the QED running coupling increases with energy scale, while the gluon self-interactions lead to a completely different behavior in QCD. The running coupling constant $\alpha_s(\mu)$ can be written as:

$$\alpha_s(\mu) \equiv \frac{g_s^2(\mu)}{4\pi} \approx \frac{4\pi}{\beta_0 \ln(\mu^2/\Lambda_{QCD}^2)} \tag{1.2}$$

, where μ is momentum transfer scale, $\beta_0 = (11 - \frac{2}{3}n_f)$ is a constant dependent on the number of quark flavors with mass less than μ and Λ_{QCD} is called the QCD scale, which has to be determined experimentally. When $\beta_0 > 0$, this solution illustrates the asymptotic freedom property: $\alpha_s \to 0$ as $\mu \to \infty$, which means QCD can be calculated perturbatively in high momentum transfer or short distance approach (pQCD). On the other hand, this solution also shows strong coupling at $\mu \sim \Lambda_{QCD}$, so QCD is non-perturbative in this case. α_s needs to be determined from experiment. Due to the asymptotic freedom, the QCD is calculated with different methods at different energy scale. The QCD can only be calculated in pQCD, where requires the high momentum transfer or short distance approach. In the strong coupling case, pQCD is irrelevant and some other methods are needed, for example Lattice QCD and AdS/CFT. The world averaged α_s at the fixed-reference $\mu_0 = M_Z$ is $\alpha_s(M_Z) = 0.1184 \pm 0.0007$ [7], and the QCD scale $\Lambda_{QCD} = 200^{+25}_{-23}$ MeV. Fig. 1.1 shows the averaged α_s at different momentum transfer scale μ compared with Lattice QCD calculations.

1.1.2 Perturbative QCD (pQCD)

Physics quantities, such as cross sections, can be calculated by a truncated power series with respect to the running coupling constant α_s (α_s^{n+2}), at sufficiently high momentum transfer scale μ, where the α_s is sufficiently small. The lowest order term $(n = 0)$, which is so called Leading Order (LO) term, is with largest contributions to the physics process. For higher order term with $n = 1$
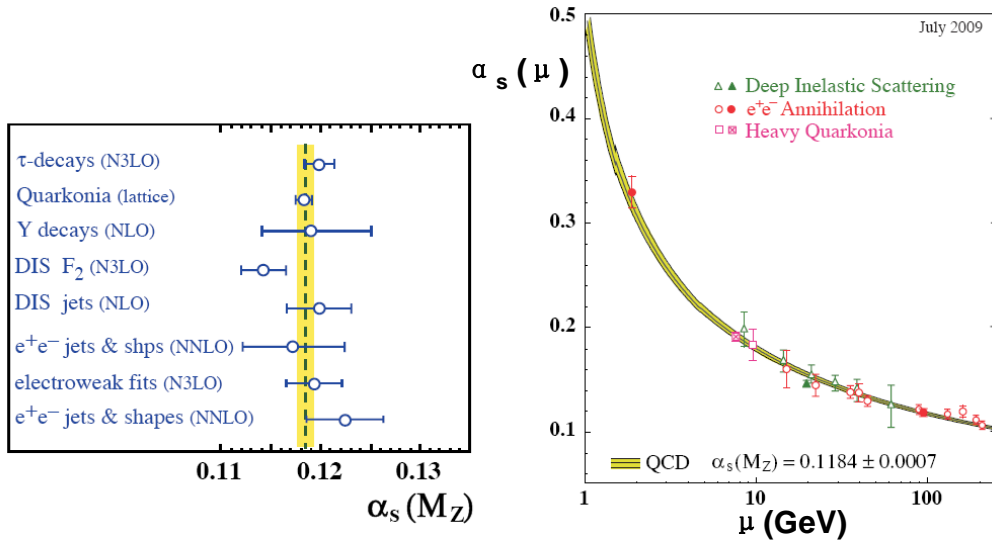
Figure 1.1: Left: Summary of measurements of $\alpha_s(M_Z)$ from different experiments; Right: α_s as a function of the energy scale μ obtained from Lattice QCD calculations (shadow lines) and experiments (markers) . The figures are taken from [7].

and $n = 2$ are called Next-to-Leading-Order (NLO) and Next-Next-to-Leading-Order (NNLO), respectively. Those higher order terms ($n \geq 1$) usually have small contributions and more complicated Feynman diagrams. There are plenty of experiments on high energy processes which can provide quantitative tests of pQCD.

The calculations are more complicated and difficult when pQCD is applied at the hadron level due to the non-perturbative nature of hadron structure. The so called QCD factorization theorem has been devoleped to calculate the cross section on hadron level, which separate the cross section into 2 parts: the process dependent parton cross section calculated by pQCD, and the universal long distance functions. For example, by assuming factorization, we can calculate the cross section of a process $A + B \rightarrow C + ...$ as:

$$\sigma_{AB \rightarrow C} = f_{a/A}(x_a, \mu_F^2) f_{b/B}(x_b, \mu_F^2) \otimes \hat{\sigma}_{ab \rightarrow c}(\hat{s}, \mu_F^2, \mu_R^2, \alpha_s) \otimes D_{c \rightarrow C}(z, \mu_F^2) \quad (1.3)$$

, where the middle term $\hat{\sigma}_{ab\to c}$ can be calculated in pQCD from Feynman diagrams. The first term $f_{a/A}(x_a, \mu_F^2)$ or $f_{b/B}(x_b, \mu_F^2)$ is the hadron Parton Distribution Function (PDF) and the last term $D_{c\to C}(z, \mu_F^2)$ is the Fragmentation Function (FF) which describes the process from a parton to a hadron. For leptons, those two terms do not contribute in this formula. Hence, we can measure PDFs through lepton-nucleon DIS interactions and FFs through high energy e^+e^- collisions. μ_R is the renormalization scale, originating from the need to regularize divergent momentum integrals in calculating high order diagram loops. μ_F is the factorization scale, at which the parton densities are evaluated. $\hat{s}$ is the partonic center of mass energy squared. From this formula, we find that it is complicated to determine the expected hadron production cross section in hadron-hadron collisions and certainly in heavy ion collisions.

1.1.3 Lattice QCD

Lattice QCD [8] is a well-established non-perturbative approach to solve the QCD theory of quarks and gluons exactly from first principles and without any assumptions. It is a lattice gauge theory formulated on a grid or lattice of points in space and time. Most importantly, lattice QCD provides a framework for investigation of non-perturbative phenomena such as confinement and quark-gluon plasma formation, which are intractable by means of analytic field theories.

At low momentum transfer, the QCD coupling constant α_s approaches unity quickly as the momentum transfer decreases. In this case the high order processes will have large contributions and can not be neglected. In Lattice QCD, space time is represented not as continuous but as a crystalline lattice, vertices connected by lines. Quarks may reside only on vertices and gluons can only travel along lines. As the spacing between vertices is reduced to zero, the theory will approach continuum QCD. Lattice QCD calculations often involved analysis at different lattice spacing to determine the lattice-spacing dependence, which

can then be extrapolated to the continuum. On the other hand, the calculation power is limited, which requires a smart use of the available resources. One needs to choose an action which gives the best physical description of the system, with minimum errors, using the available computational power. The limited computer resources force one to use physical constants which are different from their true physical values, such as quark masses are steadily going down, but to-date they are typically too high with respect to the real value.

1.1.4 Confinement and Chiral Symmetry Breaking

Confinement is the physics phenomenon that color charged particles, such as quarks, cannot be isolated, and therefore cannot be directly observed. Intuitively, confinement is due to the force-carrying gluons having color charge. As any electrically-charged particles separate, the electric fields between them diminish quickly, allowing electrons to become unbound from atomic nuclei. However, as two quarks separate, the gluon fields form narrow tubes (or strings) of color charge, which tend to bring the quarks together as though they were some kind of rubber band. This is quite different in behavior from electrical charge. Because of this behavior, the color force experienced by the quarks in the direction to hold them together, remains constant, regardless of their distance from each other. The color force between quarks is large, even on a macroscopic scale, being on the order of 100,000 newtons. As discussed above, it is constant, and does not decrease with increasing distance after a certain point has been passed. In Fig. 1.2, when two quarks become separated, at some point it is more energetically favorable for a new quark – antiquark pair to spontaneously appear, than to allow the tube to extend further. As a result of this, when quarks are produced in particle accelerators, instead of seeing the individual quarks in detectors, scientists see particle-antiparticle pairs or "jets" of many color-neutral particles (mesons and baryons), clustered together. This process is called hadronization,

fragmentation, or string breaking, and is one of the least understood processes in particle physics.
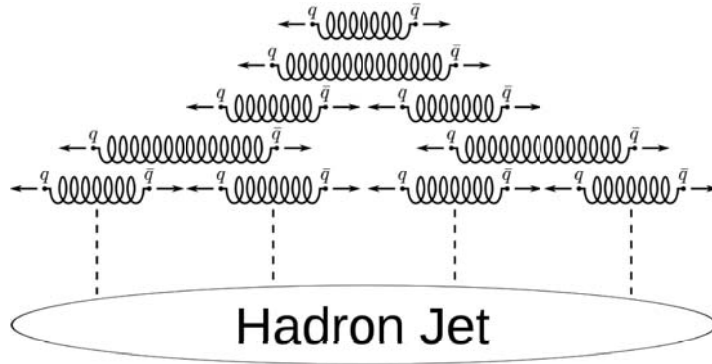
Figure 1.2: Schematic of quark confinement. The color force favors confinement because at a certain range it is more energetically favorable to create a quark-antiquark pair than to continue to elongate the color flux tube. The picture is from [9].

In the absence of quark masses, the QCD Lagrangian can be split into two independent sectors: the left- and right-handed components [10]. This Lagrangian is invariant under chiral symmetry transformations. This symmetry, which is the extension of classical $SU(3)$, is a global $SU_L(n_f) \times SU_R(n_f)$ symmetry for n_f massless quark flavors. However, it is spontaneously broken in the vacuum in the Nambu-Goldstone way to realize this symmetry. This breaking gives rise to $(n_f^2 - 1)$ massless Goldstone particles. Thus we can identify the π, K, η with the Goldstone modes of QCD: their small masses being generated by the quark-mass matrix which explicitly breaks the global chiral symmetry of the QCD Lagrangian.

1.2 QCD Phase Diagram and QCD Critical Point

Matter undergos phase transitions when external parameters such as the temperature (T), pressure (P) and/or the chemical potential (μ) are varied. The phase transition conditions can be in turn demonstrated in the phase diagram,

which can provide intrinsic knowledge on the phase structure of the matter and tells us how matter organize itself under external conditions given degrees of freedom. The phase structure of nuclear matter, described by strong interaction, can be demonstrated by QCD phase diagram, which is two dimensional diagram of parameters temperature (T) and baryon chemical potential (μ_B). Quantum chromodynamic (QCD) predicts that nuclear matter at high temperature and/or high baryon densities would make transition from a phase where quarks and gluons are confined and chiral symmetry is broken to a so called quark-gluon plasma (QGP) phase where quarks and gluons are de-confined and chiral symmetry is restored [11]. Finite temperature Lattice QCD calculations at baryon chemical potential equal to zero (μ_B=0) suggest a smooth cross-over above a critical point temperature [12, 13] $T_c \sim 170-190$ MeV from the hadronic phase to quark-gluon plasma phase [14]. At large μ_B, Lattice QCD and QCD based effective calculations indicate that the transition between hadronic and QGP phase is of first order [15]. The end point of the first order phase transition boundary towards the cross-over region is so called QCD Critical Point (CP) [16]. To explore the phase structure of the nuclear matter at extreme conditions, it is crucial for us to search for the QCD critical point and map the first order phase boundary, experimentally and theoretically [17].

1.2.1   QCD Phase Diagram

A phase diagram is a type of chart used to show conditions at which thermodynamically distinct phases can occur at equilibrium. The current conjecture of QCD phase diagram denoted by (T, μ_B) plane, which describes the phase structure of nuclear metter, is shown in Fig. 1.3. It contains information about the location of the phase boundaries (the phase transition is indicated by the orange band), hadronic gas phase (light blue) and quark-gluon plasma phase (QGP, navy). Calculations within Latticne QCD and QCD based effective mod-

els show that at large μ_B there is a first order hadronic-QGP phase transition. The phase boundary is expected to end in a critical point at finite μ_B. Current best estimates of the location of the critical point [18] is reflected in the position indicated in Fig. 1.3. Since lattice QCD computations agree with general symmetry arguments, which indicate that at $\mu_B=0$ the transition is a cross-over at critical temperature T_c. The fireball of bulk nuclear matter created in heavy ion collisions is initially out of equilibrium. However, the relative yields of different hadron species seem to be in thermal equilibrium. We assume that the fireball evolves from a non-equilibrium state to thermal equilibrium at chemical freeze-out, where the hadron inelastic interaction cease. By varying the colliding energy $(\sqrt{s_{\mathrm{NN}}})$ one traces out a line of chemical freeze-out in the phase diagram as shown in Fig. 1.3. This line can be parameterized through a hadron resonance gas model. The kinetic freeze-out line at which the elastic interactions between hadrons cease, is also shown in the QCD phase diagram.

RHIC beam energy scan program [19] can access a board region of the QCD phase diagram and give us good opportunity to search for the QCD critical point and map the first order phase boundary through heavy ion collision experiments. In the next sub-section, we will show in some detail of the first principle finite temperature Lattice QCD calculations for the QCD thermodynamic, such as the order of the QCD phase transition and the location of the QCD critical point.

1.2.2 QCD Phase Transition : Lattice QCD at Zero Density

To understand the properties of the QGP and the nature of the QCD phase transition, theoretical studies by the first principle calculations of QCD at high temperature and/or density are important. Currently, Lattice QCD calculations represent the only method to do so. Finite temperature Lattice QCD calculations at $\mu_B = 0$ provide an effective tool in understanding the physics of early Universe and of high energy heavy ion collisions, where the baryon chemical po-
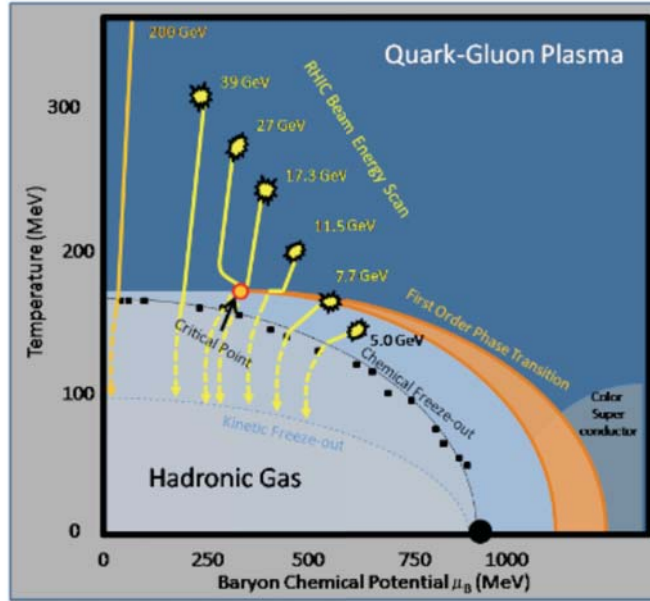
Figure 1.3: A schematic of the phase diagram of nuclear matter. The location
of the CP is placed within the RHIC BES range. Lattice QCD estimates
indicate that the CP falls within the interval $250 < \mu_B < 450$ MeV. The black
closed circles are current heavy-ion experimental calculations of the chemical
freeze-out temperature, T_{ch}, and μ_B based on statistical model fits to the
measured particle ratios. The yellow curves show the estimated trajectories of
the possible collision energies at RHIC. Figure is from [19].

tential μ_B is small (at RHIC top energy, $\mu_B \sim 20$ MeV). In the followings, some

important results of QCD thermodynamics, such as equation of state, nature of

phase transition as well as transition temperature T_c, from the finite temperature

Lattice QCD calculations at $\mu_B = 0$ will be presented.

In Lattice QCD calculations, one has to use several parameters to describe

a thermodynamic system. In addition to the number of lattice points in spacial

N_s and temporal N_τ directions, the quark masses m_q, the coupling $\beta = 6/g^2$

and the chemical potential μ_q have to be also used. Before we perform lattice

calculations, a lattice spacing a should be specified and thus the temperature and

volume of the system are determined by $T = 1/aN_\tau$, $V = (aN_s)^3$, respectively.

After the right action is chosen, there are two important ingredients to bias the

results of Lattice QCD calculations [20], one is the masses of light (m_q) and

strange quarks (m_s) used and the other is the degree of continuum. By using the physical masses and small value of the lattice spacing a, one can reduce the systematic errors of the estimated physical quantities. Such a calculation is quite CPU demanding.
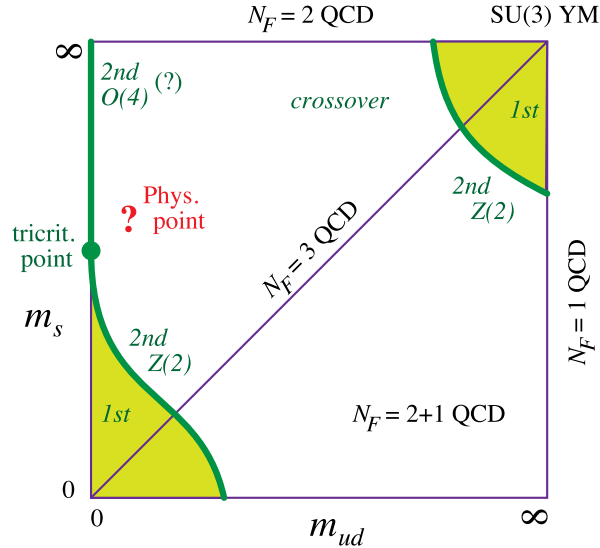
Figure 1.4: The Columbia-plot:the nature of the finite temperature transition in 2+1 flavor QCD at $\mu_B = 0$ as a function of the degenerate u and d quark mass m_{ud} and the s quark mass m_s. The figure is taken from [21].

The standard picture for the QCD phase diagram [21] in the light quark mass (m_{ud}) versus strange quark mass (m_s) plane ($N_f = 2 + 1$ flavor, $\mu_B = 0$) is shown in Fig. 1.4. It demonstrates that the nature of the transitions depends on the quark masses. The phase diagram contains two regions at small and at large quark masses, for which the $T > 0$ QCD transition is of first order. At intermediate values of the quark masses, the "transition" will be actually an analytic crossover. On the boundaries of the first order regions, we expect second order transitions. There is a question mark in the cross-over region, where the physical quark mass point might be located.

The equation of state (EOS) can provide us many important information about the system, such as the degree of freedom. The Wuppertal-Budapest Col-

laboration obtained the results for the EOS with stout quarks at the physical point [22], obtained on $N_\tau = 6 - 10$ lattices. Pressure (P) and energy density (ϵ) as a function of temperature calculated from Lattice QCD at $\mu_B = 0$ is shown in Fig. 1.5. We may find a sharp increase for the pressure and energy density, which indicates the appearance of color degrees of freedom. However, the order of the phase transition depends on the masses of the quarks implemented in the Lattice QCD calculations. The arrows denote the Stefan-Boltzmann limits, where we assume the systems with massless, non-interacting quarks and gluons. The similarity of the three curves in the insert plot of Fig. 1.5 indicates that besides the effect of quark masses, there should be interactions in the newly formed system, which is different from the original weakly interacting QGP scenario.
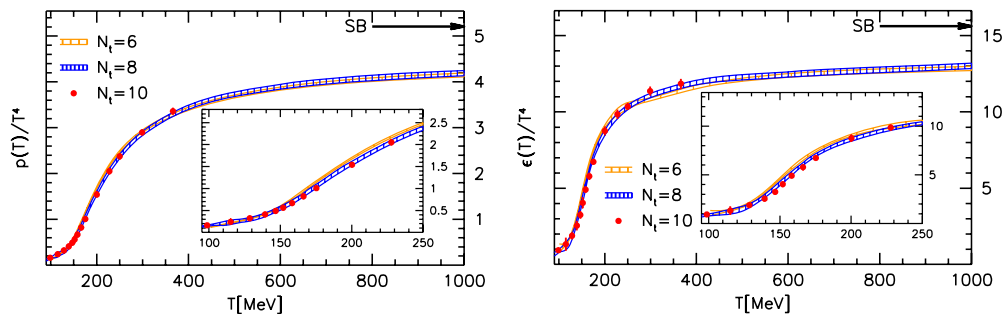
Figure 1.5: EOS in 2+1 flavor QCD with stout quarks at the physical point reported from Wuppertal-Budapest collaboration. The inter plots show the ratio of P/P_{SB} and ϵ/ϵ_{SB}, respectively. The figures are taken from [22].

To determine the nature of the transition one should apply finite size scaling techniques for the chiral susceptibility $\chi = (T/V) \cdot (\partial^2 \log Z / \partial m_{ud}^2)$, which shows a pronounced peak as a function of temperature (the coupling β is related to the temperature). Left panel of Fig 1.6 shows the finite size scaling for a first order phase transition, the pure gauge theory. The peak of analogous Polyakov loop susceptibility for pure gauge theory gets more and more singular as we increase the volume (V), where the width scales with the $1/V$, the height scales with volume (V). A second order transition will show a similar singular behavior with

critical indices. In the middle and right panel of Fig.1.6, the chiral susceptibility peak width and height saturate to a constant value, which is a characteristic properties of analytic transition, the so called cross-over.
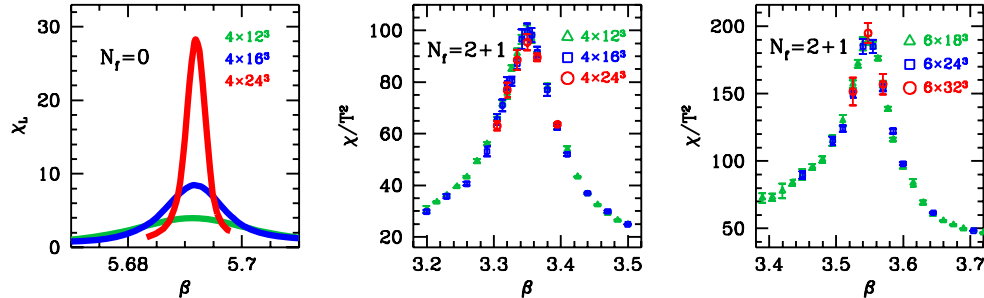
Figure 1.6: The volume dependence of the susceptibility peaks for pure SU(3) gauge theory (Polyakov-loop susceptibility, left panel) and for full QCD (chiral susceptibility on N_τ=4 and 6 lattices, middle and right panels, respectively). The figures are taken from [20].

In quantum chromodynamics, there is a conventional temperature named T_c, which is an intrinsic scale of bulk hadronic matter. It can be defined as the temperature at the peak of a susceptibility, such as Ployakov loop and chiral susceptibility, at $\mu_B = 0$. The value of T_c changes with μ_B. This is similar to saying that the Celsius scale of temperature is defined by the boiling point of water at normal pressure, P, and that the boiling point changes with P. At present, the theoretical estimation of T_c at $\mu_B = 0$ in the market are mainly given by two groups, the "hotQCD" and "Wuppertal-Budapest" group. The detail of the T_c values obtained by the two groups are shown in Tab. 1.1. Both groups give continuum extrapolation results with physical value of pion meson mass (m_π). However, there are still some discrepancies between T_c estimated by the two groups. It motivates us to extract the T_c directly from the experimental measurements in heavy ion collisions.

Table 1.1: Status of transition temperature T_c estimation.

T_c (MeV)	hotQCD	Wuppertal-Budapest
Chiral susceptibility	192 (7)(4) [12]	151 (3)(3) [20, 13]
Polyakov loop susceptibility	192 (7)(4) [12]	175 (2)(4) [20, 13]
s quark number susceptibility	N/A	176 (3)(4) [20, 13]

1.2.3 On the Location of the QCD Critical Point : Lattice QCD at Finite Density

It is a long-standing open question, whether a critical point exists on the QCD phase diagram and how to predict theoretically its location. Since the phase transition at zero μ_B is not a thermodynamic singularity but a rapid cross-over from the region dominated by a gas of hadrons to the one dominated by quark and gluon degrees of freedom [14]. This basic picture has been built up by finite temperature lattice calculations. On the other hand, the transition at $(T = 0, \mu_B > 0)$ region is thought to be first order phase transition. This conclusion is less robust, since the first principle lattice calculations are not controllable in this region due to serious fermion sign problem. But the results from different models indicate that the transition at this region should be first order phase transition. Thus, people argue that there must be a critical point somewhere in the midst of the QCD phase diagram as the end point of the first order line [11].

Recently several methods, such as reweighting method [24], imaginary chemical potential [25] and Taylor expansion method [26], were developed to circumvent the sign problem and thus access the region of finite chemical potentials. Fig. 1.7 shows the quark number susceptibility as a function of temperature calculated from Lattice QCD with hybrid method of Taylor expansion and reweighting. It is peaked around T_c for large μ_q/T, which indicates the existence of the critical point [23].
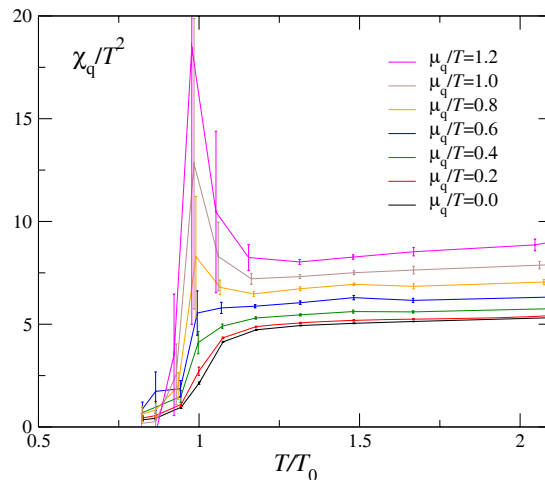
Figure 1.7: Quark number susceptibility as a function of temperature and μ_q/T by a simulation with an improved Wilson quark action. T_0 is T_c at $\mu_q = 0$. The figure is taken from [23].

The locations of QCD critical point predicted from Lattice QCD and QCD based model calculations are summarized in Fig. 1.8. Also, the information about the location of the freeze-out point for given experimental conditions is obtained by the fitting the ratios of the particle yields with thermal model. We may find that the possible locations of the critical point are widely distributed based on theoretical predications, which means large uncertainties in those theory calculations. Hence, we may need input from heavy ion collision experiment, which can provides us an ideal tool to search for the CP.

1.3   Ultra-relativistic Heavy Ion Collisions

QCD predicts that the quarks and gluons are confined in the hadrons in the normal conditions while a new form of matter, the quark-gluon plasma (QGP), dominated by quark and gluo degrees of freedom can be formed by heating and/or compressing normal nuclear matter.

The QGP exist in early Universe, when the universe was only a few tens of microseconds old. On the other hand, a compact star, such as neutron star, is
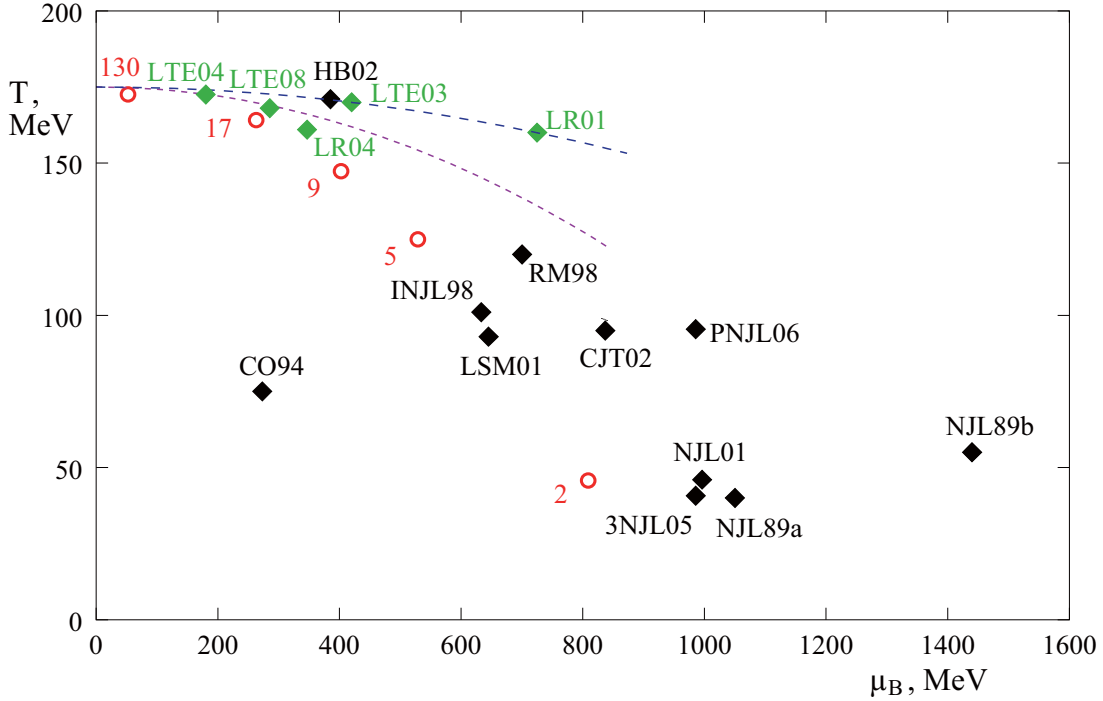
Figure 1.8: Comparison of predictions for the location of the QCD critical point on the phase diagram. Black points are model predictions: NJLa89, NJLb89 – [27], CO94 – [28, 29], INJL98 – [30], RM98 – [31], LSM01, NJL01 – [32], HB02 – [33], CJT02 – [34], 3NJL05 – [35], PNJL06 – [36]. Green points are lattice predictions: LR01, LR04 – [18, 37], LTE03 – [38], LTE04 – [39], LTE08 – [40]. The two dashed lines are parabolas with slopes corresponding to lattice predictions of the slope $dT/d\mu_B^2$ of the transition line at $\mu_B = 0$ [38, 41]. The red circles are locations of the freezeout points for heavy ion collisions at corresponding center of mass energies per nucleon (indicated by labels in GeV). The figure is taken from [11].

much cooler than the QGP, but it is compressed by its own weight to such high densities that it is reasonable to surmise that quark matter also may exist in the core. The experimentally relevant way is to prepare the QGP by "heating", i.e. by depositing energy into the system, out of which QGP then can form. An unique experimental tool to reproduce the similar environment is to collide two heavy ions at very high energy. One expects to create matter under conditions that are sufficient for deconfinement. The heavy ions are accelerated and collided in the relativistic heavy ion colliders, which is designed to search for the new form of QGP matter. By colliding two nuclei at different energies, we can produce hot dense nuclear matter at various temperature (T) and baryon chemical potential (μ_B). Hence, this allow us to access the different regions of the QCD phase diagram in order to search for the QCD critical point and map the first order phase boundary.

Initially in 70's and early 80's some accelerators used by particle physics earlier, such as Bevatron at the Berkeley Lab, were converted to accelerate heavy ions. At the same time the energies of the accelerators used for nuclear research increased, such as in NSCL/MSU and GSI in Darmstadt. By the mid 80's the heavy ions were injected into some of the highest energy proton accelerators also, i.e. Alternating Gradient Synchrotron (AGS) at Brookhaven National Laboratory (BNL) and the Super Proton Synchrotron (SPS) at the European Center for Nuclear Research (CERN). By the early 90's the injection of the heavy ions is studied already at the planning phase of new accelerators, like Relativistic Heavy Ion Collider (RHIC) at BNL and Large Hadron Collider (LHC) at CERN. Up to date, RHIC has successfully performed Au+Au and Cu+Cu collisions at $\sqrt{s_{\mathrm{NN}}}$ = 200 GeV, which is the designed top energy for heavy ion collisions. In 2010, Pb+Pb head on collisions at $\sqrt{s_{\mathrm{NN}}}$ = 2.76 TeV were also successfully performed at the LHC at CERN.

Fig. 1.9 shows a cartoon of a relativistic heavy ion collision. Because of the
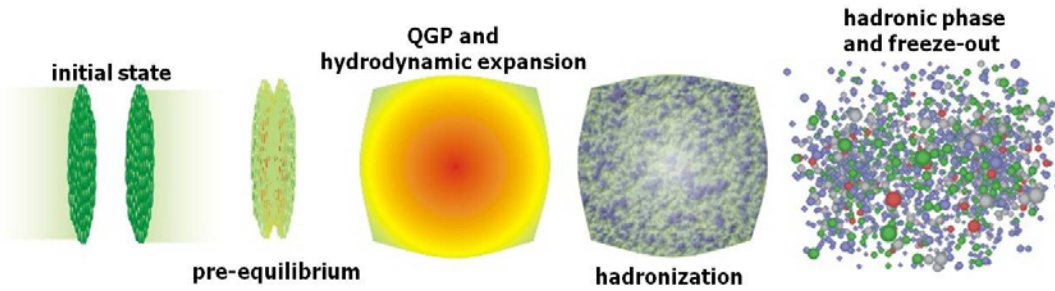
Figure 1.9: Cartoon of a relativistic heavy-ion collision. Left to right: the two nuclei approach, collide, form a QGP, then the QGP expands and hadronization, finally hadrons rescattering and freeze out.

Lorentz contraction effect in the moving direction, two nuclei can be seen as two thin disks approaching each other at high speed. The energy density estimated with Bjorken approximation [42] for Au+Au central collision at RHIC top energy (~ 5 GeV/fm^3) is much higher than the energy density needed for the formation of QGP from the Lattice QCD calculation (~ 1 GeV/fm^3). The physics processes at the initial stage (~ 1 fm/c) are dominated by hard scatterings, such as quark pair production, jet production and fragmentation. During the initial stage of the collisions, heavy ions deposit their energy into the collision region and hadrons "melt" into quarks and gluons to form QGP. The subsequent processes are the expansion and hadronization of QGP, when the fireball cools down and partons are hadronized into hadrons ($1 \sim 10$ fm/c). Then, the system reaches a stage called chemical freeze-out, where the abundance of the hadrons are fixed and the inelastic interaction between hadrons cease. Finally, the system is dilute enough and comes to the kinetic freeze-out as an end, when the hadrons cease their elastic interactions ($10 \sim 15$ fm/c).

Plenty of exciting physics results reveal that the matter created at RHIC top energy is quite different from what we observed before and it can not be described by hadronic degrees of freedom. Those measurements provide strong hints that the strongly interacting QGP has been formed in the at top energy

Au+Au collisions at RHIC. Some selected key measurements from RHIC will be discussed in the following sections.

1.3.1 Particle Production and Hadron p_T Spectra

A hot and dense medium is believed to be created in heavy ion collisions. Thus, it is of particular relevace to check whether the produced medium in its early stage passed through the QGP phase. In the bulk sector, hadron multiplicity and correlations are expected to provide information on the nature, composition, and size of the medium [43]. By fitting the experimental particle multiplicities with a thermal model, we can extract thermal parameters, temperature (T_{ch}) and baryon chemical potential (μ_B) of the hot dense medium at chemical freeze-out of heavy ion collision, when the inelastic collision cease. This allows us to quantify from the experimental side the features of the phase diagram of hadronic matter and establish the "line of chemical freeze-out" described by an universal condition for chemical freeze-out [43].

A compilation of measurement of yields at mid-rapidity for various hadron species is shown in left panel of Fig. 1.10 for central Au+Au or Pb+Pb collisions. The contributions from feeding due to weak decays has been removed as shown in right panels of Fig. 1.10. The main properties concerning the chemical composition of the medium at mid-rapidity can derived from the yields shown in the Fig. 1.10 without any model.

Fig.1.11 shows the thermal model fits for the low p_T integrated particle yields ratios of Au+Au central collisions at $\sqrt{s_{\mathrm{NN}}} = 200$ GeV measured by STAR experiment. The corresponding fitted thermal parameters at chemical freeze-out are $T_{ch} = 163 \pm 4$ MeV, $\mu_B = 24 \pm 4$ MeV, $\gamma_s = 0.99 \pm 0.07$ (Non-equilibrium parameter). It can be found that the quality of the fits is very good for most of the hadrons except some short-lived resonances, such as Λ^* and K^*. This may be
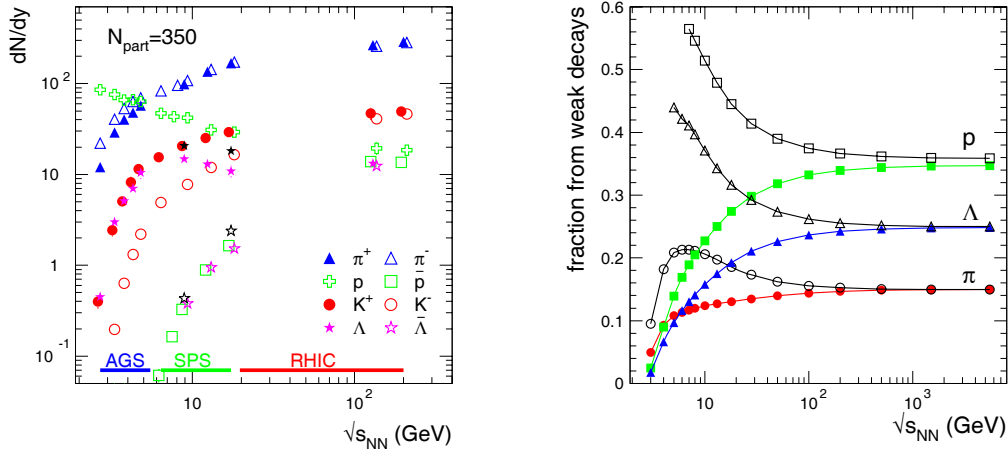
Figure 1.10: Left Panel: The energy dependence of experimental hadron yields at mid-rapidity for various species produced in central heavy ion collisions.
Right Panel: The energy dependence of fraction of total hadron yields originating from weak decays. The full symbols are for particles (π^+, p, Λ), the open ones for antiparticles $(\pi^-, \bar{p}, \bar{\Lambda})$. The figures are taken from [44].

due to the hadronic re-scattering after chemical freeze-out. The variation of γ_s from 0.75 to 1 (peripheral to central) shown in the inset plot of Fig.1.11 indicates the saturation of the strange sector has been achieved for the first time at RHIC.

In the left panel of Fig. 1.12, we show the energy dependence of T_{ch} and μ_B extracted from the thermal fits of the experimental data from AGS, SPS and RHIC. The solid lines shown in the figures are the parametrization for the results obtained by fitting mid-rapidity data with expressions:

$$T_{ch}[\text{GeV}] = T_{lim}\left(1 - \frac{1}{0.7 + (\exp(\sqrt{s_{NN}}(\text{GeV})) - 2.9)/1.5}\right) \quad (1.4)$$

$$\mu_B[\text{GeV}] = \frac{a}{1 + b\sqrt{s_{NN}}(\text{GeV})}, \quad (1.5)$$

, where the parameters $a = 1.303\pm0.120$ GeV, $b = 0.286\pm0.049$ GeV^{-1} and $T_{lim} = 0.161\pm0.004$ GeV. The right panel of Fig. 1.12 shows the phase diagram of QCD matter embedding with T_{ch} and μ_B value extracted from thermal fits of the
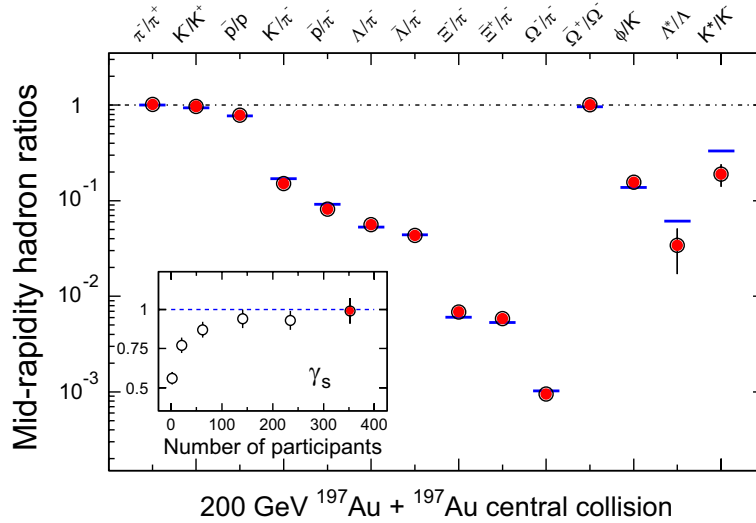
Figure 1.11: Ratios of p_T-integrated mid-rapidity yields for different hadron species measured in STAR for central Au+Au collisions at $\sqrt{s_{\mathrm{NN}}} = 200$ GeV. The horizontal bars represent thermal model fits to the measured yield ratios for stable and long-lived hadrons. The variation of γ_s with centrality is shown in the inset, including the value (leftmost point) from fits to yield ratios measured by STAR for 200 GeV p+p collisions. The figure is taken from [45].

AGS, SPS and RHIC data [44]. It is important to notice that the chemical freeze-out points below $\mu_B < 400$ coincides well with the phase boundary obtained from 2+1 flavor lattice QCD calculations.

The transverse momentum spectra of various hadron species can provide information about the bulk properties of the medium, such as radial flow and temperature, at kinetic freeze-out, where the elastic collision between particles cease. Since people realized that the Blast Wave (BW) model has some limitations in describing the hadron p_T spectra, due to strong assumptions of local equilibrium and arbitrary fit range in p_T the non-extensive Tsallis statistics was introduced to understand the particle production in heavy ion collisions [46, 47]. Then, the Tsallis distribution is embedded in the BW model instead of Boltzmann distribution for source of particle emission, describing hydrodynamic expansion in heavy ion collisions, which is so called Tsallis Blast Wave (TBW) model. In the
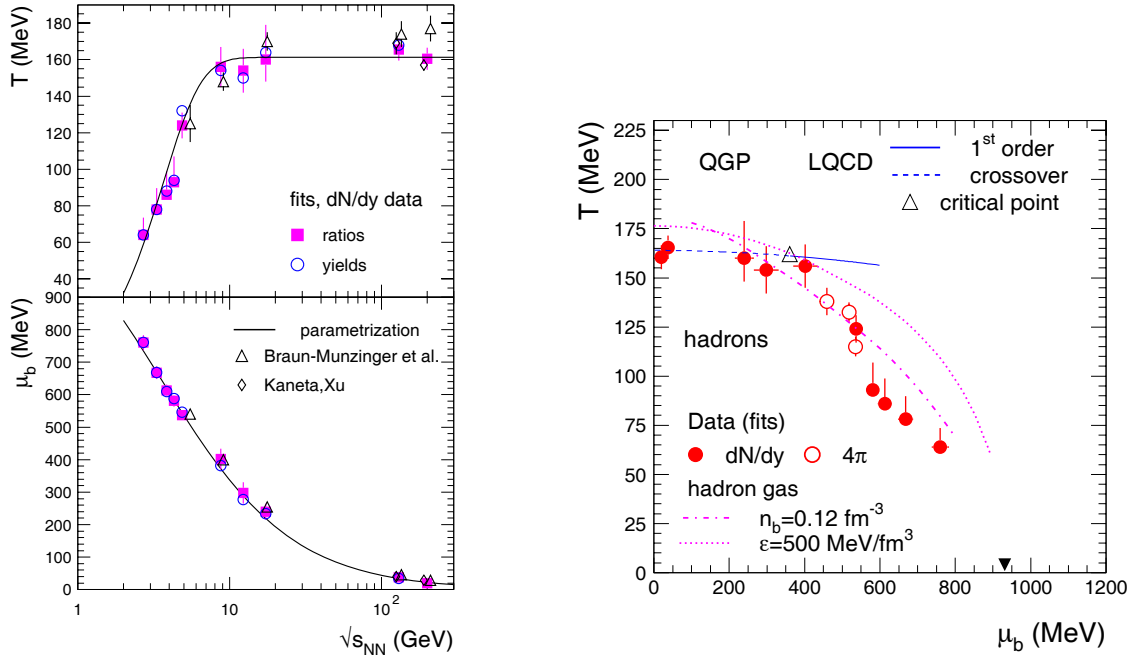
Figure 1.12: Left Panel: The energy dependence of temperature and baryon chemical potential. Right Panel: The experimental values for the chemical freeze-out are shown together with results of lattice QCD calculations. The predicated critical point is marked by open triangle. The freeze-out curve for hadron resonance gas at constant energy density ($\epsilon = 500$ MeV/fm^3) and constant total baryon density ($n_b = 0.12$ fm^{-3}) are also included. The full triangle is the ground state of nuclear matter. The figures are taken from [44].

TBW model, there are three common parameters for all particles: temperature T, non-equilibrium parameter q and average flow velocity β. The Tsallis distribution behaves as a power law function at high p_T, an exponential distribution at low p_T and Boltzmann distribution when $q \rightarrow 1$.

Fig. 1.13 shows the identified spectra measured by STAR and PHENIX collaborations and their associated TBW results from the fit. It is found that the strange hadrons approach equilibrium quickly from peripheral to central Au+Au collisions and they tend to decouple earlier from the system than the light hadrons but with the same final radial flow. The kinetic freeze-out temperature of strange hadrons is also found to be similar to the chemical freeze-out temperature
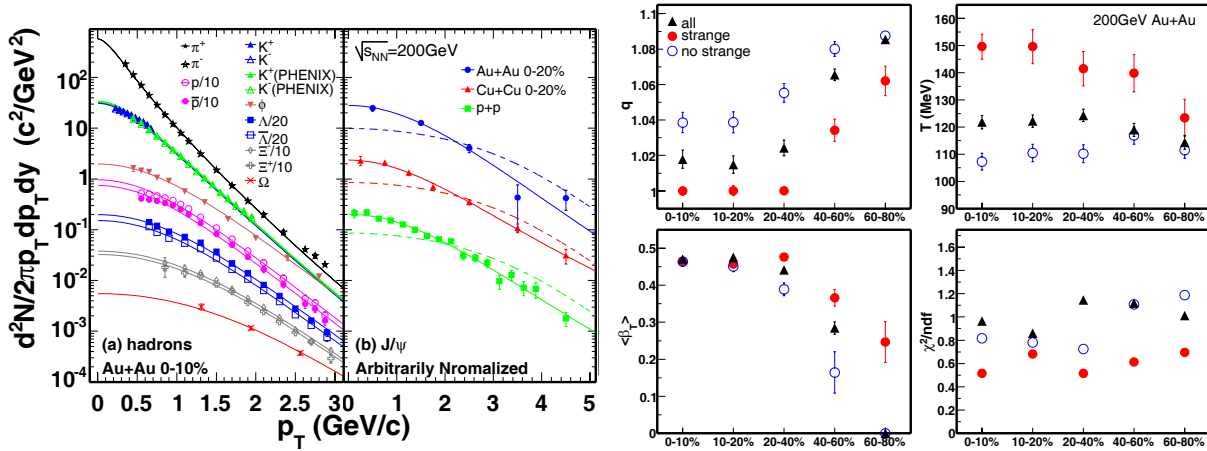
Figure 1.13: Left Side : Identified particle spectra from Au+Au collisions at $\sqrt{s_{NN}}$=200 GeV. The left panel: spectra of light hadrons and strange hadrons. The solid curves are results from TBW fit. the right panel: J/ψ spectrum, the dashed line is the TBW prediction using parameters from the fit to other hadrons, and the solid curve is a TBW fit to J/ψ alone. Right Side : q, T, β and χ^2/nDoF as a function of centrality for different groups of hadrons from the TBW model fit to spectra in Au+Au collisions at $\sqrt{s_{NN}}$=200 GeV. The figures are taken from [47].

extracted from the thermal model fit of particle yield ratios. These results provide an alternative picture of freeze-out: a thermalized system is produced in the partonic phase; the hadronic scattering at later stage is not enough to maintain the system in equilibrium and does not increase the radial flow of the copiously produced light hadrons [47].

We may find that the relative particle production rates, transverse momentum spectra of identified hadrons and their radial flow are all consistent with the formation of thermalized partonic matter. Its subsequent hadronization during the phase transition should in general drive hadronic constituents towards equilibrium and the pressure gradient pushes the bulk hadrons with a collective radial velocity field. The high degree of equilibrium of hadron multiplicities and collective radial flow gained by hadrons could be related to the strongly interacting QGP phase at early stage of heavy ion collisions.

1.3.2 Elliptic Flow

In non-central heavy ion collisions, the initial spatial anisotropy and the frequent interaction between constituents of the system will build up an azimuthal anisotropy pressure gradient. Consequently, the spatial anisotropy will be transferred into azimuthal anisotropy in the momentum space driven by the pressure gradient. To characterize the azimuthal anisotropy in momentum space, the momentum spectra of particles is expanded as a Fourier series in terms of azimuthal angle (ϕ) as:

$$E\frac{d^3N}{dp^3} = \frac{d^2N}{2\pi p_T dp_T dy}(1 + \sum_{n=1}^{\infty} 2v_n cos[n(\phi - \Psi_{rp})]) \tag{1.6}$$

$$v_n = \langle cos[n(\phi - \Psi_{rp})]\rangle \tag{1.7}$$

, where Ψ_{rp} denotes the direction of the reaction plane defined by the beam direction and the impact parameter. The Fourier expansion coefficient v_n stands for the nth harmonic of the event azimuthal anisotropy [48]. The v_1 and v_2 are so called directed and elliptic flow, respectively. The elliptic flow is of particular interest as it is considered to be quite sensitive to the early stage of collisions due to the self-quenching effect [49]. Thus, the elliptic flow provides us an experimental tool for probing the properties of the hot dense matter created at early stage, such as equation of state (EoS), degree of freedom and degree of thermalization. To check whether the deconfinement, thermalized and strongly interacting partonic matter has been formed in the early stage of the collisions, the elliptic flow calculated from ideal hydrodynamics have been applied to compare with the experimental data [50].

In left panel of Fig. 1.14, the elliptic flow (v_2) of charged pions, charged and neutral kaons, protons and lambdas and their anti-particles for Au+Au minimum-bias collisions at $\sqrt{s_{NN}} = 200$ GeV show almost linear increase with transverse momentum in the low-p_T region up to $p_T \approx 1.5$ GeV/c [50]. A clear
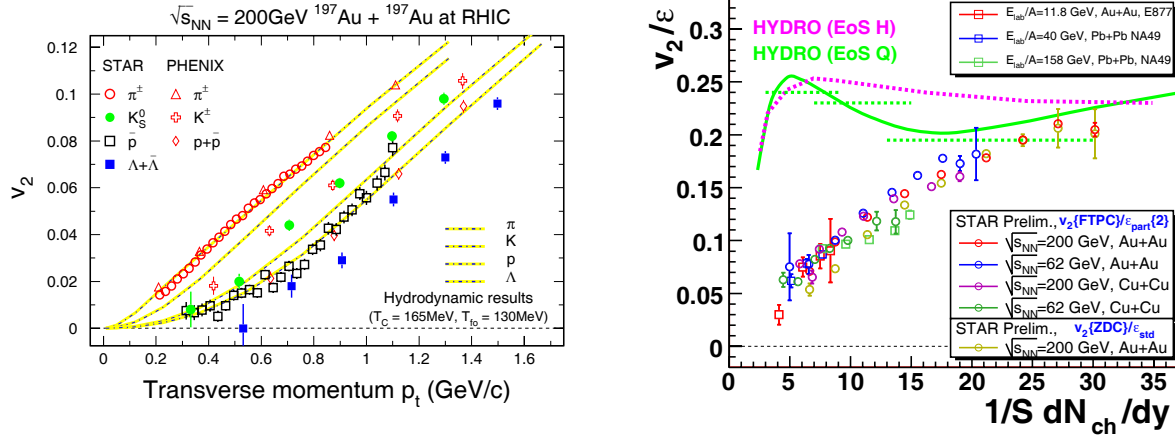
Figure 1.14: Left Panel : Elliptic flow v_2 for different particle species measured by STAR and PHENIX compared to hydrodynamic model predictions. The data indicates the expected mass ordering in this low p_T region. Right Panel : Compilation of v_2/ϵ for charged hadrons as a function of particle density at mid-rapidity. Green dashed lines represent ideal hydrodynamic limit for AGS, SPS and RHIC collisions energies. The figures are taken from [50, 51].

mass ordering effect is also visible: particles with a higher mass show a smaller v_2 at a given p_T than particles with lower mass and this can be described by hydrodynamical model successfully, which describes these observations in this p_T-region to a level of $20 - 30\,\%$, attributing the mass ordering to an underlying common transverse velocity field. The hydrodynamics, in which thermalization is assumed and mean free path is much smaller than the system size, predict the values of v_2 is only proportional with initial state spatial anisotropy (ϵ), namely $v_2/\epsilon = const$. In the right panel of Fig. 1.14, we show the elliptic flow (v_2) scaled by eccentricity ϵ as a function of transverse charged particle density at mid-rapidity for various colliding systems [51]. The values of v_2/ϵ have shown a linear dependence on the transverse particle density at low energy and are close to the values predicted by ideal hydrodynamics at RHIC top energy. This may indicate that the thermalization might be already built-up in the early stage of the most central Au+Au collisions for first time at the RHIC top energy.
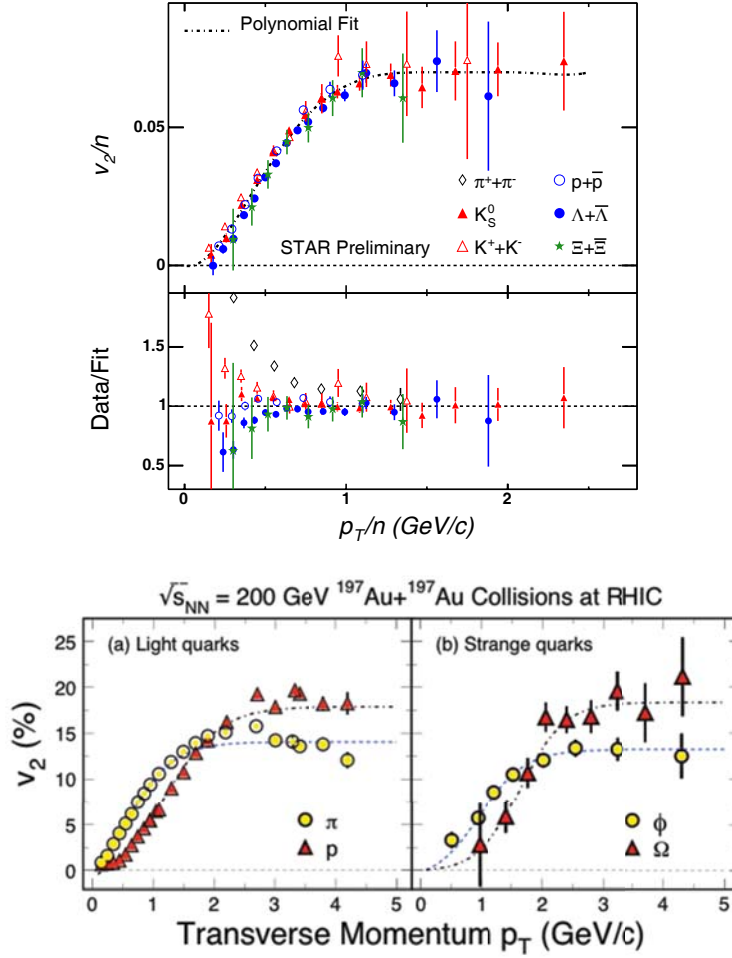
Figure 1.15: Upper panel: Test of number of quarks (NQ) scaling of identified hadron v_2 in Au+Au minimum-bias collisions at $\sqrt{s_{\rm NN}} = 200$ GeV(The lower plot shows the ratio of the data to the dashed-dotted fit to the data in the upper plot.) Lower panel: v_2 as a function of p_T for π, p (left) and ϕ, Ω (right). Lines represent NQ-inspired fit. The figures are taken from [50, 52].

Another necessary condition for formation of QGP is the deconfinement of the quarks from hadrons. The upper panel of Fig. 1.15 shows the v_2 for different particle species scaled according to the number of quarks (NQ) of the hadrons as a function of NQ scaled p_T. It can be observed that mesons and baryons fall onto one universal curve when $p_T/NQ > 0.6$ GeV/c [50]. This may imply that the final hadrons at intermediate p_T range are formed by coalescence of constitute quarks when the partonic phase hadronizes. This provides the evidence of deconefinement at the early stage of the collisions at RHIC. In the lower panel of Fig. 1.15, the comparable v_2 of multi-strange hadrons (ϕ and Ω) to light hadrons (π and p) is directly pointing to the creation of strongly interacting partonic matter (partonic collectivity) at the early stage of the collisions, due to the early decoupling from the system and less suffering from the hadronic scattering for the multi-strange hadrons [52].

Finally, several evidences from elliptic flow (v_2) measurements have been found to support the idea that the deconfinement, thermalized, strongly interacting partonic matter (QGP) has been formed in the central Au+Au collisions at RHIC top energy.

1.3.3 Jet Quenching

In heavy ion collisions, high p_T ($p_T >\sim 5$ GeV/c) particles are believed to be generated through fragmentation of energetic partons (jets) produced by the initial QCD hard-scattering processes [53]. Those energetic partons will loss energy when traveling through the hot dense medium by collisional energy loss and medium-induced gluon radiations. Hence, the final state particles fragmented from the jets can be used as an ideal probe for the hot dense medium created in the early stage of the heavy ion collisions by studying jet-medium interactions.

Experimentally, the nuclear modification factor, the difference between the

spectrum in A+B collisions with respect to a p+p collision reference, is widely used to describe or demonstrate the jet-quenching phenomena. It is defined as:

$$R_{AB}(p_T) = \frac{d^2 N_{AB}/dp_T dy}{T_{AB} d^2 \sigma_{pp}/dp_T dy} \tag{1.8}$$

, where $T_{AB} = \langle N_{bin} \rangle / \sigma_{pp}^{inel}$ is the nucleus overlap function, calculated from a Glauber model [54]. N_{bin} denotes the number of binary collisions in a nucleus-nucleus collision. The experimental results shown in left panel of Fig. 1.16 demonstrate that there is a strong suppression relative to the binary scaling expectation at high p_T in the central Au+Au collisions $-$ jet quenching [55]. While this suppression is not seen in d+Au collisions which imply that the suppression in central Au+Au is due to the final state interactions rather than initial state effect and thus hot dense matter must be created in central Au+Au collisions at top energy of RHIC. This means the energetic partons loss their energy by interacting with the hot dense medium and then the production of the high p_T particles will be suppressed.
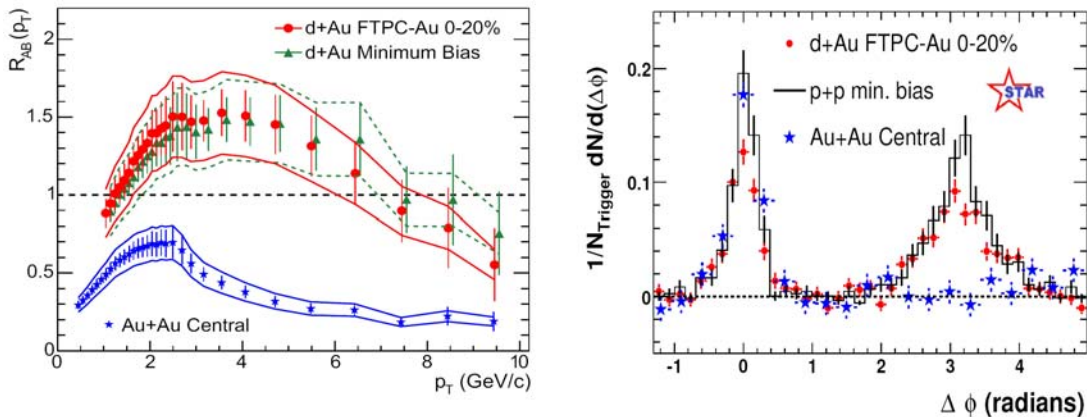
Figure 1.16:   Left: $R_{AB}(p_T)$ as a function of transverse momentum in d+Au and Au+Au 200 GeV collisions at RHIC. Right: Two particle azimuthal distributions in p+p, d+Au central and Au+Au central collisions at $\sqrt{s_{NN}} = 200$ GeV The figures are taken from [55].

The jet-quenching phenomena has also been illustrated by a dihadron azimuthal angle correlation study. The right panel of Fig. 1.16 shows the associ-

ated hadrons ($p_T^{associate} > 2$ GeV/c) azimuthal distribution relative to a triggered hadron ($p_T^{trigger} > 4$ GeV/c). The enhanced near side correlation $\Delta\phi \sim 0$, which means the pair is from a single jet, is observed in p+p, d+Au and Au+Au collisions. The pair from the back-to-back jet correlation at $\Delta\phi \sim \pi$ only appears in p+p and d+Au while it almost completely disappears in central Au+Au collisions.

1.3.4   Motivation of the Study

Our main purpose of performing higher moments analysis in heavy ion collision experiment is to probe the bulk properties, such as the phase boundary, QCD critical point [56] and thermalization, of the hot dense nuclear matter in the nature. It opens a completely new domain and effective way for probing the bulk properties of hot dense nuclear matter and test the QCD theory at non-perturbative region. It also can be used to constrain some QCD fundamental parameters, such as the scale for the QCD phase diagram (the transiton temperature T_c at $\mu_B = 0$), by comparing the experimental data with the first principle Lattice QCD calculations.

Recently, it was found that the higher order fluctuation observables-higher moments (Variance (σ^2), Skewness (S), Kurtosis (κ)) of conserved quantities, such as net-baryon, net-charge, and net-strangeness, distributions can be directly connected to the corresponding thermodynamic susceptibilities in Lattice QCD [57] and Hadron Resonance Gas (HRG) model [58], for *e.g.* the third order susceptibility of baryon number ($\chi_B^{(3)}$) is related to the third moment ($< (\delta N_B)^3 >$) of baryon number distributions[1] as $\chi_B^{(3)} = < (\delta N_B)^3 >/VT^3$; V, T are volume and temperature of system respectively. As the volume of the system is hard to determine, the susceptibility ratio, such as $\chi_B^{(4)}/\chi_B^{(2)}$ and

---

[1]see detail in chapter III.

$\chi_B^{(3)}/\chi_B^{(2)}$, are used to compare with the experimental data as $\kappa\sigma^2 = \chi_B^{(4)}/\chi_B^{(2)}$ and $S\sigma = \chi_B^{(3)}/\chi_B^{(2)}$. Theoretical calculations demonstrate that the experimental measurable net-proton (proton number minus anti-proton number) number fluctuations can effectively reflect the fluctuations of the net-baryon and net-charge number [59]. Thus, it is of great interest to measure the higher moments of event-by-event net-proton multiplicity distributions in the heavy ion collision experiment. It allows us to probe the bulk properties of the hot dense nuclear matter and test the QCD theory at non-perturbative domain, which is rarely tested by experiments.

Current results from heavy ion collision at RHIC top energy suggest that a new form of matter, the strongly interacting quark-gluon plasma (sQGP) has been formed [45]. Finite temperature Lattice QCD calculations predict that the transition from hadronic phase to the QGP phase at high temperature and small μ_B region is a smooth cross-over. While at large μ_B region, we meet notorious fermion sign problem in the aspect of the first principle Lattice QCD calculation. Although many fantastic techniques, such as re-weighting [24], image baryon chemical potential [25] and Taylor expansion [26], have been developed to overcome the problems and make the Lattice QCD calculable at finite μ_B region, the location of QCD critical point and even its existence is not confirmed yet.

Due to the finite size, rapid expansion and critical slowing down effects *etc.*, the effective correlation length in the heavy ion collision near the QCD critical point is a small value about $2 \sim 3fm$ [60]. The event-by-event observables are believed to be sensitive to the correlations and fluctuations. Model calculations demonstrate that higher moments of net-proton distributions are proportional to the higher power of the correlation length [61, 62], such as third order cumulant $< (\delta N)^3 > \sim \xi^{4.5}$ and fourth order cumulant $< (\delta N)^4 > - 3 < (\delta N)^2 >^2 \sim \xi^7$), where $\delta N = N - M$, N is the particle multiplicity in one event and M is the averaged particle multiplicity of the event sample. It motivates us to search for

the QCD critical point with the higher moments of the net-proton distributions, experimentally, as a direct application of the higher moments observable. The characteristic signatures for the appearance of QCD critical point are the non-monotonic dependence of the observations on the colliding energy ($\sqrt{s_{\mathrm{NN}}}$). When approaching the QCD critical point, the moment products $\kappa\sigma^2$ and $S\sigma$ of net-proton distributions will show large deviation from its Poisson statistical value. The skewness is expected to change its sign when system evolution trajectory in the phase diagram cross phase boundary [27].

Several experimental programs have planed to perform heavy ion collisions experiments to locate the QCD critical point, such as RHIC at BNL, SPS/LHC at CERN and FAIR at GSI. In year 2010 (Run 10), RHIC has started Beam Energy Scan (BES) program [19] to tune the center of mass energy from $\sqrt{s_{\mathrm{NN}}} = 39$ GeV down to $\sqrt{s_{\mathrm{NN}}} = 7.7$ GeV with the corresponding μ_B coverage $112 < \mu_B < 410$ MeV. The data for Au+Au collisions at three low energies 7.7, 11.5 and 39 GeV have been taken during year 2010 (Run 10) and another energy point $\sqrt{s_{\mathrm{NN}}}$ = 19.6 GeV is being taken in this year 2011 (Run 11). With large uniform acceptance STAR detector and sensitive observables [56], it provides us good opportunities to search for the QCD critical point at RHIC. We also expect that the phenomena, such as number of quark scaling of v_2, jet-quenching and possible local parity violation, which has already been established for QGP signature at RHIC top energy, will be turned off at those lower BES energy, if our current understanding of RHIC physics and these signatures are correct. This will also provide us the information about the first order phase boundary.

CHAPTER 2

Experimental Setup

2.1 The RHIC Accelerator

The Relativistic Heavy Ion Collider (RHIC) located at Brookhaven National Laboratory (BNL) on Long Island is a high luminosity heavy ion and the only spin polarized proton collider in the world [63, 64]. By accelerating and colliding heavy ion and polarized proton, physicists can study the primordial form of extremely high energy density and high temperature matter created in the first microseconds of the early universe after the Big Bang and also the spin structure of the proton, respectively. The top center-of-mass collision energy for heavy ion beams is 200 GeV per nucleon pair and that for proton pairs is 500 GeV. The average store luminosity for gold-on-gold 200 GeV collision achieved in year 2010 (Run 10) is $20 \times 10^{26} cm^{-2} s^{-1}$, which is an order of magnitude higher than the original design goals for average luminosity. For polarized p+p collision, Run 9 (in year 2009) achieved center-of-mass energy of 500 GeV and the corresponding average store luminosity is $55 \times 10^{30} cm^{-2} s^{-1}$.

The idea to build RHIC dates back to 1983, when it was conceived as part of the long-range plan for nuclear science. The total line-term budget for the RHIC project was 616.66 million US. dollars. The construction project began in 1991 and the collider as well as a complementary set of four detectors, BRAHMS, PHENIX, PHOBOS, and STAR, were completed during 1999 [63]. RHIC is an intersecting storage ring particle accelerator. Its double storage rings ("Yellow"

Figure 2.1: Schematic of the RHIC complex. Relativistic heavy ions collide at six intersection points along the RHIC ring of 3,814 m long.

and "Blue") are hexagonally shaped and 3,834 m long in circumference, with curved edges in which stored particles are deflected and focused by 1,740 superconducting niobium-titanium magnets. Fig. 2.1 shows the schematic of RHIC complex. The six interaction points are at the middle of the six relatively straight sections, where the two rings cross, allowing the particles to collide and four of the interaction points are equipped with detectors. Two large experiments, STAR and PHENIX, are located at 6 and 8 o'clock while the other two relative small experiment PHOBOS and BRAHMS are located at 10 and 1 o'clock, respectively.

Fig. 2.2 shows the RHIC acceleration scenario for Au beam. Three accelerators in the injector chain will boost the energy of ions, and strip electrons from the atoms. The first acceleration stage for ions is in the Tandem Van de Graaff accelerator, while for protons, the 200 MeV linear accelerator (Linac) is used. As an example, gold nuclei leaving the Tandem Van de Graaff have an energy of about 1 MeV per nucleon and have an electric charge Q = +31 (31 of 79 electrons
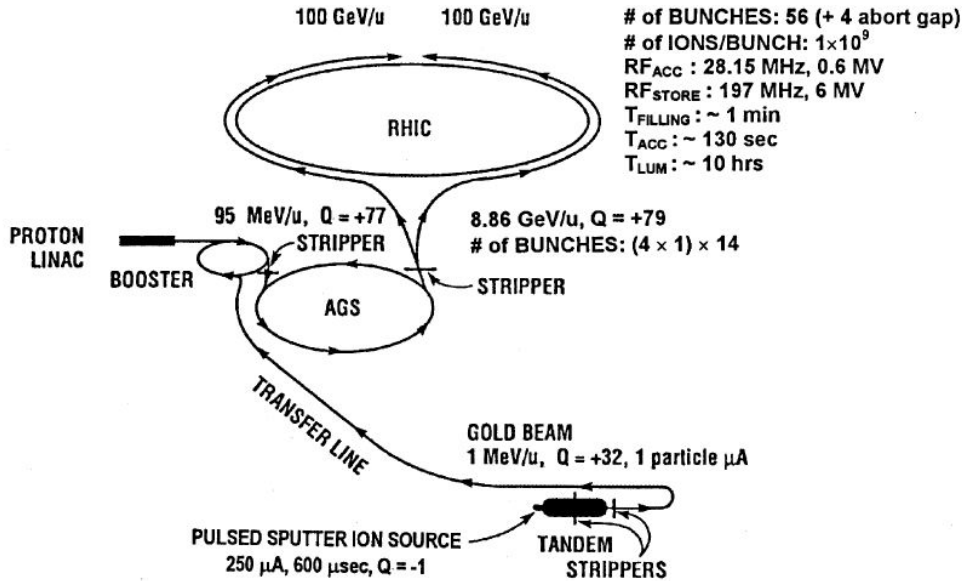
Figure 2.2: RHIC acceleration scenario for Au beam. The figure is taken from [64]

stripped from the gold atom). The particles are then accelerated by the Booster Synchrotron to 95 MeV per nucleon, which injects the projectile now with Q = +77 into the Alternating Gradient Synchrotron (AGS), before they finally reach 8.86 GeV per nucleon and are injected in a Q = +79 state (no electrons left) into the RHIC storage ring over the AGS-to-RHIC Transfer Line (ATR) [64].

Since the pilot run in 1999 and through to 2010, RHIC has had 4 operating periods (Runs) with Au+Au collisions, in the years of 2000, 2001, 2004 and 2007. The Au+Au runs alternated with a d+Au run in 2003, a Cu+Cu run in 2005, and another d+Au run in 2007/08. We have also ran polarized p+p collisions for every year except 2007 and 2010. In year 2010 (Run 10), the RHIC ran Au+Au collisions at $\sqrt{s_{\mathrm{NN}}}$ = 62.4, 39, 11.5 and 7.7 GeV after an 11 weeks 200 GeV physics run. Run 10 was a very successful run during which the RHIC were operating far below the design energy for Au+Au collision and an order of magnitude beyond the original design goals for average luminosity.

2.2   The STAR Experiment

2.2.1   Overview

The Solenoidal Tracker [65] at RHIC (STAR) located at 6 o'clock of RHIC accelerator is one of the two large detector systems constructed at the RHIC at BNL. The massive STAR detecotor weigh over 1200 tons and is as big as a building. It has an large uniform acceptance with full azimuthal angle and large polar angle coverage around mid-rapidity. The layout of the STAR detector is shown in Fig. 2.3.
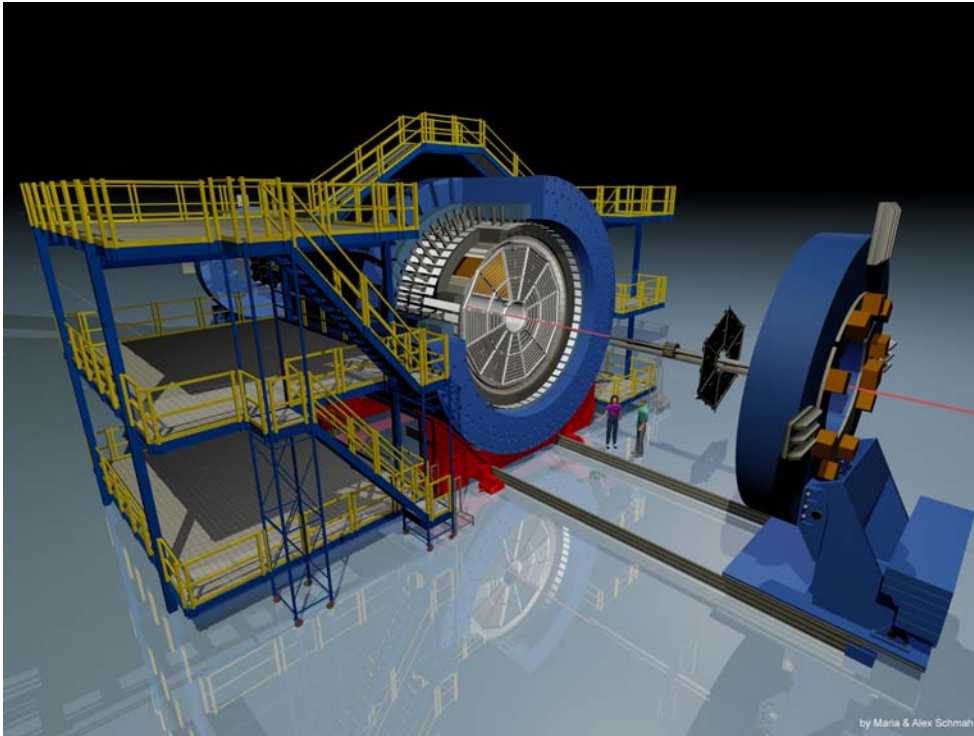
Figure 2.3: First 3D picture of the STAR detector. The figure is taken from [66].

The main goals of the STAR experiment is to study the formation and characteristics of the quark-gluon plasma (QGP), a state of matter believed to exist at sufficiently high energy densities, and explore the phase structure of QCD phase

diagram. The STAR experiment measures many observables simultaneously to study the signature of a possible QGP phase transition and to obtain a fundamental understanding of the microscopic structure of these hadronic interactions at high energy densities. In order to accomplish this, STAR was designed primarily for measurements of hadron production over a large solid angle, featuring detector systems for high precision tracking, momentum analysis, and particle identification at the center of mass (c.m.) rapidity. With large uniform acceptance, the STAR detector is also very suitable for the event-by-event fluctuation and correlation measurements.
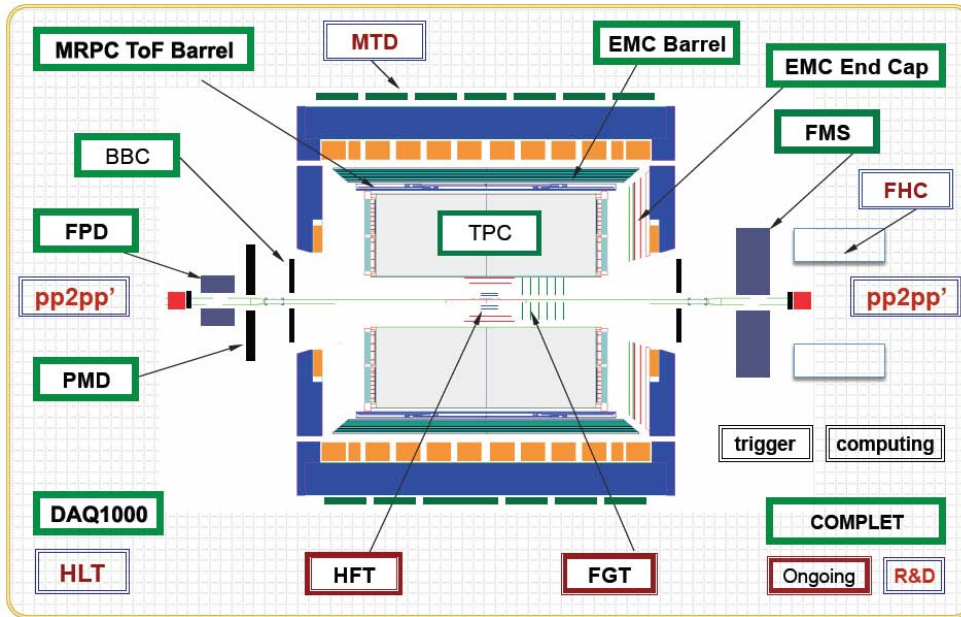
Figure 2.4: Cutaway side view of the STAR detector in year 2008 run and future upgrades.

Fig. 2.4 shows the cutaway view of the STAR detector. STAR consists of several sub-detectors and the main tracking device, the Time Projection Champer (TPC) is located in a homogenous solenoidal magnet. The STAR magnet is cylindrical in design with a length of 6.85 m and has inner and outer diameters of 5.27 m and 7.32 m, respectively. It generates a field along the length of the

cylinder having a maximum of $|Bz| = 0.5$ T. It allows the tracking detectors to measure the helical trajectory of charged particles to get their momenta. To date, the STAR magnet has been run in full field, reversed full field and half filed configurations.

The STAR tracking detectors are used to reconstruct the trajectories of particles in the STAR experiment. The "heart" of the STAR, main tracker, TPC has the pseudo-rapidity $|\eta| < 1.8$ and full azimuth (2π) coverage. The detail of the TPC detector will be discussed in the next sub-section. There are also inner detectors Silicon Vertex Tracker (SVT) and Silicon Strip Detector (SSD) close to the beam pipe, which provides additional high precision space points on tracking so that they can improve the position resolution and allows us to reconstruct the secondary vertex of weak decay particles. But, unfortunately, the SVT and SSD detector were taken out since in the year 2008 (Run 8) because of producing significant unexpect photonic background to the electron related analysis by their material budget. In the forward rapidity region, two Forward radial-drift TPC (FTPC) installed in the east and west of STAR covering $2.8 < |\eta| < 3.8$ and full azimuth angle [65], are used to track particles in the forward and backward rapidity. To measure displaced vertex of hadronic decay channel for the heavy flavor hadron (mainly D and B meson) more preciously, a less material silicon detector the so called Heavy Flavor Tracker [67, 68] (HFT), which consists of two layers of pixels with radius 1.5 and 5 from the beam axis, has been proposed to build in center of the STAR. With HFT, we can improve the signal to background ratio for charmed hadron (D_0, D^*, B, Λ_c) measurement significantly and it allows us to address the long-lived issue of thermalization by measuring the charmed hadron flow. To get better point resolution, the SSD will be placed between HFT and TPC to fill the gap. To improve the precision of the tracking at the forward region, a Forward GEM Tracker (FGT) based on triple GEM technology is proposed and in preparation [69].

The STAR trigger sub-system can be treated as the "brain" of the STAR experiment. It is a 10 MHz pipelined system which is based on input from fast detectors to control the event selection for the much slower tracking detectors. Three fast trigger detectors are Zero Degree Calorimeter (ZDC), Central Trigger Barrel (CTB) and Beam-Beam Counter (BBC). Two ZDCs, centered at 0° and with polar angle coverage < 2.5 mrad, are placed on each side and about 18 m away from the center of STAR. Hadronic calorimeter ZDC is put beyond the dipole magnet to detect the outgoing neutral particles (mostly neutron) after the charged particles bent by magnet. The CTB is installed surrounding the outer cylinder of the TPC, and was used to trigger the flux of charged-particles in the mid-rapidity region. It has been replaced by barrel Time of Flight detector (TOF) (will be discussed in the following sub-section). The BBC subsystem consists of a hexagonal scintillator array structure placed at 3.5 m away from the TPC center and covers $3.3 < |\eta| < 5$. It is the main device to make the relative luminosity measurement and to provide a trigger to distinguish polarized p+p events from beam related background events by means of timing measurements. Some other detectors are used for special triggers, *e.g.* pseudo Vertex Position Detectors (pVPDs) or upgraded pVPDs (upVPD) are used for TOF triggered events, and EMC is used to trigger on events with high transverse momentum (p_T) particles *etc.*.

The STAR Barrel Electro-Magnetic Calorimeter(BEMC) installed at barrel of the TPC is with pseudo-rapidity coverage $|\eta| < 1$ and full azimuth 2π coverage [70]. To supplement with BEMC, the Endcap Electro-Magnetic Calorimeter (EEMC) provides coverage with $1 < \eta < 2$ and the full azimuthal range [71]. Those two EMC systems can trigger on the high transverse momentum photons, electrons, and electromagnetically decaying hadrons.

The STAR Time-Of-Flight [72, 73, 74] (TOF) sub-system is based on Multi-gap Resistive Plate Chamber (MRPC) technique, which was first developed by

the CERN ALICE group. The Barrel TOF system installed between BEMC and TPC at STAR, covers $|\eta| < 0.9$ and full azimuth (2π) angle. The intrinsic time resolution and detecting efficiency for particles $p_T > 0.5$ GeV/c are $< 80ps$ and $> 95\%$, respectively. By using TOF PID method, we can largely improve our the capability of identifying particles. The upper limit of momentum (p) for π/K separation can be extended from 0.7 GeV/c to 1.6 GeV/c and 1.1 GeV/c to 3 GeV for proton/(π, K) separation. By combining with TPC, we can also identify electron at $p_T > 0.2$ GeV/c. TOF installation had been 100% completed and taking data in year 2010 (Run 10). One of the 120 trays didn't take data and was taken out for high voltage problem. The starting time of the TOF system is provided by the upVPD detector installed 5.7 m away from TPC center.

2.2.2 The Time Projection Champer (TPC)

TPC [75] is the main tracking device of the STAR detector. It was designed to record the tracks of particles, provide the information of their momenta and identify the particles by measuring their ionization energy loss (dE/dx) in the TPC gas. With the 4.2 m long cylinder and 4 m in radius, STAR TPC is the second largest single TPC in the world. The cylinder is concentric with the beam pipe, and the inner and outer radii of the active volume are 0.5 m and 2.0 m, respectively. Charged particles can be identified by TPC over a board momentum range $0.15 < p_T < 30$ GeV/c (0.075 GeV/c lower limit for magnet at 0.25 T). The TPC covers full azimuth angle $(0 < \phi < 2\pi)$ and the pseudo-rapidity range of $|\eta| < 2$ for inner radius and $|\eta| < 1$ for outer radius. Fig. 2.5 shows the cutaway view of the STAR TPC.

The TPC is divided into two parts by the central membrane, which is typically held at 28 kV high voltage. A chain of 183 resistors and equipotential rings along the inner and outer field cage create a uniform drift field (~ 135 V/cm) from the central membrane to the ground planes where anode wires and pad planes are
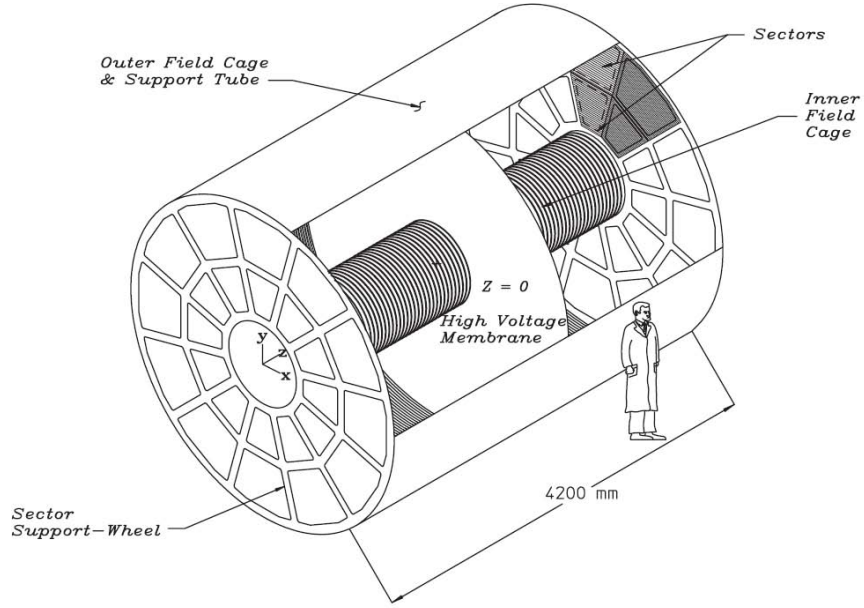
Figure 2.5: Cutaway view of the TPC detector. The figure is taken from [75].

organized into 12 sectors for each sub-volume of the TPC. The working gas of the TPC is two gas mixture the so called P10 gas (Ar $90\% + CH_4$ 10%) regulated at 2 mbar above the atmospheric pressure. The electron drift velocity in P10 is relatively fast, ~ 5.45 cm/μs at 130 V/cm. The gas mixture must satisfy multiple requirements and the gas gains are ~ 3770 and ~ 1230 for the inner and outer sectors working at normal anode voltage (1170 V for inner and 1390 V for outer), respectively.

Table 2.1: Comparison of the Inner and Outer subsector geometries.

Item	Inner Subsector	Outer Subsector	Comment
Pad Size	2.85 mm x 11.5 mm	6.20 mm x 19.5 mm	
Isolation Gap between pads	0.5 mm	0.5 mm	
Pad Rows	13 (#1-#13)	32 (#14-#45)	
Number of Pads	1,750	3,942	5,692 total
Anode Wire to Pad Plane Spacing	2 mm	4 mm	
Anode Voltage	1,170 V	1,390 V	20:1 signal:noise
Anode Gas Gain	3,770	1,230	
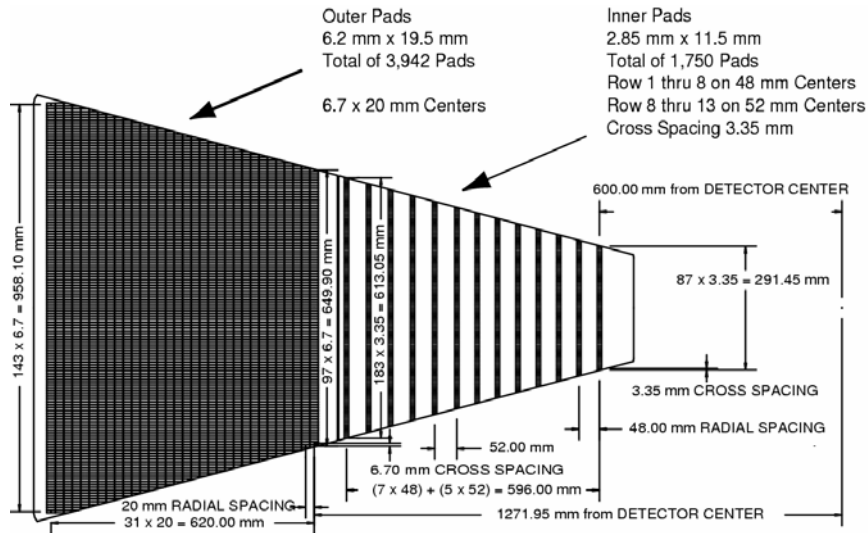
Figure 2.6: The anode pad plane of one full TPC sector. The inner sub-sector is on the right and it has small pads arranged in widely spaced rows. The outer sub-sector is on the left and it is densely packed with larger pads.

Each readout plane is instrumented with a thin Multi-Wire Proportional Chamber (MWPC) together with a pad plane readout. The drifting electrons avalanche in the high field at the 20 μm anode wires providing an amplification of 1000-3000. The chambers consists of a pad plane and three wire planes. Fig. 2.6 shows the pad plane of one full TPC sector. Each pad plane is also divided into inner and outer sub-sectors. The outer radius sub-sectors have continuous pad coverage to optimize the dE/dx resolution. This is optimal because the full track ionization signal is collected and more ionization electrons improve statistics on the dE/dx measurement. Another modest advantage of full pad coverage is an improvement in tracking resolution due to anti-correlation of errors between pad rows. The typical resolution is $\sim 0.5 - 1.0$ mm. The inner sector only serves to extend the position measurements along the track to small radii thus improving the momentum resolution and the matching to the inner tracking detectors. It also helps to detect particles with lower momentum. The parameters of the outer and inner sub-sectors are summarized in Table 2.1. $136,608 = 5692 \times 24$ readout pads provide (x, y) coordinate information, while z coordinate is provided by 512

time buckets and the drift velocity.
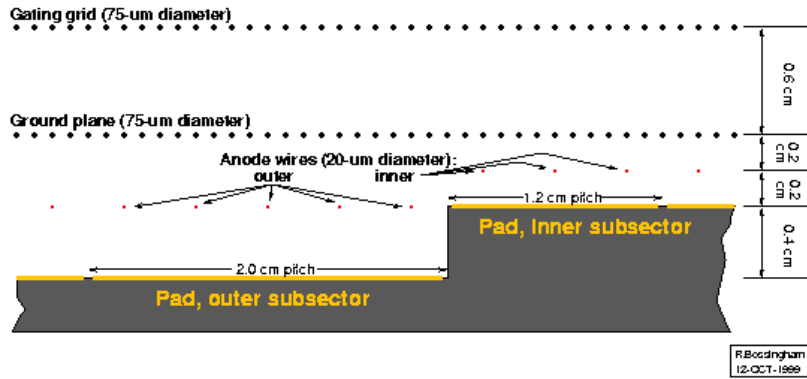
Figure 2.7: Cutaway view of wires relative to the inner and outer pad rows.

Fig. 2.11 shows a cutaway view of inner sub-sector and outer sub-sector pad plane. There are three layers wires plane above the read out pad plane, which are gating grid wires plane, ground wires plane and anode wires plane (from top to bottom). When charged particles traverse the TPC, they liberate the electrons from the TPC gas due to the ionization energy loss (dE/dx). These electrons are drifted towards the end cap planes of the TPC. There the signal induced on a readout pad is amplified and integrated by a circuit containing a pre-amplifier and a shaper. Then it is digitalized and then transmitted over a set of optical fibers to STAR *Data AcQuisition system* (DAQ).

At the DAQ stage, raw events containing ADC and TDC values from each detector were recorded as hits, vertices as well as the collision position. The TPC tracks reconstruction process begins by the 3D coordinate space points finding. This step results in a collection of points reported in global Cartesian coordinates. The Timing Projection chamber Tracker (TPT) algorithm is then used to reconstruct tracks by helical trajectory fit. The resulted track collection from the TPC is combined with any other available tracking detector reconstruction results and then refit by application of a Kalman filter routine a complete and robust statistical treatment. The primary collision vertex is then reconstructed

from these global tracks and a refit on these tracks with the distance of closest approach (dca) less than 3 cm is preformed by a constrained Kalman fit that forces the track to originate from the primary vertex. As expected, the vertex resolution decreases as the square root of the number of tracks used in the calculation. The primary vertex resolution is $\sim 350 \mu$m with more than 1000 tracks. The refit results are stored as primary tracks collection in the container. The reconstruction efficiency including the detector acceptance for primary tracks depends on the particle type, track quality cuts, p_T and track multiplicities $etc.$. The typical value for the primary pions with $N_{fit} > 24$ and $|\eta| < 0.7$, $dca < 3.0$ cm is approximate constant at $p_T > 0.4$ GeV/c: $\sim 90\%$ for Au+Au peripheral collisions and $\sim 80\%$ for central collisions, respectively.
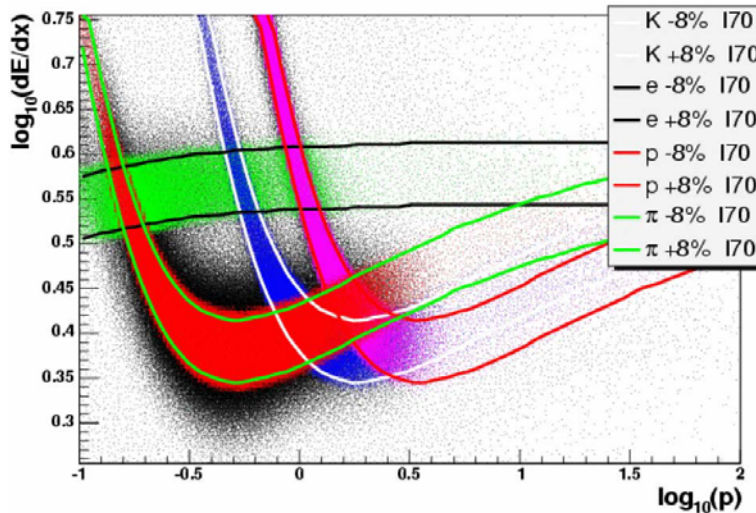
Figure 2.8: $log_{10}(dE/dx)$ (KeV/cm) as a function of $log_{10}(p)$ (GeV/c) for electron, pions, kaons and protons. The colored band are within the $\pm 1\sigma$ dE/dx resolution. $I70$ denotes Bichsel's prediction for 30% truncated dE/dx mean [76].

The TPC provides the track momentum and the dE/dx information for charged particles identification. For a particle with charge z (in units of e) and speed $\beta = v/c$ passing through, the mean rate of dE/dx is given by the Bethe-Bloch equation (2.1) [77]:

$$ -\frac{dE}{dx} = Kz^2 \frac{Z}{A} \frac{1}{\beta^2} \left[\frac{1}{2} \ln \frac{2m_e c^2 \beta^2 \gamma^2 T_{max}}{I^2} - \beta^2 - \frac{\delta}{2} \right] \tag{2.1} $$

The meaning of each symbol can be referred to Particle Data Book. Different types of particles (different rest masses) with the same momentum have different kinematic variables β (γ), which may cause distinguishable dE/dx. The typical resolution of dE/dx in Au+Au collisions is $\sim 8\%$, which makes the π/K separation up to $p \sim 0.7$ GeV/c and proton/meson separation up to $p \sim 1.1$ GeV/c. Fig. 2.8 shows measured dE/dx by TPC as a function of momentum.
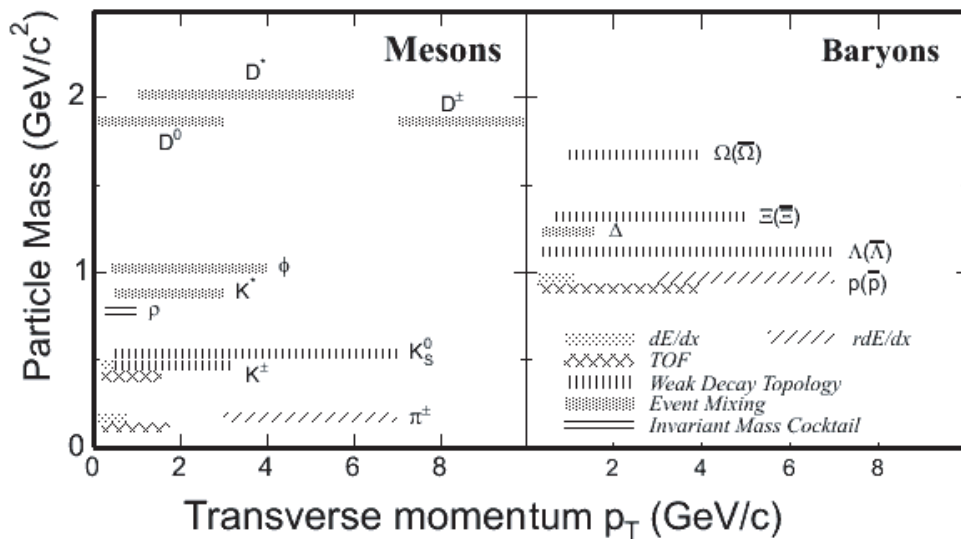
Figure 2.9: p_T reach of particle identification capability with STAR detectors. The upper edges of rdE/dx, weak decay topology, event mixing are limited by statistics. The figure is taken from [78].

A technique has been developed to identify high momentum ($p > 3$ GeV/c) pions and protons in the relativistic rising region of dE/dx [72, 79, 80] benefiting from the advantage that the mean value of dE/dx for different particles have a visible separation in the relativistic rising region as shown in Fig. 2.8 ($\sim 2\sigma$ separation for pions and protons). Due to large acceptance of the TPC, the K_S^0, $\Lambda(\bar{\Lambda})$ *etc.* can be identified across p_T region $0.3 < p_T < 7.0$ GeV/c (upper edge limited by statistics) by using the topology of the weak decay in the TPC.

Resonances (K^*, ϕ, Δ *etc.*) can be reconstructed through the event mixing technique [81]. Fig. 2.9 shows the PID capabilities with the TPC. In addition, the TOF PID capability is also shown in the figures which will be discussed in the next sub-section.

2.2.3   Time-Of-Flight (TOF) Detector

With a total of 120 trays installed at the outside barrel of the TPC (with 60 on east side and 60 on west side), STAR has completed its upgrade of full barrel Time-Of-Flight (TOF) detector with $|\eta| < 0.9$ and 2π azimuthal coverage based on the Multigap Resistive Plate Chamber (MRPC) technology in the year 2010 (Run 10). In Run10, 119 out of 120 trays were with good performance in data taking and only one tray was taken out for the high voltage cable problem. In the year 2009 (Run 9), 94 out of 120 trays were installed (72% coverage) and 86 of those installed trays were in the data taking.
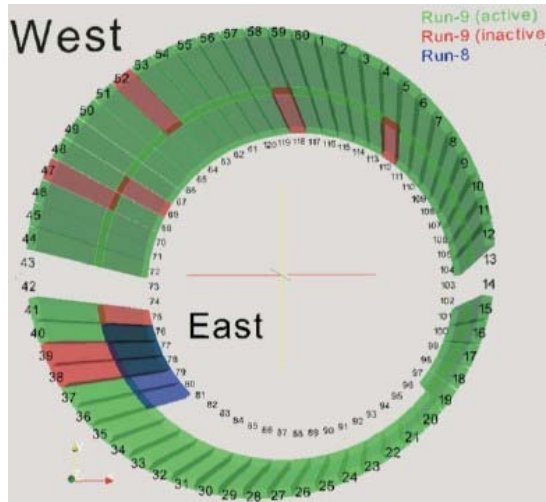
Figure 2.10: TOF trays distribution in Run 8 and Run 9.

Fig. 2.10 shows the TOF tray distribution installed in Run 8 and Run 9. Each tray covers 6 degree in azimuthal direction (ϕ) around the TPC [82].

A tray contains 32 MRPC modules and was placed along the beam line direc-

Tray, Module & Pad
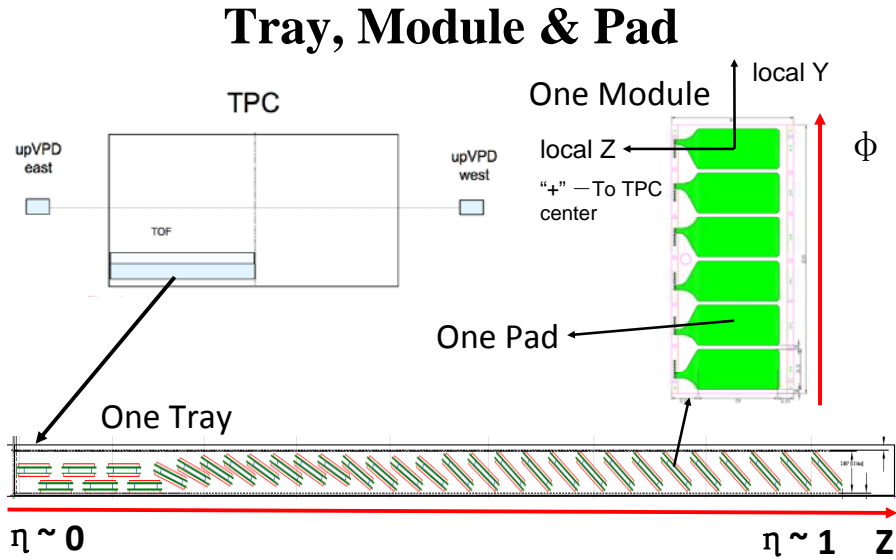
Figure 2.11: Geometry of TOF trays, modules and pads. The figure is taken from [83].

tion around TPC. In each module, there are 6 read-out pad along the azimuthal direction (ϕ). The detailed geometry and the definition of local coordinate system for each pad are shown in Fig. 2.11. Two VPDs [84] were installed since Run 2 to provide a starting time for TOF detectors, each staying 5.4 m away from the TPC center along the beam line. The VPD can also provide the independent Z component of the vertex. Each VPD consists of three detecting element tubes covering $\sim 19\%$ of the total solid angle in $4.43 < |\eta| < 4.94$. Due to different multiplicities, the effective timing resolution of total starting time is 25 ps, 85 ps and 140 ps for 200 GeV Au+Au, d+Au and p+p collisions, respectively.

MRPC technology was first developed by the CERN ALICE group. Fig. 2.12 shows the two side-view of a MRPC module which was adopted by STAR [85]. A MRPC basically consists a stack of resistive plates with a series of uniform gas gaps. It works in avalanche mode. Electrodes are applied to the outer surface of the outer plates. With a strong electric field applied on, the internal plates are
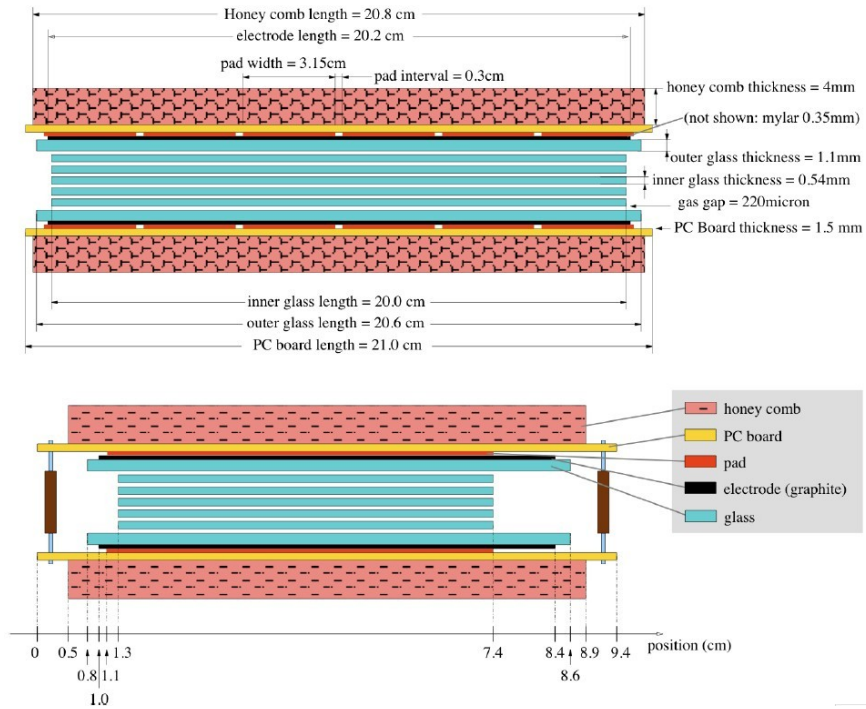
Figure 2.12: Two side-view of a MRPC moduel. The figure is taken from [85].

left electrically floating and they will keep the correct voltage due to the flow of electrons and ions created in avalanches. There are six read-out pads on each module in this design. The first beam test for 6-gap MRPCs at CERN PS-T10 facility with $p_{lab} = 7$ GeV/c pions beam resulted in a ~ 65 ps timing resolution with more than 95% detecting efficiency and the module is capable of working at high event rate (500 Hz/cm^2) [85]. These modules were then assembled in a prototype TOF tray and tested in the AGS radiation area. Similar resolution was obtained. In RHIC Run 3 and Run 4, the MRPC modules in TOF trays installed in the STAR detector were applied on the high voltage of 14 kV and with the working gas of 95% freon and 5% isobutane. The charged particle detecting efficiency is $> 95\%$ at high voltage plateau.

TOF system calibrations [86] include the start time calibration from VPD and TOF flight time calibration. The main sources need to be considered are global time offset due to different electronics delays, the correlation between the

Table 2.2: TOF system performance in different runs.

Operating condition			Timing Resolution (ps)		
			VPD	Overall	TOF
Run 3	200GeV d+Au		85	120	85
	200GeV p+p		140	160	80
Run 4	62GeV Au+Au		55	105	89
	200GeV Au+Au	Full-field	27	86	82
		Half-field	20	82	80
Run 5	200GeV Cu+Cu (ToT)		50	92	75
	62GeV Cu+Cu (ToT)		82	125	94
Run 8	200GeV d+Au (ToT)		N/A	N/A	N/A
	200GeV p+p (ToT)		83	112	75
Run 9	500GeV p+p		85	115	78
	200GeV p+p		81	110	74
Run 10	200GeV Au+Au		28	87	82

amplitude and the timing signals, the correlation between the hit position and the timing signals *etc.* Table. 2.2 lists the calibrated timing resolution results for VPD and TOF system since the year 2003 (Run 3). The results indicate that the intrinsic timing resolution of TOF was around 75 ps, which was quite stable since run 5.

Fig. 2.13 shows the hadron identification capability of TOF system in 200 GeV p+p collisions in Run 9. One can see clearly the bands for electron, pion, kaon, proton and deuteron. We conclude that the performance of TOF system has satisfied the STAR TOF system upgrade requirements.
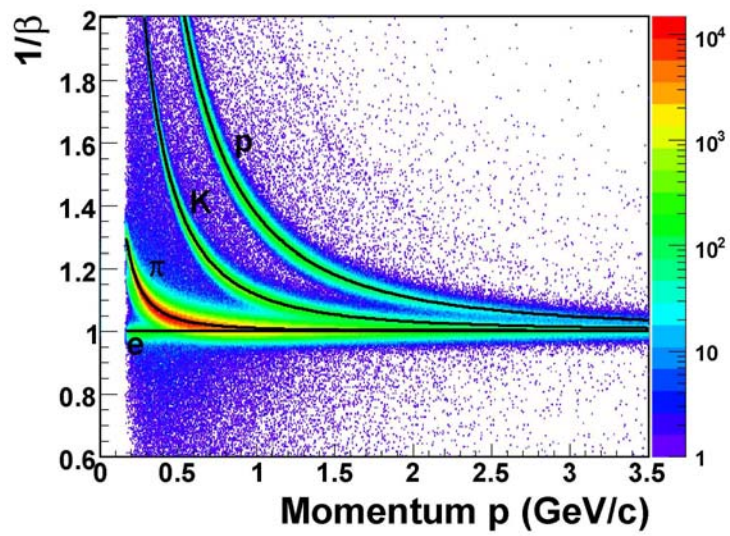
Figure 2.13: $1/\beta$ vs. momentum (p) from Run 9 200 GeV p + p collisions, where the $\beta = v/c$ and v is the speed of a particle.

CHAPTER 3

Moments Methodology in Heavy Ion Collision

In statistics [87], moments are used to characterize the shape of a probability distribution. For example, the second central moment (moment about the mean), variance (σ^2) is widely applied to describe the width of a probability distribution. The skewness (S) and kurtosis (κ) are used to describe how the distributions skewed and peaked from its mean value, respectively. Another alternative methods to the moments of a distribution is so called cumulant. The cumulants determine the moments in the sense that any two probability distributions whose cumulants are identical will have identical moments as well, and similarly the moments determine the cumulants. In heavy ion collision, the higher moments of distributions of conserved quantities, such as net-baryon, net-charge and net-strangeness, are predicted to be sensitive to the correlation length and to be connected to the thermodynamic susceptibilities computed in Lattice QCD [57] and in the Hadron Resonance Gas [58] (HRG) model. As the net-proton can also reflect the net-baryon and net-charge fluctuations, higher moments of net-proton distributions are used to search for the QCD critical point. In this chapter, We will show you the definitions and properties of the moments and cumulants. The connection between higher moments of net-proton distributions and the thermodynamic baryon number susceptibilities in Lattice QCD and HRG model as well as correlation length will be also discussed.

3.1 Cumulants and Moments

3.1.1 Definition

In probability theory and statistics, the cumulants of a probability density distribution can be defined by using the cumulant-generating function [88]. The cumulant-generating function of the random variable X is defined as:

$$G(t) = \log[E(e^{tX})] \tag{3.1}$$

, where the E is the expectation operator and some times denoted by angle brackets $<>$, $E(e^{tX}) =< e^{tX} >= \int\limits_{-\infty}^{+\infty} e^{tX} f(X)dX$, for a real-valued continuous probability density function $f(x)$. Generally, the nth order cumulants C_n can be extracted from the cumulant-generating function via differentiation (at zero) of $G(t)$.

$$C_n = G^{(n)}(0) = \left.\frac{\partial^n G(t)}{\partial t^n}\right|_{t=0} \tag{3.2}$$

Cumulants of a distribution are closely related to the moments of the distribution and the moment-generating function for moments about zero can be written as:

$$g(t) = E(e^{tX}) = 1 + \sum_{n=1}^{\infty} < X^n > \frac{t^n}{n!} \tag{3.3}$$

Consequently, the nth order moments about zero $\mu_n' =< X^n >$ can be obtained by

$$\mu_n' =< X^n >= g^{(n)}(0) = \left.\frac{\partial^n g(t)}{\partial t^n}\right|_{t=0} \tag{3.4}$$

Thus, the cumulant-generating function can be expressed in term of the moments about zero as:

$$
\begin{aligned}
G(t) &= \log[g(t)] = -\sum_{n=1}^{\infty}\frac{1}{n}(1-g(t))^n = \sum_{n=1}^{\infty}\frac{1}{n}(-\sum_{m=1}^{\infty}\mu'_m\frac{t^m}{m!})^n \\
&= \mu'_1 \times t + (\mu'_2 - {\mu'_1}^2) \times \frac{t^2}{2!} + (\mu'_3 - 3\mu'_2\mu'_1 + 2{\mu'_1}^3) \times \frac{t^3}{3!} + ... \quad (3.5)
\end{aligned}
$$

Finally, we obtain the connections between the cumulants, moments about zero μ'_n and central moments (moments about mean) $\mu_n =< (X- < X >)^n >=< (\delta X)^n >$:

$$
\begin{aligned}
C_1 &= \mu'_1 =< X > & (3.6) \\
C_2 &= \mu'_2 - {\mu'_1}^2 =< (X- < X >)^2 > & (3.7) \\
C_3 &= \mu'_3 - 3\mu'_2\mu'_1 + 2{\mu'_1}^3 =< (X- < X >)^3 > & (3.8) \\
C_4 &= \mu'_4 - 4\mu'_3\mu'_1 - 3{\mu'_2}^2 + 12\mu'_2{\mu'_1}^2 - 6{\mu'_1}^4 \\
&= < (X- < X >)^4 > -3 \times (< (X- < X >)^2 >)^2 & (3.9)
\end{aligned}
$$

$$
\vdots
$$

$$
\begin{aligned}
C_n &= \mu'_n - \sum_{m=1}^{n-1}\binom{n-1}{m-1}C_m\mu'_{n-m} \\
&= \mu_n - \sum_{m=1,(n-m,n\geq 2)}^{n-1}\binom{n-1}{m-1}C_m\mu_{n-m} & (3.10)
\end{aligned}
$$

In general, we may also consider the joint cumulants, for example, the generating-function of joint cumulants for random variables, $X_1, X_2, ...X_n, (n \geq 2)$ is defined as:

$$
G(t_1, t_2, ..t_n) = \log < e^{\sum_{j=1}^{n} t_j X_j} > \quad (3.11)
$$

Then, the joint cumulants of random variables, $X_1, X_2, ... X_n$, $(n \geq 2)$ can be expressed as:

$$
\begin{aligned}
C(X_1, X_2 ..., X_n) &= \sum_{\pi} (|\pi| - 1)! (-1)^{|\pi| - 1} \prod_{B \in \pi} E(\prod_{i \in B} X_i) \\
&= \sum_{\pi} (|\pi| - 1)! (-1)^{|\pi| - 1} \prod_{B \in \pi, |B| \geq 2} E(\prod_{i \in B} \delta X_i) \quad (3.12)
\end{aligned}
$$

, where π runs through the list of all partitions of $\{1, 2, ..., n\}$, B runs through the list of all blocks of partitions π, $|\pi|$ is the number of parts in the partition and $|B|$ is the number of parts in the block B. For example, if we only have two random variables X, Y, then various order joint cumulants are:

$$
\begin{aligned}
C(X, Y) &= C_{1X,1Y} = < \delta X \delta Y > & (3.13) \\
C(X, Y, Y) &= C_{1X,2Y} = < \delta X (\delta Y)^2 > & (3.14) \\
C(X, X, Y, Y) &= C_{2X,2Y} = < (\delta X)^2 (\delta Y)^2 > \\
&\quad - 2 < \delta X \delta Y >^2 - < (\delta X)^2 >< (\delta Y)^2 > & (3.15) \\
C(X, Y, Y, Y) &= C_{1X,3Y} = < \delta X (\delta Y)^3 > - 3 < \delta X \delta Y >< (\delta Y)^2 > & (3.16)
\end{aligned}
$$

, where the $\delta X = X - < X >, \delta Y = Y - < Y >$.

Usually, the central moments are more useful than the moments about zero to describe the shape of the distributions. The second central moment (variance (σ^2)) is used to describe the width of a distributions. The normalized third central moment and forth central moment so called skewness (S) and kurtosis (κ), are used to describe the asymmetry and peakness of distributions, respectively.

They are defined as:

$$
\sigma^2 \;\; = \;\; <(X-<X>)^2> = C_2 \tag{3.17}
$$

$$
S \;\; = \;\; \frac{<(X-<X>)^3>}{\sigma^3} = \frac{C_3}{(C_2)^{3/2}} \tag{3.18}
$$

$$
\kappa \;\; = \;\; \frac{<(X-<X>)^4>}{\sigma^4} - 3 = \frac{C_4}{(C_2)^2} \tag{3.19}
$$

Negative Skew   Positive Skew
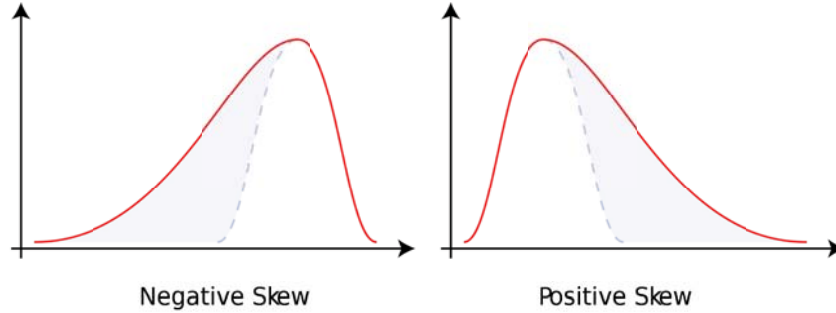
Figure 3.1: Visual example of distribution with negative skewness (left panel) and positive skewness (right panel). The figure is taken from [89].

Fig. 3.1, it gives a visual example for determining which of the two kinds of skewness a distribution has. The distribution shown in the left panel, which gives negative skewness, is said to be left-skewed. It has a longer left tail and the center of the distribution is concentrated on the right of the distribution. The distribution in the right panel of Fig. 3.1 shows you a distribution with positive skewness, which is said to be right-skewed. It has a longer right tail and the center of the distribution is concentrated on the left of the distribution. A zero value indicates that the values are relatively evenly distributed on both sides of the mean, typically but not necessarily implying a symmetric distribution.

Fig. 3.2 shows the kurtosis of seven well-known distributions from different parametric families. All distributions here are symmetric and with unity variance and zero mean and skewness. From top to bottom, those distributions are Laplace distribution (D), hyperbolic secant distribution (S), logistic distribution (L), normal distribution (N), raised cosine distribution (C), Wigner semicircle
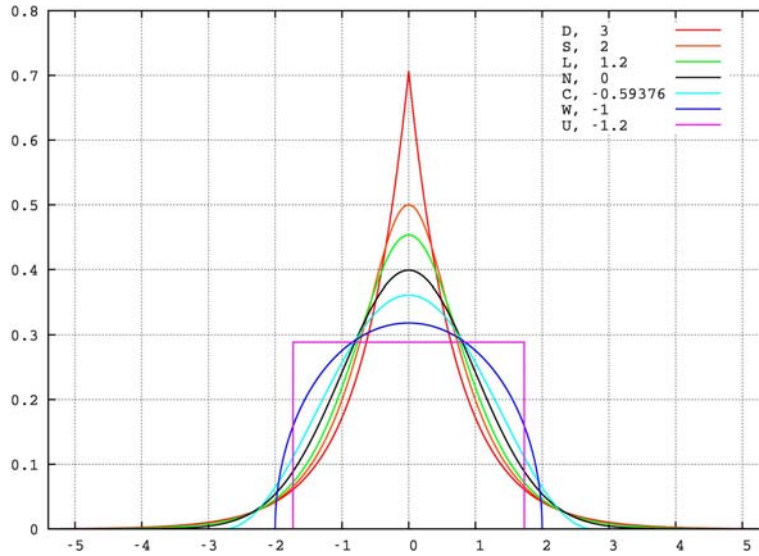
Figure 3.2: Visual example of kurtosis for seven well-known distributions from different parametric family. The figure is taken from [90].

distribution (W) and uniform distribution (U). It is found that the distributions with a sharp peak have a larger kurtosis value than those distributions with broad tails. In Fig. 3.2, the kurtosis values for Laplace distribution, normal distribution and uniform distribution are 3, 0, -1.2, respectively. A high kurtosis distribution has a sharper peak and longer, fatter tails, while a low kurtosis distribution has a more rounded peak and shorter thinner tails. The kurtosis must be at least -2, which can be realized by the Bernoulli distribution with $p = 1/2$. There is no upper limit to the kurtosis and it may be infinite.

For normal distributions, both, the skewness and the kurtosis are equal to zero. Thus, they are ideal probes of the non-gaussian fluctuations.

3.1.2 Properties of Cumulants and Moments

In this sub-section, We will introduce several important properties for cumulants and moments, which will be used in our following analysis. There are many good properties for cumulants, such as shift-invariance, homogeneity and additivity.

1. Shift-invariance: This means that, if we denote by C_n the nth cumulant of the probability distribution of the random variable X, then for any constant c we have:

$$C_n(X + c) = C_n, n > 1 \tag{3.20}$$

In other words, shifting a random variable (adding c) shifts the first cumulant (the mean) and doesn't affect any of the others.

2. Homogeneity: For any constant c, we have:

$$C_n(cX) = c^n C_n(X) \tag{3.21}$$

This means the nth cumulant is homogeneous of degree n.

3. Additivity: If X and Y are independent random variables, then:

$$C_n(X + Y) = C_n(X) + C_n(Y) \tag{3.22}$$

In general case (X, Y are not necessary independent), we have:

$$C_n(X + Y) = \sum_{j=0}^{n} \binom{n}{j} C(\underbrace{X, X, ..., X}_{j}, \underbrace{Y, Y, ..., Y}_{n-j}) = \sum_{j=0}^{n} \binom{n}{j} C_{j,X,n-j,Y} \tag{3.23}$$

For example,

From equ. (3.17)-(3.19), we know the various moments (σ^2, S, κ) can be expressed as a function of cumulants. For the variance $\sigma^2 = C_2$, this is assured with the above three properties. Skewness (S) and kurtosis(κ) are self-invariant and homogenous but not for the additive. For example, if we have n independent identical random variance $X_1, X_2, ...X_n$, then we can get the sum of those random variables $Y = X_1 + X_2 + ... + X_n$ and the skewness and kurtosis of random variance

Y can be written as:

$$S(Y = \sum_{m=1}^{n} X_m) \quad = \quad \frac{\sum\limits_{m=1}^{n} C_3(X_m)}{(\sum\limits_{m=1}^{n} C_2(X_m))^{3/2}} \tag{3.24}$$

$$\kappa(Y = \sum_{m=1}^{n} X_m)) \quad = \quad \frac{\sum\limits_{m=1}^{n} C_4(X_m)}{(\sum\limits_{m=1}^{n} C_2(X_m))^2} \tag{3.25}$$

If $X_1, X_2, ...X_n$ are all with the same distribution as random variance X, we have:

$$S(Y = \sum_{m=1}^{n} X_m) \quad = \quad \frac{n \times C_3(X)}{n^{3/2} \times (C_2(X))^{3/2}} = \frac{1}{\sqrt{n}} \times S(X) \tag{3.26}$$

$$\kappa(Y = \sum_{m=1}^{n} X_m) \quad = \quad \frac{n \times C_4(X)}{n^2 \times (C_2(X))^2} = \frac{1}{n} \times \kappa(X) \tag{3.27}$$

More generally, if $X_1, X_2, ...X_n$ are independent random variables, not necessarily identically distributed, but all having the same variance then:

$$S(Y = \sum_{m=1}^{n} X_m) \quad = \quad \frac{1}{n^{3/2}} \times \sum_{m=1}^{n} \frac{C_3(X_m)}{(C_2(X_m))^{3/2}} = \frac{1}{n^{3/2}} \times \sum_{m=1}^{n} S(X_m) \tag{3.28}$$

$$\kappa(Y = \sum_{m=1}^{n} X_m) \quad = \quad \frac{1}{n^2} \times \sum_{m=1}^{n} \frac{C_4(X_m)}{(C_2(X_m))^2} = \frac{1}{n^2} \times \sum_{m=1}^{n} \kappa(X_m) \tag{3.29}$$

The equ. 3.28 and 3.29 show that the skewness and kurtosis of the sum are smaller, as they approach a Gaussian distribution in accordance with the central limit theorem. On the other hand, for moment-generating function $g(t)$ (moment about zero), we have:

$$g_Y(t) = g_{X_1}(a_1 t)g_{X_2}(a_2 t)...g_{X_n}(a_n t) \tag{3.30}$$

, where the $Y = \sum\limits_{m=1}^{n} a_m X_m$ are the sum of independent random variables (not necessarily identically distributed) and a_m are constants. For random variable

$Z = X_1 - X_2$, where X_1, X_2 are two independent random variables, we get:

$$g_Z(t) = g_{X_1}(t)g_{X_2}(-t) \tag{3.31}$$

It means that if we know the moment-generating function for X_1, X_2, the moment of the distribution for a random variable $X_1 - X_2$ can be calculated through the moment-generating function from equ. 3.30, even without knowing the underlying distribution of the $X_1 - X_2$.

3.2 Applications in Heavy Ion Collision

Experimentally, we measure particle multiplicities event-by-event wise. In the following, we use N to represent the particle number in one event. The average value over the whole event ensemble is denoted by $< N >$, where the single angle brackets are used to indicate ensemble average of a event-by-event distributions.

The deviation of N from its mean value is defined by

$$\delta N = N - < N > \tag{3.32}$$

Then, we can define the various order cumulants of event-by-event distributions of a variable N.

$$
\begin{aligned}
C_{1,N} &= <N> \tag{3.33}\\
C_{2,N} &= <(\delta N)^2> \tag{3.34}\\
C_{3,N} &= <(\delta N)^3> \tag{3.35}\\
C_{4,N} &= <(\delta N)^4> -3<(\delta N)^2>^2 \tag{3.36}
\end{aligned}
$$

Once we have the definition of cumulants, various moments can be denoted

as:

$$M = C_{1,N}, \sigma^2 = C_{2,N}, S = \frac{C_{3,N}}{(C_{2,N})^{3/2}}, \kappa = \frac{C_{4,N}}{(C_{2,N})^2} \tag{3.37}$$

, where M is the mean value.

And also, the moments product $\kappa\sigma^2$ and $S\sigma$ can be expressed in terms of cumulant ratios.

$$\kappa\sigma^2 = \frac{C_{4,N}}{C_{2,N}}, S\sigma = \frac{C_{3,N}}{C_{2,N}} \tag{3.38}$$

With above definition of various moments, we can calculate various moments and moment products with the measured event-by-event particle number fluctuations in a certain p_T and rapidity range for each centrality. Higher moments of conserved quantities, such as net-baryon, net-charge and net-strangeness number are predicted to be sensitive to the correlation length developed in heavy ion collisions and are directly linked to the thermodynamic susceptibilities computed in Lattice QCD [57] and in the Hadron Resonance Gas (HRG) [58] model. As the net-proton fluctuations can also reflect the net-baryon and net-charge fluctuations in heavy ion collision [59], higher moments of net-proton distributions can be used to search for the QCD critical point.

The window in rapidity should be at least about one unit wide, in order for the results to apply without significant acceptance corrections. Furthermore, the longitudinal expansion of the matter produced in the collision reduces correlations among particles separated by much more than one unit in rapidity, making larger windows unnecessary.

3.2.1 Connection to the Thermodynamic Susceptibility in the Lattice QCD and HRG Model

Higher moments of conserved quantities distributions are directly connected to the thermodynamic susceptibilities, such as net-baryon, net-charge and net-strangeness number susceptibilities calculated in Lattice QCD [57, 91] and Hadron Resonance Gas (HRG) model [58]. P/T^4 is the dimensionless pressure, which is expressed by the logarithm of the QCD partition function:

$$\frac{P}{T^4} = \frac{1}{VT^3} \ln \left[Z(V, T, \mu_B, \mu_S, \mu_Q) \right] \tag{3.39}$$

Then, the susceptibilities of those conserved quantities in Lattice and HRG model can be calculated by the derivation of the dimensionless pressure [91]:

$$\chi_q^{(n)}(T, \mu_B, \mu_S, \mu_Q) = \left. \frac{\partial^n (P/T^4)}{\partial (\mu_q/T)^n} \right|_T \tag{3.40}$$

, where the μ_q/T $(q = B, S, Q)$ is the normalized chemical potential and the $\chi_q^{(n)}(T, \mu_B, \mu_S, \mu_Q)$ are the nth order susceptibilities for net-baryon (B), net-strangeness (S) and net-charge (Q) number. In principle, those susceptibilities are Taylor coefficients in the expansion of P/T^4 with respected to μ_q/T at fixed T.

The Lattice QCD results [91] are obtained from (2+1) flavor calculations with dynamical light and strange quark degrees of freedom and an improved staggered fermion action (p4 action) that strongly reduces lattice cutoff effects in bulk thermodynamics at high temperature. The value of the strange and light quark masses are mostly physical. The strange quark mass (m_s) is fixed to physical value while the light up and down quark masses are treated as degenerate and equal to $m_s/10$.

In the grand canonical ensemble framework, the n-th order cumulant of net-

baryon (B), net-strangeness (S) and net-charge number (Q) distributions are connected to the corresponding susceptibilities by:

$$C_{n,q} = VT^3 \chi_q^{(n)}(T, \mu_B) \tag{3.41}$$

, where the V denotes the volume of the system, $q = B, S, Q$. As it is very difficult to determine the volume, experimentally, we use the ratios:

$$(S\sigma)_q \;=\; \frac{C_{3,q}}{C_{2,q}} = \frac{\chi_q^{(3)}}{\chi_q^{(2)}} \tag{3.42}$$

$$(\kappa\sigma^2)_q \;=\; \frac{C_{4,q}}{C_{2,q}} = \frac{\chi_q^{(4)}}{\chi_q^{(2)}} \tag{3.43}$$

$$(\frac{\kappa\sigma}{S})_q \;=\; \frac{C_{4,q}}{C_{3,q}} = \frac{\chi_q^{(4)}}{\chi_q^{(3)}} \tag{3.44}$$

to make a direct comparison between experimental data and theory. The left hand sides are the measured moment products for net-baryon, net-strangeness and net-charge number distributions and the right hand sides are the corresponding theoretical susceptibility ratios.
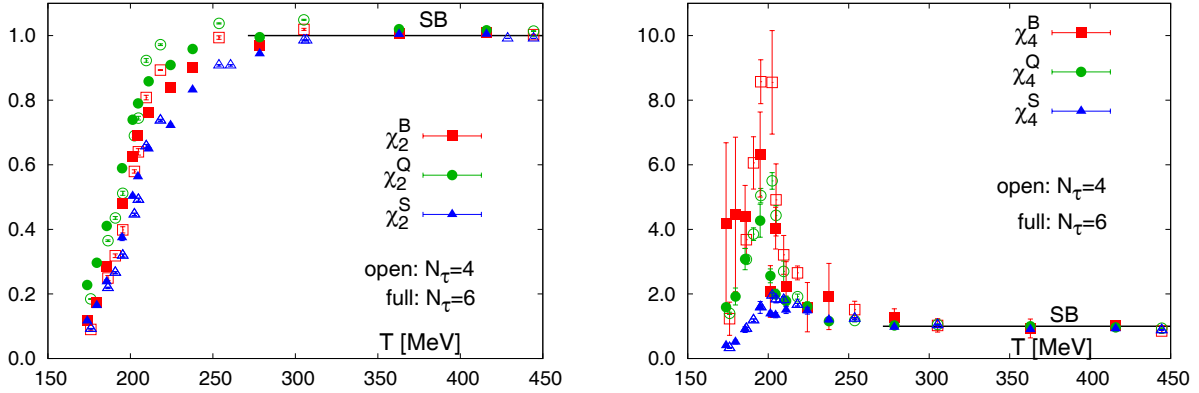
Figure 3.3: Quadratic and quartic fluctuations of net-baryon, net-strangeness and net-charge number at $\mu_B = 0$. The figures are taken from [91].

Quadratic (χ_4) and quartic (χ_2) susceptibilities of net-baryon (B), net-strangeness(S) and net-charge (Q) number evaluated at zero baryon chemical potential $\mu_B = 0$

are shown in Fig. 3.3. It can be found that, in all cases quadratic fluctuations rise rapidly in the transition region where the quartic fluctuations show a maximum. This maximum is most pronounced for the baryon number fluctuations but is still visible also in fluctuations of the strangeness number. We note that results obtained on lattices with temporal extent $N_\tau = 6$ are in good agreement with those obtained on the coarser $N_\tau = 4$ lattice. For the value of quark masses used here, the transition temperature T_c at $\mu_B = 0$ is about 200 MeV. For temperature above $1.5T_c$, we may find that in Fig. 3.3, the quadratic and quartic fluctuations of baryon, strangeness and charge number can be described by an ideal, massless quark gas, for which the pressure is given by:

$$\frac{P^{SB}}{T^4} = \sum_{f=u,d,s} [\frac{7\pi^2}{60} + \frac{1}{2}(\frac{\mu_f}{T})^2 + \frac{1}{4\pi^2}(\frac{\mu_f}{T})^4] \tag{3.45}$$

, which is so called Stefan-Boltzmann (SB) limit.

Particle abundance in heavy ion collisions at chemical freeze-out, when the inelastic interactions between particles cease, can be well described by HRG model for large range of energies with energy dependent input thermodynamic parameter temperature (T) and baryon chemical potential (μ_B) [43, 44]. By fitting with the experimental data, we can parameterize the chemical freeze-out curve $T(\mu_B)$ in the $T - \mu_B$ plane and μ_B as [58]:

$$T(\mu_B) = a - b\mu_B^2 - c\mu_B^4 \tag{3.46}$$

$$\mu_B(\sqrt{s_{NN}}) = \frac{d}{1 + e\sqrt{s_{NN}}} \tag{3.47}$$

, where $a = (0.166 \pm 0.002)$ GeV, $b = (0.139 \pm 0.016)$ GeV, $c = (0.053 \pm 0.021)$ GeV^{-1}, $d = (1.308 \pm 0.028)$ GeV^{-3} and $e = (0.273 \pm 0.008)$ GeV^{-1}. This parameterization agrees with the phenomenological freeze-out condition of fixed energy per particle of about 1 GeV $(E/A = 1$ GeV$)$. By requiring strangeness
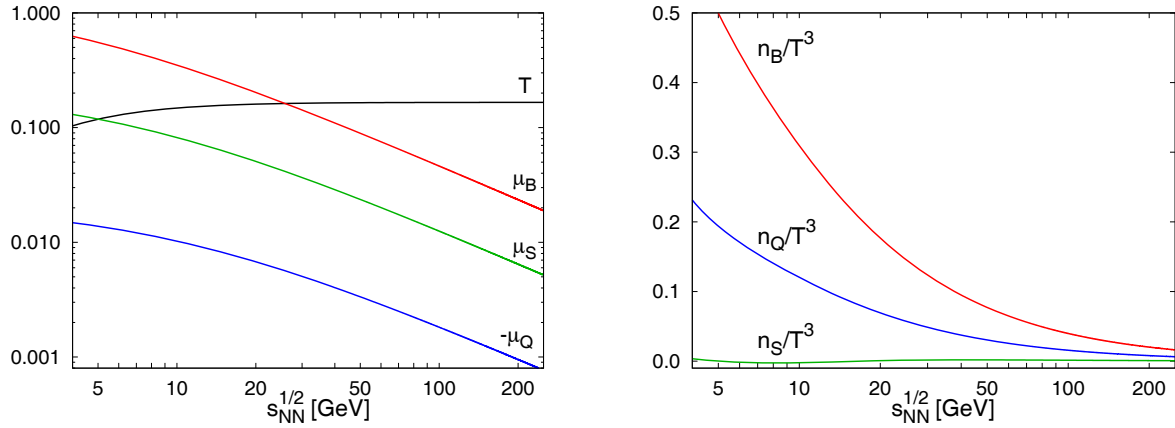
Figure 3.4: The energy dependence of the baryon, strangeness and charge chemical potential at the chemical freeze-out (left part) and the corresponding number density in the right part of the figure. The figures are taken from [58].

neutrality and isospin asymmetry in the inial state of Au+Au collisions, we can calculate the strange and electric-charge chemical potential from the HRG model. Fig. 3.4 shows baryon, strangeness and charge chemical potential (left part) and the baryon, strangeness and charge number density (right part) along with the chemical freeze-out curve. Based on the HRG model, we can also evaluate the μ_S/μ_B ratio chemical freeze-out curve:

$$\frac{\mu_S}{\mu_B} \approx 0.164 + 0.018\sqrt{s_{NN}} \tag{3.48}$$

, which shows a weak energy dependence.

In the HRG model [58], the particles are treated as a non-interacting hadron-resonance gas in thermal equilibrium, for which the equation of state is simple. The pressure can be obtained analytically within the grand canonical ensemble framework as:

$$
\begin{aligned}
\frac{P}{T^4} &= \frac{1}{\pi^2}\sum_i g_i(m_i/T)^2 K_2(m_i/T) \\
&\times \cosh[(B_i\mu_B + S_i\mu_S + Q_i\mu_Q)/T]
\end{aligned}
\tag{3.49}
$$

,where the B_i, S_i, Q_i, m_i are baryon, strangeness, charge quantum number and mass, the μ_B, μ_S, μ_Q denote the baryon, strange and charge chemical potential for the system, the K_2 are modified bessel functions and g_i is spin-isospin degeneracy for each particle. The contribution of anti-particle is explicitly included in the equ. (3.49) and the summation index i^{th} is for all stable hadrons and resonance. The HRG model used here includes all mesons and baryons mass from particle data book with mass $m_i \leq 2.5\text{GeV}$. From equ. 3.42 to 3.49, we obtain:

$$(S\sigma)_q = \frac{\chi_q^{(3)}}{\chi_q^{(2)}} = \frac{\sum_i F(m_i, T) \times q_i^3 \times \sinh[(\vec{q} * \vec{\mu}_q)/T]}{\sum_i F(m_i, T) \times q_i^2 \times \cosh[(\vec{q} * \vec{\mu}_q)/T]} \tag{3.50}$$

$$(\kappa\sigma^2)_q = \frac{\chi_q^{(4)}}{\chi_q^{(2)}} = \frac{\sum_i F(m_i, T) \times q_i^4 \times \cosh[(\vec{q} * \vec{\mu}_q)/T]}{\sum_i F(m_i, T) \times q_i^2 \times \cosh[(\vec{q} * \vec{\mu}_q)/T]} \tag{3.51}$$

$$(\frac{\kappa\sigma}{S})_q = \frac{\chi_q^{(4)}}{\chi_q^{(3)}} = \frac{\sum_i F(m_i, T) \times q_i^4 \times \cosh[(\vec{q} * \vec{\mu}_q)/T]}{\sum_i F(m_i, T) \times q_i^3 \times \sinh[(\vec{q} * \vec{\mu}_q)/T]} \tag{3.52}$$

, where $q_i = B_i, S_i, Q_i$, the quantum number for stable hadrons and resonances, $\vec{q} = (B_i, S_i, Q_i)$, the vector of the three quantum number, $\vec{\mu}_q = (\mu_B, \mu_S, \mu_Q)$, the chemical potential vector of the system and $F(m_i, T) = \frac{g_i(m_i/T)^2 K_2(m_i/T)}{\pi^2}$.

As there is a factor $q_i = B_i, S_i, Q_i$ in each term of the right hand side of the equ.3.50 to 3.52, the fluctuations of the conserved quantities, such as net-baryon, net-strangeness and net-charge, are only contributed from the particles carrying corresponding quantum number (B_i, S_i, Q_i).

To simplified the results in equ. 3.50 to 3.52, let us discuss the net-baryon, net-strangeness and net-charge number fluctuations one by one [58].

1. Baryon number fluctuations: In the HRG model, only baryons with baryon

number B=1 contribute to the baryon number fluctuations, we have:

$$
(S\sigma)_B = \frac{\chi_B^{(3)}}{\chi_B^{(2)}} = \frac{\sum_{i\in baryons} F(m_i,T) \times \sinh[(\mu_B + S_i\mu_S + Q_i\mu_Q)/T]}{\sum_{i\in baryons} F(m_i,T) \times \cosh[(\mu_B + S_i\mu_S + Q_i\mu_Q)/T]} \tag{3.53}
$$

$$
(\kappa\sigma^2)_B = \frac{\chi_B^{(4)}}{\chi_B^{(2)}} = 1 \tag{3.54}
$$

$$
(\frac{\kappa\sigma}{S})_B = \frac{\chi_B^{(4)}}{\chi_B^{(3)}} = \frac{\chi_B^{(4)}}{\chi_B^{(2)}} \times \frac{\chi_B^{(2)}}{\chi_B^{(3)}} = \frac{(\kappa\sigma^2)_B}{(S\sigma)_B} = \frac{1}{(S\sigma)_B} \tag{3.55}
$$

$$
(\frac{\sigma^2}{M})_B = \frac{\chi_B^{(2)}}{\chi_B^{(1)}} = \frac{\chi_B^{(4)}}{\chi_B^{(3)}} = (\frac{\kappa\sigma}{S})_B = \frac{1}{(S\sigma)_B} \tag{3.56}
$$

For $\mu_Q \ll \mu_S \ll \mu_B$, then:

$$
(S\sigma)_B = \tanh(\frac{\mu_B}{T}) \tag{3.57}
$$

Theoretical calculations have demonstrated that the net-proton fluctuations in heavy ion collision can reflect the net-baryon fluctuations.
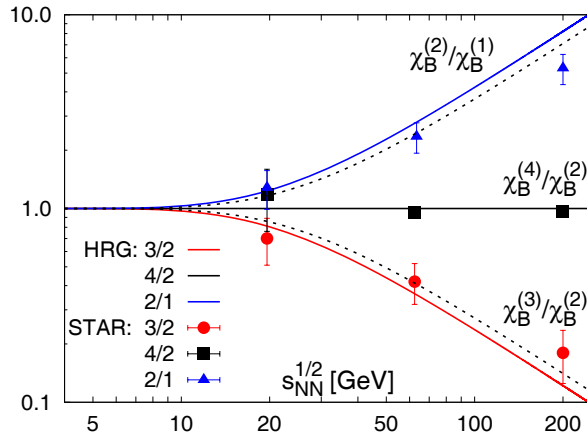
Figure 3.5: The ratio of quadratic fluctuations and mean net-baryon number($(\sigma^2/M)_B$),cubic to quadratic ($(S\sigma)_B$)and quartic to quadratic ($(\kappa\sigma^2)_B$) baryon number fluctuations calculated in the HRG model on the freeze-out curve and compared to results obtained by the STAR collaboration. The dashed curves show the approximate results for $(\kappa\sigma^2)_B = 1$ and $(S\sigma)_B = \tanh(\mu_B/T)$, respectively. The figure is taken from [58].

Fig. 3.5 shows a comparison of the energy dependence of quadratic fluctua-

tions (σ^2) normalized to the net-baryon number (M_B), moment products ($S\sigma)_B$ and ($\kappa\sigma^2)_B$ obtained in HRG model at chemical freeze-out with the STAR data. In Fig. 3.5, the $\kappa\sigma^2$ of net-proton distributions from STAR data are averaged within all collision centralities. The HRG model provides a good description of properties of different moment products of net-proton number fluctuations measured at RHIC energies.

2. Strangeness number fluctuations: Particles carry strange quantum number, such as strange meson and strange baryon, can contribute to the strange number fluctuations. Thus, we have:

$$(S\sigma)_S = \frac{\sum\limits_{baryon} q_s^3 F(m_i, T)\sinh(\frac{\mu_B}{T} + q_s\frac{\mu_S}{T}) + \sum\limits_{meason} q_s^3 F(m_i, T)\sinh(q_s\frac{\mu_S}{T})}{\sum\limits_{baryon} q_s^2 F(m_i, T)\cosh(\frac{\mu_B}{T} + q_s\frac{\mu_S}{T}) + \sum\limits_{meason} q_s^2 F(m_i, T)\cosh(q_s\frac{\mu_S}{T})} \tag{3.58}$$

$$(\kappa\sigma^2)_S = \frac{\sum\limits_{baryon} q_s^4 F(m_i, T)\cosh(\frac{\mu_B}{T} + q_s\frac{\mu_S}{T}) + \sum\limits_{meason} q_s^4 F(m_i, T)\cosh(q_s\frac{\mu_S}{T})}{\sum\limits_{baryon} q_s^2 F(m_i, T)\cosh(\frac{\mu_B}{T} + q_s\frac{\mu_S}{T}) + \sum\limits_{meason} q_s^2 F(m_i, T)\cosh(q_s\frac{\mu_S}{T})} \tag{3.59}$$

$$(\frac{\kappa\sigma}{S})_S = \frac{\sum\limits_{baryon} q_s^4 F(m_i, T)\cosh(\frac{\mu_B}{T} + q_s\frac{\mu_S}{T}) + \sum\limits_{meason} q_s^4 F(m_i, T)\cosh(q_s\frac{\mu_S}{T})}{\sum\limits_{baryon} q_s^3 F(m_i, T)\sinh(\frac{\mu_B}{T} + q_s\frac{\mu_S}{T}) + \sum\limits_{meason} q_s^3 F(m_i, T)\sinh(q_s\frac{\mu_S}{T})} \tag{3.60}$$

$$(\frac{\sigma^2}{M})_S = \frac{\sum\limits_{baryon} q_s^2 F(m_i, T)\cosh(\frac{\mu_B}{T} + q_s\frac{\mu_S}{T}) + \sum\limits_{meason} q_s^2 F(m_i, T)\cosh(q_s\frac{\mu_S}{T})}{\sum\limits_{baryon} q_s F(m_i, T)\sinh(\frac{\mu_B}{T} + q_s\frac{\mu_S}{T}) + \sum\limits_{meason} q_s F(m_i, T)\sinh(q_s\frac{\mu_S}{T})} \tag{3.61}$$

, where the q_s denote the strange quantum number of particles.

3. Electric-charge fluctuations: Particles carry electric-charge including mesons and baryons can contribute to the electric-charge fluctuations. We consider par-
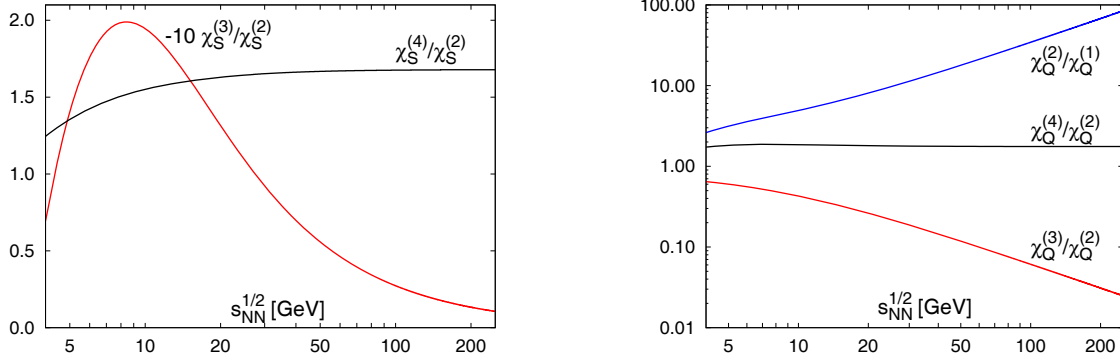
Figure 3.6: The ratios of moment products of strangeness and charge fluctuations along the chemical freeze-out curve, where the chemical potential and the temperature are parameterized as a function of colliding energy. The figures are taken from [58].

ticles with electric charge $Q = 1$ and $Q = 2$:

$$(S\sigma)_Q = \frac{\sum_{Q=1} F(m_i,T)\sinh[\frac{\vec{q}*\vec{\mu}_q}{T}] + 2^3 \sum_{Q=2} F(m_i,T)\sinh[(\frac{\vec{q}*\vec{\mu}_q}{T}]}{\sum_{Q=1} F(m_i,T)\cosh[\frac{\vec{q}*\vec{\mu}_q}{T}] + 2^2 \sum_{Q=2} F(m_i,T)\cosh[\frac{\vec{q}*\vec{\mu}_q}{T}]} \quad (3.62)$$

$$(\kappa\sigma^2)_Q = \frac{\sum_{Q=1} F(m_i,T)\cosh[\frac{\vec{q}*\vec{\mu}_q}{T}] + 2^4 \sum_{Q=2} F(m_i,T)\cosh[(\frac{\vec{q}*\vec{\mu}_q}{T}]}{\sum_{Q=1} F(m_i,T)\cosh[\frac{\vec{q}*\vec{\mu}_q}{T}] + 2^2 \sum_{Q=2} F(m_i,T)\cosh[\frac{\vec{q}*\vec{\mu}_q}{T}]} \quad (3.63)$$

$$(\frac{\kappa\sigma}{S})_Q = \frac{\sum_{Q=1} F(m_i,T)\cosh[\frac{\vec{q}*\vec{\mu}_q}{T}] + 2^4 \sum_{Q=2} F(m_i,T)\cosh[(\frac{\vec{q}*\vec{\mu}_q}{T}]}{\sum_{Q=1} F(m_i,T)\sinh[\frac{\vec{q}*\vec{\mu}_q}{T}] + 2^3 \sum_{Q=2} F(m_i,T)\sinh[\frac{\vec{q}*\vec{\mu}_q}{T}]} \quad (3.64)$$

$$(\frac{\sigma^2}{M})_Q = \frac{\sum_{Q=1} F(m_i,T)\cosh[\frac{\vec{q}*\vec{\mu}_q}{T}] + 2^2 \sum_{Q=2} F(m_i,T)\cosh[(\frac{\vec{q}*\vec{\mu}_q}{T}]}{\sum_{Q=1} F(m_i,T)\sinh[\frac{\vec{q}*\vec{\mu}_q}{T}] + 2 \sum_{Q=2} F(m_i,T)\sinh[\frac{\vec{q}*\vec{\mu}_q}{T}]} \quad (3.65)$$

Fig. 3.6 shows the susceptibility ratios of the strangeness and charge number as a function of energy along the freeze-out curve. Multi-charged ($Q \geq 2$) and multi-strange ($S \geq 2$) particles get a larger weight in higher moments resulting in a significant deviation of the $(\kappa\sigma^2)_Q$ and $(\kappa\sigma^2)_S$ from unity. The $(S\sigma)_Q$ and $(S\sigma)_S$ are not simply related to the $\tanh(\mu_Q/T)$ and $\tanh(\mu_S/T)$ like the baryon number fluctuations.

At low temperatures, hadrons are the relevant degrees of freedom and the HRG model has been shown to be a good description of thermal conditions
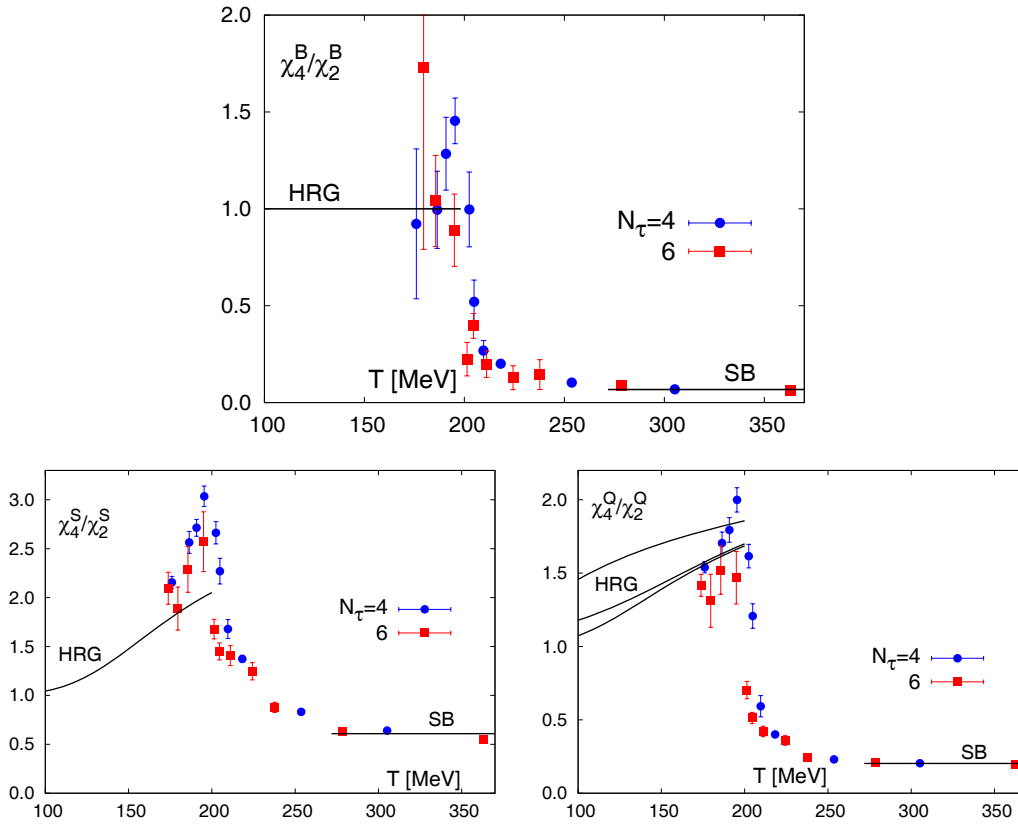
Figure 3.7: The ratio of fourth and second order cumulants of baryon number (top), strangeness (bottom left) and electric charge (bottom right) fluctuations. In the latter case the curves are for a HRG model calculated with physical pion masses (upper curve), pions of mass 220 MeV (middle) and infinitely heavy pions (lower curve). The figures are taken from [57].

at chemical-freeze out [57, 92, 93, 94]. On the other hand, the fluctuations of the thermal system have been successfully described by HRG model and in good agreement with Lattice QCD calculations below the transition temperature. The HRG calculations break down in the vicinity of the transition temperature. In Fig. 3.7, we compare the forth order to second order susceptibility ratios for baryon, strangeness and charge number as a function of temperature from Lattice QCD computed at $\mu_B = 0$ with HRG model calculations. Those ratios are expected to be less sensitive to the detail of the hadron mass spectrum and emphasize the charges of relevant degrees of freedom contributing to the fluctuations. Based on equ. (3.54) from HRG model calculation, the χ_B^4/χ_B^2

is equal to unity and independent of the hadron mass spectrum. This can be reproduced by lattice QCD results and the results are shown in Fig. 3.7 (top). From equ. (3.59) and equ. (3.63), we know that it is more complicated in the strange and charge sectors, in which multiply strange hadrons and charged hadrons $(Q, S \geq 2)$ contribute to the HRG model calculations. This will lead to deviations of the cumulant ratio χ_S^4/χ_S^2 and χ_Q^4/χ_Q^2 from unity.

The formulas (equ.(3.53) to (3.65)) provide connections between fluctuation observables and thermodynamic quantities for a thermal equilibrium system. As there has no QCD critical point physics in the HRG model, it also provides pure thermal equilibrium fluctuations baseline to search for the QCD critical point using higher moments of net-baryon, net-strangeness and net-charge fluctuations. Deviations from the HRG predication may indicate non-equilibrium of the system and/or new physics. The mutual agreements between Lattice QCD, HRG Model and experimental data can provide us evidence of thermalization of the colliding system.

3.2.2 QCD Based Model Calculation: Sensitivity to the Correlation Length

Theoretical calculations demonstrate that due to the finite size effect, rapid expansion and critical slowing down etc., the typical correlation length in heavy ion collisions near the QCD Critical Point (CP) is about $1.5 \sim 3 fm$ [60], which is a small finite value. The event-by-event observables are believed to be sensitive to the correlations and fluctuations. In fact, many event-by-event experimental observables have been applied to search for the CP and phase transitions, such as average p_T fluctuation [95], K/π ratio fluctuation [96] etc.. Unfortunately, no evidence of CP signatures have been discovered yet. It motivates us to find more sensitive experimental observables. Generally, the variance ($\sigma^2 =< (\delta N)^2 >$) of distributions of conserved quantities, such as net-baryon, net-charge and net-

strangeness are related to ξ as $\sigma^2 \sim \xi^2$, where $\delta N = N - M$, N is the particle multiplicity in one event and M is the averaged particle multiplicity of the event sample.

Recently, QCD based model calculations show that higher moments of particle multiplicity distributions are proportional to the higher power of the correlation length [61, 62], such as third order cumulant $< (\delta N)^3 > \sim \xi^{4.5}$ and fourth order cumulant $< (\delta N)^4 > -3 < (\delta N)^2 >^2 \sim \xi^7$). Due to the higher sensitivity to the CP related correlation and fluctuations than variance, higher moments (skewness ($S =< (\delta N)^3 > /\sigma^3$) and kurtosis ($\kappa =< (\delta N)^4 > /\sigma^4 - 3$)) of multiplicity distributions are chosen to search for the CP [56].

In statistics, skewness and kurtosis are widely used to characterize the properties of probability distributions. Skewness is used to describe the asymmetry property of distributions, while kurtosis describes their peakness. Sign changing of skewness as a function of colliding energy may indicate a crossing of phase boundary [27]. In addition, for normal distributions, both of the skewness and kurtosis are equal to zero, thus they are ideal probe of non-Gaussian fluctuations.

3.3 Baseline Study

It is important for us to understand the baseline and background effects before we search for new physics. To search for the QCD critical point, two important baseline effects for the higher moments analysis are the non-QCP physics and the detector efficiency. In the following sub-sections, we will discuss about the two baseline effects.

3.3.1 Detector Efficiency Effect

Experimentally, particles are measured with a certain detection efficiency which is mainly due to the reconstruction efficiency, detector acceptance and intrinsic response efficiency. The total efficiency shows transverse momentum, centrality and particle species dependence. On the other hand, it is hard to correct the efficiency for event-by-event measurements, such as proton and antiproton number in our case. That's why we should know the efficiency effects to build up baseline for our higher moments analysis.

In principle, the particle detection can be seen as a binomial process. If the detector efficiency is ε and the total input single particle multiplicities is N, then, the detected number of particles k is distributed according to a binomial distribution:

$$B(k; N, \varepsilon) = \frac{N!}{k!(N-k)!}\varepsilon^k(1-\varepsilon)^{N-k} \tag{3.66}$$

Here we consider the net-proton number $(N_{p-\bar{p}} = N_p - N_{\bar{p}})$ distributions. If the intrinsic distributions of the number of protons and anti-protons are $P(N_p)$ and $P(N_{\bar{p}})$, respectively, we can get the finally detected net-proton distributions $T(k)$ as

$$\begin{aligned} T(k) &= \sum_{N_p, N_{\bar{p}}, n,} B(n+k; N_p, \varepsilon_p)B(n; N_{\bar{p}}, \varepsilon_{\bar{p}})P(N_p)P(N_{\bar{p}}) \\ (n &+ k > 0, n > 0) \end{aligned} \tag{3.67}$$

, where the ε_p and $\varepsilon_{\bar{p}}$ are the proton and antiproton detection efficiency, respectively. For simplification, we assume that the detection efficiency of protons and anti-protons is equal, $\varepsilon_p = \varepsilon_{\bar{p}} = \varepsilon$, which is a reasonable approximation in our analysis. Consequently, we can build up the relation between the various cumu-

lants of detected net-proton distribution and intrinsic net-proton distributions.

$$C_{1,k} = \varepsilon < N_p - N_{\bar{p}} > \tag{3.68}$$

$$C_{2,k} = \varepsilon^2 C_{2,N} + \varepsilon(1-\varepsilon) < N_p + N_{\bar{p}} > \tag{3.69}$$

$$C_{3,k} = \varepsilon^3 C_{3,N} + 3\varepsilon^2(1-\varepsilon)(C_{2,N_p} - C_{2,N_{\bar{p}}})$$
$$+ (1-2\varepsilon)(1-\varepsilon)\varepsilon < N_p - N_{\bar{p}} > \tag{3.70}$$

$$C_{4,k} = \varepsilon^4 C_{4,N} + 6\varepsilon^3(1-\varepsilon)(C_{3,N_p} + C_{3,N_{\bar{p}}})$$
$$+ 4\varepsilon^2(1-2\varepsilon)(1-\varepsilon)C_{2,N} + 3\varepsilon^2(1-\varepsilon)^2 C_{2,N_p+N_{\bar{p}}}$$
$$+ [1-6\varepsilon(1-\varepsilon)]\varepsilon(1-\varepsilon) < (N_p + N_{\bar{p}}) > \tag{3.71}$$

We may find that the efficiency effects are complicated for higher moments and it is hard to estimate the effect. But we can consider a special case that the primary proton and antiproton are distributed as independent poisson distributions, which have been widely seen in the particle and nuclear physics for particle distributions. Then, the equ.(35)-(38) can be simplified as:

$$C_{1,k} = C_{3,k} = \varepsilon < N_p - N_{\bar{p}} > \tag{3.72}$$

$$C_{2,k} = C_{4,k} = \varepsilon < N_p + N_{\bar{p}} > \tag{3.73}$$

and we have:

$$M_k = C_{1,k} = \varepsilon M_N \tag{3.74}$$

$$\sigma_k^2 = C_{2,k} = \varepsilon \sigma_N^2 \tag{3.75}$$

$$S_k = \frac{C_{3,k}}{(C_{2,k})^{3/2}} = \frac{S_N}{\sqrt{\varepsilon}} \tag{3.76}$$

$$\kappa_k = \frac{C_{4,k}}{(C_{2,k})^2} = \frac{\kappa_N}{\varepsilon} \tag{3.77}$$

The moment products $S\sigma$ and $\kappa\sigma^2$ can be written as:

$$S_k\sigma_k = \frac{S_N}{\sqrt{\varepsilon}} \times \sqrt{\varepsilon}\sigma_N = S_N\sigma_N \tag{3.78}$$

$$\kappa_k\sigma_k^2 = \frac{\kappa_N}{\varepsilon} \times \varepsilon\sigma_N^2 = \kappa_N\sigma_N^2 \tag{3.79}$$

It can be seen that for independent poissonian distributed proton and antiproton multiplicities, the efficiency effect on the various moments are simple and shown by equ. (41)-(44). It is also important for us that the efficiency effects cancel in the moment products $S\sigma$ and $\kappa\sigma^2$ as shown in equ. (45)-(46), which means the two moment products of poissonian distributed quantities are not distorted by the efficiency.

As it is difficult to estimate the efficiency effects for arbitrary input distribution, we have studied the effects of the detector efficiency by comparing the various moments of net-proton distribution generated from the HIJING hadronic transport model and the moments of the reconstructed net-proton distributions after passing the same event through a realistic GEANT detector simulation . The difference between the two cases for the σ, S and κ are about an order of magnitude smaller than their absolute values. Typical difference values for central Au+Au 200 GeV collisions are -0.37$\pm$0.05, 0.02$\pm$0.05 and -0.06$\pm$0.12 for σ, S and κ, respectively. These results indicate that the effects on the shape of the distributions are small [56].

3.3.2 Expectations from Poisson Statistics

Many background effects result in statistical fluctuations, which obey the Poission statistics. If we assume our true signals are not correlated with those statistical backgrounds, then the Poisson value of our observables can serve as a baseline. In statistics, the probability distribution of Poisson can be expressed

as :

$$P(X = k) = \frac{e^{-\lambda}\lambda^k}{k!} \tag{3.80}$$

, where the k is the random variable and λ is the parameter of the Poisson distribution. The various moments (M, σ, S, κ) as well as moment products $(\kappa\sigma^2, S\sigma)$ of single Poisson distribution are simple :

$$M = \lambda \tag{3.81}$$

$$\sigma = \sqrt{\lambda} \tag{3.82}$$

$$S = \frac{1}{\sqrt{\lambda}} \tag{3.83}$$

$$\kappa = \frac{1}{\lambda} \tag{3.84}$$

$$\kappa\sigma^2 = S\sigma = 1 \tag{3.85}$$

Hence, for particle multiplicities, its Poisson value of its various moments are simple. In our case, we are dealing with the difference of two independent Poisson distributions, such as net-proton, net-charge. The difference of two independent Poisson distributions distributed as the so called "Skellam" distributions. Its probability density formula is :

$$f(k; \mu_1, \mu_2) = e^{-(\mu_1+\mu_2)}(\frac{\mu_1}{\mu_2})^{k/2}I_{|k|}(2\sqrt{\mu_1\mu_2}) \tag{3.86}$$

, where the μ_1 and μ_2 are the mean value of two Poisson distributions, respectively, the $I_k(z)$ is the modified bessel function of the first kind. Then, we can calculate various moments (M, σ, S, κ) and moment products $(\kappa\sigma^2, S\sigma)$ products

of the Skellam distribution. The results are shown below:

$$M \;=\; \mu_1 - \mu_2 \tag{3.87}$$

$$\sigma \;=\; \sqrt{\mu_1 + \mu_2} \tag{3.88}$$

$$S \;=\; \frac{\mu_1 - \mu_2}{(\mu_1 + \mu_2)^{3/2}} \tag{3.89}$$

$$\kappa \;=\; \frac{1}{\mu_1 + \mu_2} \tag{3.90}$$

$$S\sigma \;=\; \frac{\mu_1 - \mu_2}{\mu_1 + \mu_2} \tag{3.91}$$

$$\kappa\sigma^2 \;=\; 1 \tag{3.92}$$

We may find that the $\kappa\sigma^2$ are always unity for both Poisson and Skellam distributions while the $S\sigma$ is changed from unity in Poisson to the quantity to describe the asymmetry between μ_1 and μ_2 in Skellam distribution. In our case, if we say the net-proton obeys the Poisson statistics, then the protons and anti-protons should be distributed as independent Poisson distributions and the net-proton obeys the Skellam distribution. In grand canonical ensemble calculation of the thermal model, such as the HRG model we used, the resulted particle multiplicity is an independent Poisson distribution, thus our results are consistent with Poisson statistics or with an thermal model.

3.3.3   Model Calculations

To investigate the non-CP physics background contribution to our various moments and moments products, such as resonance decay, jet-production, co-alescence mechanism of particle production, thermal particle production and hadronic rescattering, we have calculated moment products $S\sigma$ and $\kappa\sigma^2$ by using various models, such as UrQMD [97] (ver.2.3), AMPT default (ver.1.11), AMPT String Melting [98] ($\sigma_{pp} = 10mb$) (ver.2.11), Therminator [99] (ver.1.0) and HIJING [100] (ver.1.35). All models were running under default versions
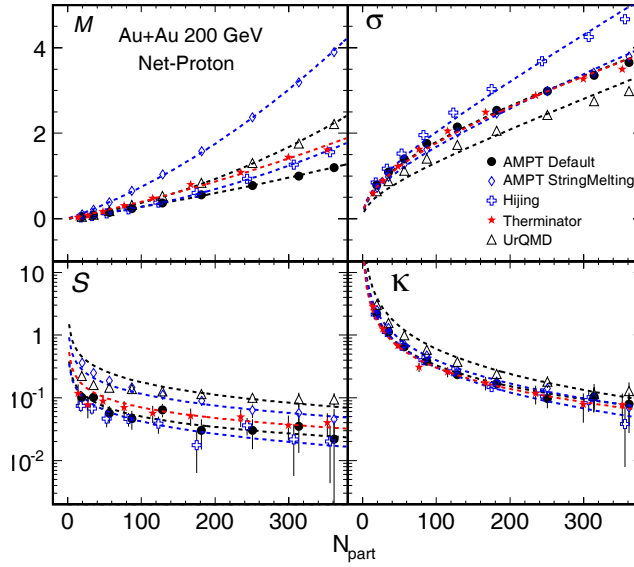
Figure 3.8: Centrality dependence of various moments of net-proton distributions for Au+Au collisions at $\sqrt{s_{NN}} = 200$ GeV from various models.
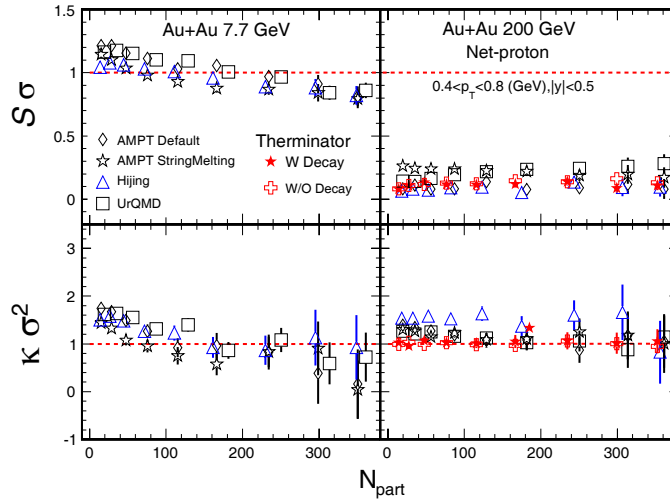
Figure 3.9: Centrality dependence of $S\sigma$ and $\kappa\sigma^2$ of net-proton distributions for Au+Au collisions at $\sqrt{s_{NN}} = 7.7, 200$ GeV from various models.

and using the same kinematic coverage as for data.

Fig. 3.8 shows the centrality dependence of various moments of net-proton distributions for Au+Au 200 GeV from model calculations. The mean value and standard deviation increase monotonically with increasing centrality, while the skewness and kurtosis decrease monotonically. The dashed lines shown in the figure are the Central Limit Theorem (CLT) expectations by assuming a superposition of independent sources. The details of CLT expectations will be discussed in the next chapter.
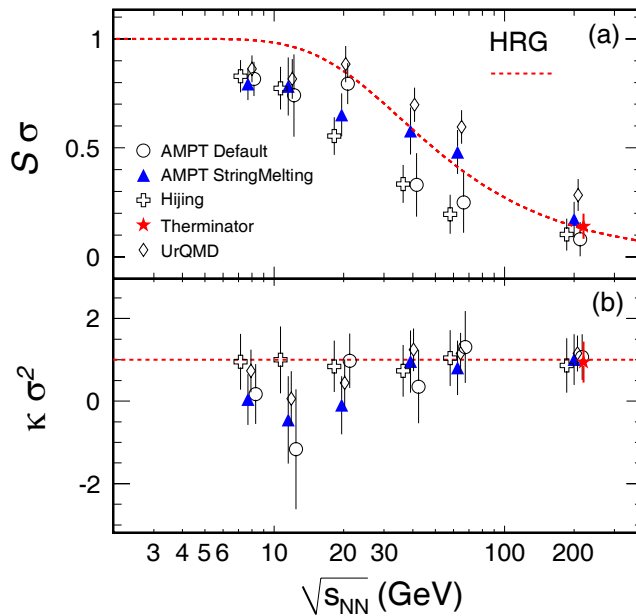
Figure 3.10: Energy dependence of $S\sigma$ and $\kappa\sigma^2$ of net-proton distributions for various models. The red dash lines are predictions from HRG model.

Fig. 3.9 shows $S\sigma$ and $\kappa\sigma^2$ of net-proton distributions for Au+Au collisions at $\sqrt{s_{NN}} = 7.7$ GeV (left two panels) and at $\sqrt{s_{NN}} = 200$ GeV (right two panels) with various model calculations as a function of N_{part}, the number of participants. For Au+Au 7.7 GeV, the $S\sigma$ of net-proton distributions shows a small decreasing trend, while the $\kappa\sigma^2$ are almost no centrality dependence and around unity. For Au+Au 200 GeV, the $S\sigma$ and $\kappa\sigma^2$ show no centrality dependence.

In Fig. 3.10, we show the energy dependence for $S\sigma$ and $\kappa\sigma^2$ of most central $(0-5\%)$ net-proton distributions from various model calculations. The $S\sigma$ and $\kappa\sigma^2$ calculated from Hijing, AMPT default and UrQMD transport model fail to be described by HRG model simultaneously. The results from AMPT String Melting and Therminator can be described by HRG model at the high energy. A non-monotonic variation as a function of collision energy for $S\sigma$ and $\kappa\sigma^2$ would indicate new physics, such as critical fluctuations.

CHAPTER 4

Analysis Method

In this chapter, we introduce you the methods to perform the higher moments analysis of the experimental data. First, we will discuss the centrality determination as well as the particle identification with TPC and TOF detector in the STAR experiment. Then, the so called Centrality Bin Width Effect (CBWE) in the higher moment analysis is studied and also several methods are developed to eliminate this effect. Finally, we deduce the formula for number of participant (N_{part}) dependence of the higher moments derived from Central Limit Theorem (CLT), in which we assume the colliding system consist of many identical independent emission sources. This can provide us the baseline to understand the centrality dependence of the various higher order moments.

4.1 Data Sets

The data presented in this section were measured by the STAR detector at Brookhaven National Laboratory (BNL). Those are Au+Au collisions at $\sqrt{s_{NN}} = 7.7, 11.5, 19.6, 39, 62.4,$
130 and 200 GeV, Cu+Cu collisions at $\sqrt{s_{NN}} = 22.4, 62.4, 200$ GeV, d+Au at $\sqrt{s_{NN}} = 200$ GeV and p+p collisions at $\sqrt{s_{NN}} = 62.4, 200$ GeV. Basic information for data sets used in the analysis, such as colliding system and energy, production name, the calendar time in physics, the run and year for data taking, are shown in the table 4.1.

Table 4.1: Cu+Cu, d+Au and p+p data sets information

System	Energy (GeV)	Weeks for Physics	Run	Year	Production
p+p	62.4	2	Run 6	2006	P06ie
	200	10	Run 9	2009	P10ic
d+Au	200	10	Run 3	2003	P04if
	22.4	5 Shifts	Run 5	2005	P05if
Cu+Cu	62.4	2	Run 5	2005	P05id
	200	8	Run 5	2005	P06ib
	7.7	5	Run 10	2010	P10ih
	11.5	1.5	Run 10	2010	P10ih
	19.6	2 Shifts	Run 2	2001	P02ge
Au+Au	39	2	Run 10	2010	P10ih
	62.4	9 days	Run 4	2004	P04id‖P04ie
	130	5	Run 1	2000	P00hi
	200	12	Run 4	2004	P05ic
	200	11	Run 10	2010	P10ij‖P10ik

4.1.1 Event Selection

In our analysis, we select minimum bias trigger events with a z-coordinate (V_z) of primary vertex within ±30cm for most of the colliding systems, from the center of the TPC along the beam line. This ensures uniformity of detector efficiency and ideal detector coverage. To obtain enough statistics for Au+Au collision at 7.7, 11.5 GeV and 130 GeV, we use loose primary vertex cut $|V_z| \leq 70$cm to select minimum bias trigger events for those three energies. It is known that the inefficiency effect for primary vertex z-coordinate within ±70cm is small for those three energies. To remove background events, such as beam-beam pipe events, transverse x-y coordinate (V_x, V_y) cuts are also applied for some of the colliding systems, especially for the low energy collision, such as Au+Au collision at 7.7 and 11.5, 19.6, 39 GeV. The detail of the minimum bias trigger setup name and trigger id selection of the data set are listed in the table 4.2.

The parameters for the vertex cuts and the number of events for the Au+Au, Cu+Cu, d+Au and p+p collisions are listed in table 4.3.

Table 4.2: Au+Au, Cu+Cu, d+Au and p+p data trigger selection

System	Energy (GeV)	TriggerSetupName	TriggerId
p+p	62.4	ppProduction62||ppProductionMB62	147001
	200	pp2pp_Production2009	7||250107
d+Au	200	dAuMinBias	2001||2003
Cu+Cu	22.4	cu22ProductionMinBias	86011
	62.4	cu62ProductionMinBias	76007||76001
	200	cuProductionMinBias	66007
Au+Au	7.7	AuAu7_production	290001||290004
	11.5	AuAu11_production	310014
	19.6	minbiasZDC	4608||4609
	39	AuAu39_production	280001
	62.4	Production62GeV	35001||35004 ||35007||35009
	130	minbias	1||3
	200	ProductionMinBias	15007
	200	AuAu200_production	260001||260011 ||260021||260031

Table 4.3: Vertex cuts and number of events used in the analysis for Au+Au, Cu+Cu, d+Au and p+p collisions. $\vec{V_r} = (V_x, V_y)$ and $\vec{V_0} = (-0.246, 0.378)$

System	Energy (GeV)	V_z Cut (cm)	V_r Cut (cm)	Events (M)
p+p	62.4	$|V_z| < 30$	N/A	1.3
	200	$|V_z| < 30$	N/A	6.7
d+Au	200	$|V_z| < 30$	N/A	2.3
Cu+Cu	22.4	$|V_z| < 30$	$|\vec{V_r}| < 1$	0.67
	62.4	$|V_z| < 30$	N/A	14.7
	200	$|V_z| < 30$	N/A	3.7
Au+Au	7.7	$|V_z| < 70$	$|\vec{V_r}| < 2$	5
	11.5	$|V_z| < 70$	$|\vec{V_r}| < 2$	16.4
	19.6	$|V_z| < 30$	$|\vec{V_r} - \vec{V_0}| < 2$	0.043
	39	$|V_z| < 30$	$|\vec{V_r}| < 2$	10
	62.4	$|V_z| < 30$	N/A	5.5
	130	$|V_z| < 70$	N/A	0.36
	200	$|V_z| < 30$	N/A	9
	200	$|V_z| < 30$&& $|V_z - VpdV_z| < 3$	N/A	21

4.1.2 BES Data Taking at STAR in the Year 2010

One of the main goals of the RHIC Beam Energy Scan (BES) program is to search for the QCD critical point and the phase boundary in the QCD phase diagram [19]. This will allow us to understand the phase structure of hot, dense matter created in the high energy heavy ion collisions. In the year 2010 (Run 10), RHIC has tuned the colliding energy from $\sqrt{s_{\rm NN}}$=200 GeV down to $\sqrt{s_{\rm NN}}$=7.7 GeV and the corresponding μ_B coverage is about $20 - 410$ MeV. The actual time of data taking for the BES data is shown in the table 4.1. Table 4.4 shows the number of minimum bias and/or central events collected in Run 10 for each energy. For 7.7 GeV, the cuts $|V_z| < 70$cm and $|\vec{V_r}| < 2$cm are marked as so called "good events".

Table 4.4: Run 10 Au+Au BES data taken in year 2010.

System	$\sqrt{s_{NN}}$(GeV)	Minbias (M)	Central (M)	Start and End Date
	200	355	265	Dec. 28 to Mar. 18
	62.4	140	33	Mar. 18 to Apr. 08
Au+Au	39	250	N/A	Apr. 08 to Apr. 22
	11.5	20	N/A	Apr. 22 to May 27
	7.7	5	N/A	May 27 to Jun 07

Data taking for Au+Au collision at 39, 62.4 and 200 GeV in Run 10 went fairly smooth and we have taken more events than we expected, which was not the case for Au+Au 7.7 GeV collisions. In the early days of 7.7 GeV data taking, we got very few good events at rate of $1Hz$ and lots of background events, such as beam-beam pipe events and beam-support structure events. We have never before met such a situation, where we had to work very hard for very few events. As shown in Fig. 4.1 and 4.2, we can see the good event rate and percentage of the good events for Au+Au 7.7 GeV data taken as a function of beam fill number monitored by the STAR High Level Trigger (HLT). The good event rate increased from $1Hz$ to $6Hz$ and the percentage of good events increased from 5%
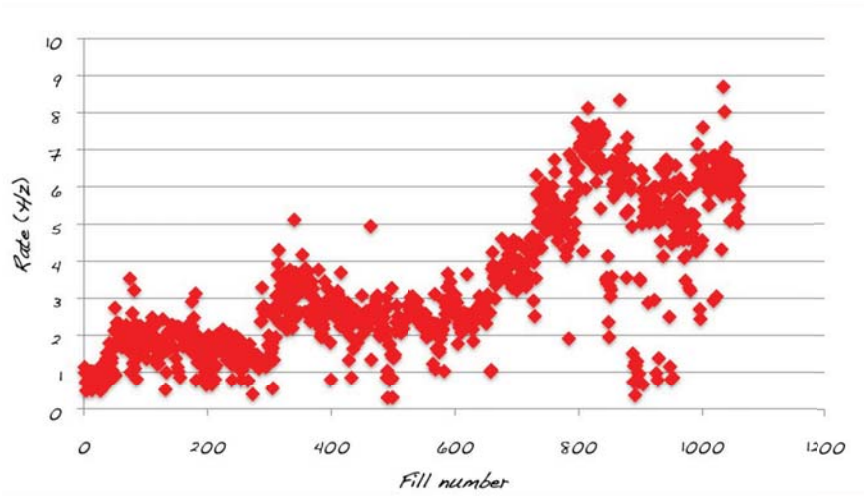
Figure 4.1: Good event rate for Au+Au 7.7 GeV data taken as a function of beam fill number monitoring by STAR High Level Trigger (HLT).
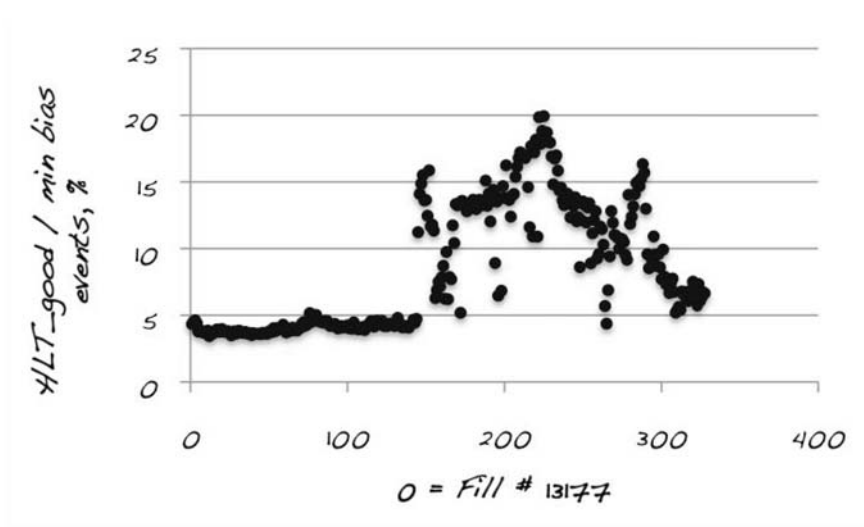
Figure 4.2: Percentage of good event for Au+Au 7.7 data taken as a function of beam fill number monitoring by STAR High Level Trigger (HLT).
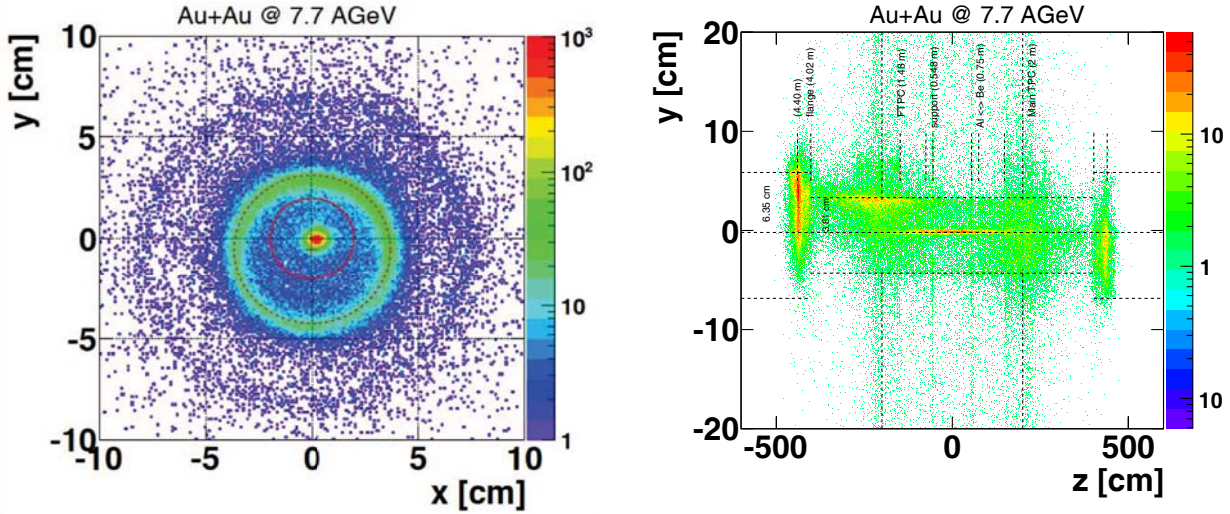
Figure 4.3: The Vertex X-Y and Y-Z 2D distribution for Au+Au collision at 7.7 GeV calculated from new vertex finder. The figures are taken from [101].

(from fill number 13177) to 17%. Fig. 4.3 shows the $X-Y$ and $Y-Z$ coordinate 2D plots of the primary vertex reconstructed with a new vertex finder algorithm for the Au+Au 7.7 GeV data. In the $X-Y$ plot of Fig. 4.3, the red solid circle represents a circle with radius 2 cm and the events outside of the solid circle are mainly from by background events. Those background events as shown in $Y-Z$ plot of Fig. 4.3 result from the interaction between beam and materials distributed along z-direction, such as flange ($\sim$ 4m far from TPC center), FTPC, TPC support structure and beam pipe.

We had to completely change our running conditions, such as TPC always on, run starting with injection of second beam, changing beam focus length β^* from 10 m to 6 m, 10 minutes fill and 4 fill per hour, to reduce the background events and increase the good event rate. Finally, we got a percentage of 17% good events compared with the 2% of the initial data taking for 7.7 GeV. In the top plot of Fig. 4.4, we show the day to day dependence of the number of good events with the run condition for the corresponding periods. The bottom two plots of Fig. 4.4 show the total number of events (left plot) and the percentage
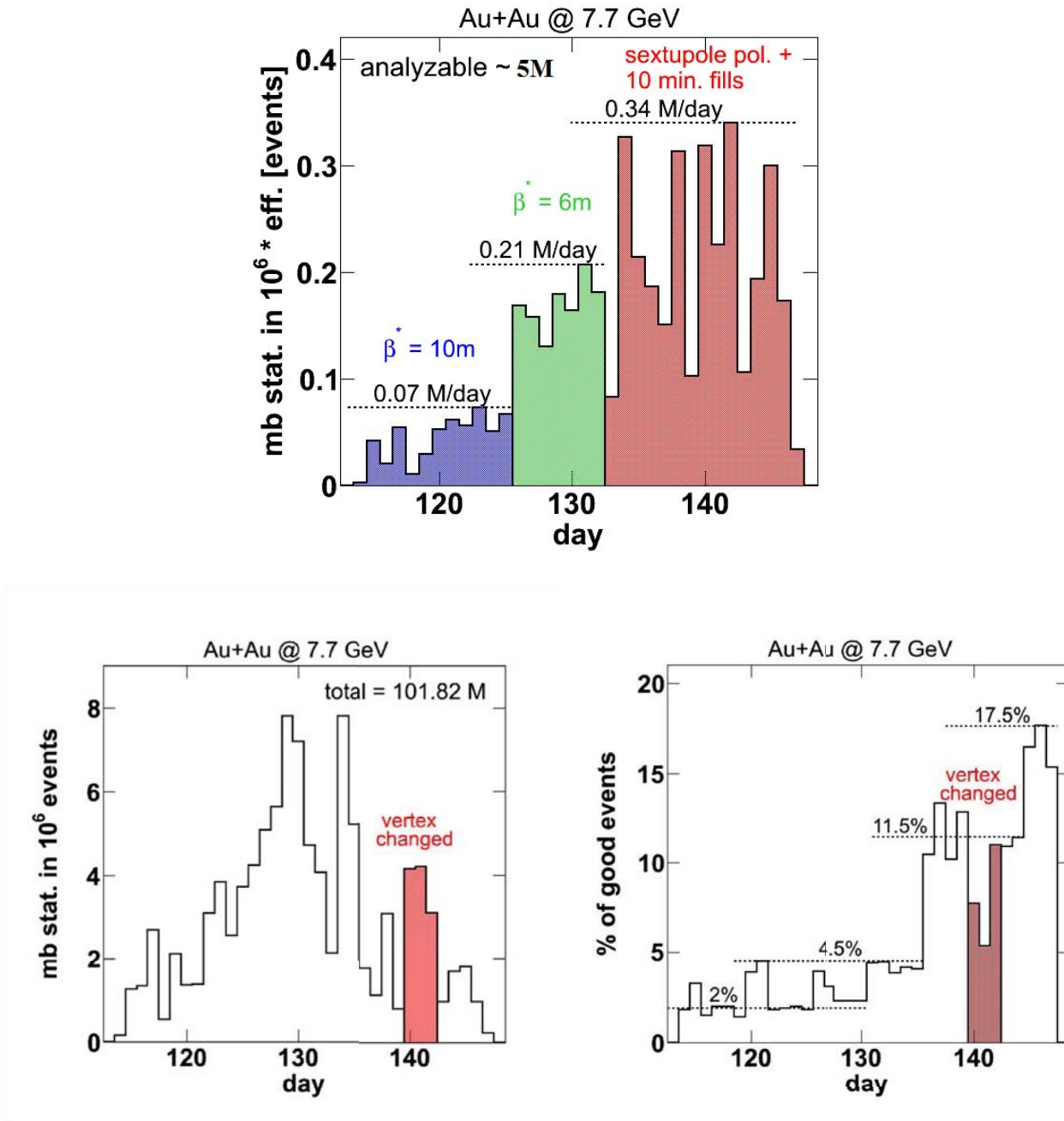
Figure 4.4: Day by day good events (top plot), total events (bottom left) and percentage of good events (bottom right) evolution for Au+Au 7.7 GeV. The figures are taken from [101]
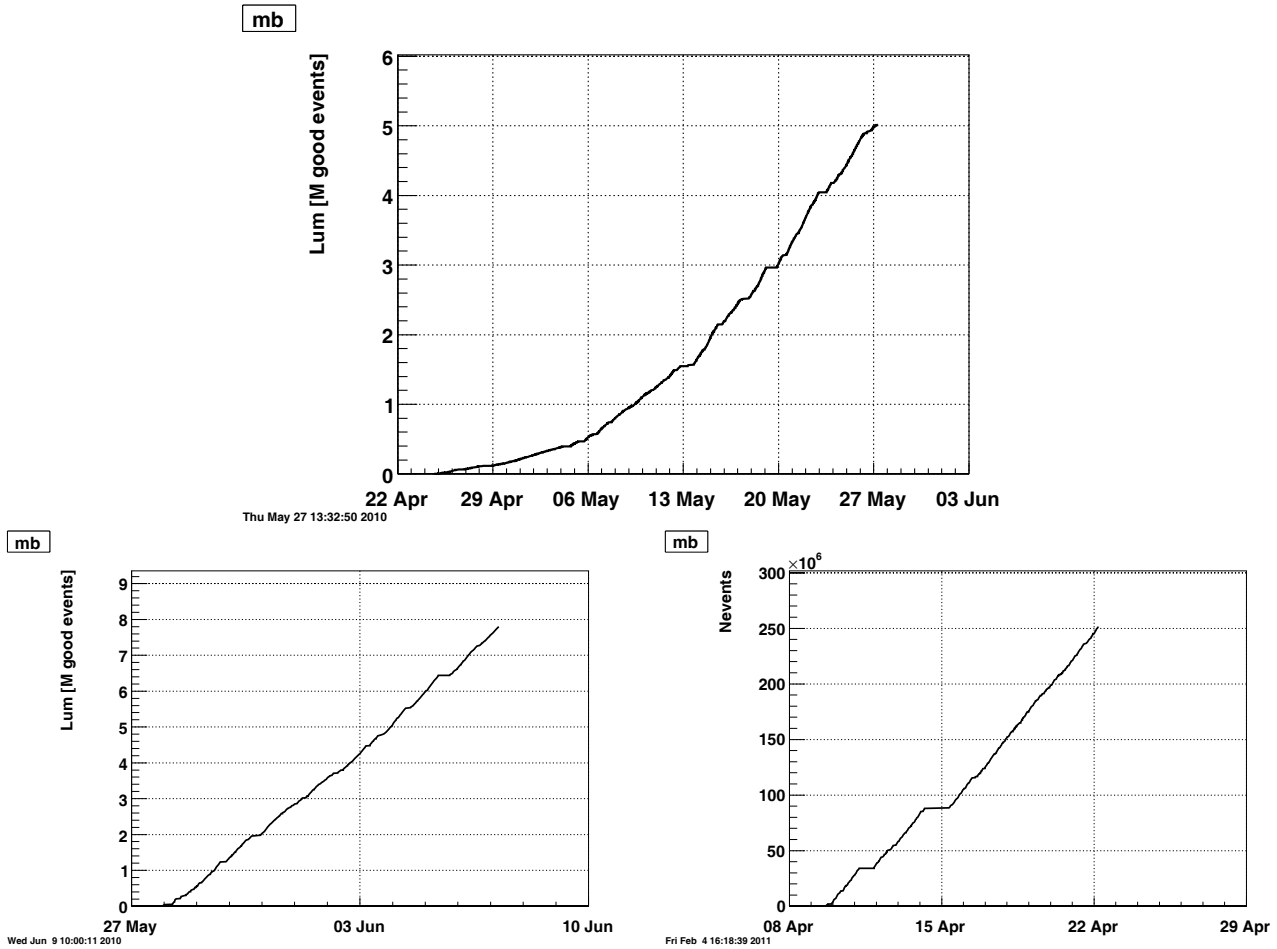
Figure 4.5: Integrated of good events evolution for Au+Au collision at 7.7 GeV (top), 11.5 GeV (bottom left) and integrated total number of events for Au+Au collision at 39 GeV monitored by HLT.

of good events (right plot) for 7.7 GeV. The shadow region in the bottom two plots are corresponds to a period that with a different collision vertex position.

In top of Fig. 4.5 shows day by day dependence of the integrated number of good events collected for 7.7 GeV ($|V_z| < 70$cm, $|\overrightarrow{V_r}| < 2$cm) while the bottom two plots show the good events ($|V_z| < 30$cm, $|\overrightarrow{V_r}| < 2$cm) and total events for 11.5 (left plot) and 39 GeV (right plot), respectively. We notice that at early days of 7.7 GeV, the number of good events is pretty small and increased in the end after great efforts.
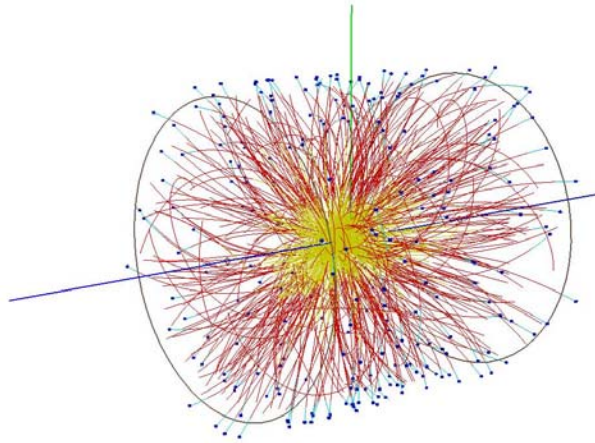
Figure 4.6: Event display for Au+Au collision at 7.7 GeV. The tracks with blue end points are those matched to the TOF.

Although, we met many problems during Run 10 data taking, such as dead TPC sectors, low event rate and high background at low energy, we still met or exceeded our goals for each energy point at the end of the run after great efforts from all of us. I am very glad to say that the Run 10 is a very successful run. Finally, in Fig. 4.6, We show a beautiful event display of Au+Au collisions at 7.7 GeV as the end of this section.

4.2 Centrality Determination

The centrality of nucleus-nucleus collisions is an important parameter in heavy ion collision physics. It can be defined by several different parameters [102]. The most common one is the so called impact parameter b, defined as the distance between the geometrical centers of the colliding nuclei in the plane transverse to their direction. Other geometry variables include the number of nucleons that participate, N_{part} and the number of binary collisions, N_{coll}. The number of participants is defined as the number of nucleons, which undergo at least one inelastic nucleon-nucleon collision and the number of binary collisions is defined as number of inelastic nucleon-nucleon collisions. With the above geometric information, we can compare centrality dependence (N_{part}, N_{coll}) of observables between different experiments. Unfortunately, those geometry observables can't be directly measured and must be deduced from a combination of experimentally measured quantities and Monte-Carlo simulations. This usually is done by a purely geometric model, the so called Glauber model [103, 104].
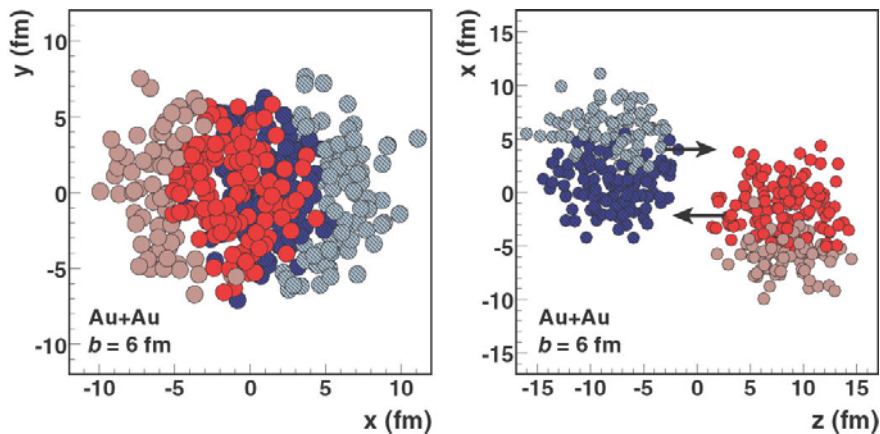
Figure 4.7: Illustration of a Glauber Monte Carlo event for Au+Au at $\sqrt{s_{NN}} = 200$ GeV with impact parameter $b = 6$ fm in the transverse plane (left panel) and along the beam axis (right panel). The nucleons are drawn with a radius $\sqrt{\sigma_{inel}^{NN}/\pi}/2$. Darker disks represent participating nucleons. The figures are taken from [104].
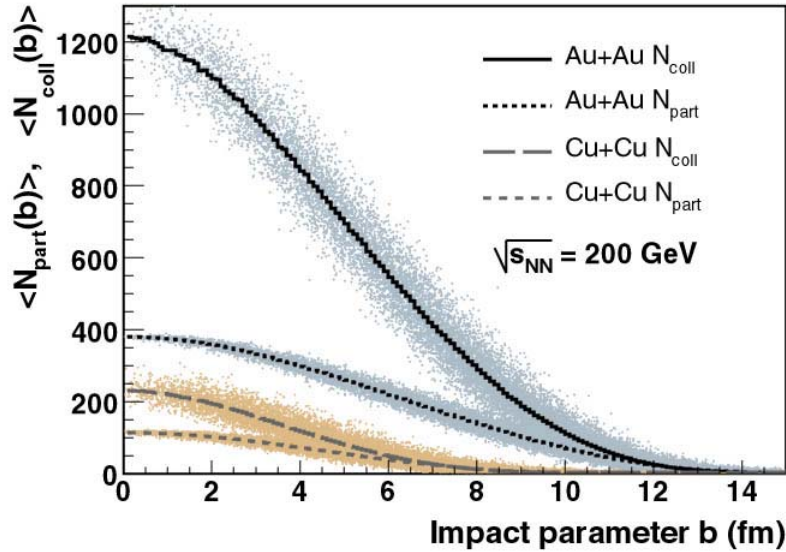
Figure 4.8: Average number of participants ($\langle N_{\mathrm{part}} \rangle$) and binary nucleon-nucleon collisions ($\langle N_{\mathrm{coll}} \rangle$) along with event-by-event fluctuation of these quantities in the Glauber Monte Carlo calculation as a function of the impact parameter b. The figures are taken from [104].

In the Glauber model, a nucleus-nucleus collision is treated as a sequences of independent binary nucleon-nucleon collisions. Fig. 4.7 shows an illustration of a Glauber Monte Carlo event for a single Au+Au collision with impact parameter $b = 6$ fm. The average number of participants $< N_{part} >$ and binary collisions as a function of impact parameter b are shown in the Fig. 4.8 for Au+Au and Cu+Cu collision at $\sqrt{s_{\mathrm{NN}}} = 200$ GeV. For a fixed impact parameter, the fluctuations of the N_{part} and N_{coll} are also shown in the Fig. 4.8.

Experimental observables, such as particle multiplicity, not only reflect the geometry of the collision, but also depend on physics processes. This indicates that relation between measured observable and impact parameter is not one-to-one correspond. There are fluctuations for the observable even with a fixed impact parameter. One value of observable may correspond to many possible impact parameters. Experimentally, the centrality is usually expressed as a percentage of

the total cross-section, such as $0-5\%$ (most central), $30-50\%$ (semi-peripheral), which indicates the fraction of a data sample (corrected for inefficiency) relative to all possible collision geometries (impact parameters).
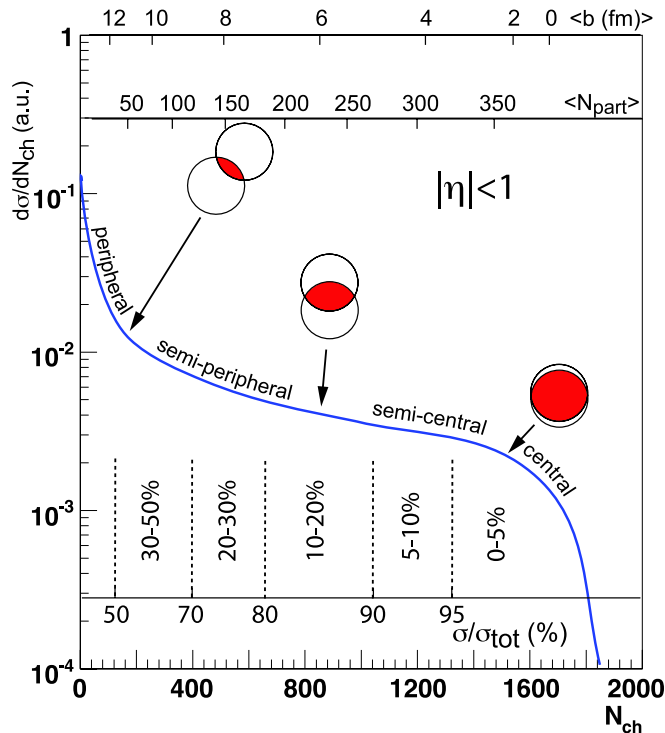
Figure 4.9: An illustrated example of the correlation of the total inclusive charged-particle multiplicity N_{ch} with Glauber-calculated quantities(b, N_{part}). The plotted distribution and various values are illustrative and not actual measurements. The figure is taken from [104].

For illustrative purposes, Fig. 4.9 shows a typical centrality determination plot with charged particle multiplicity. Once the total integral of the distribution is known, centrality classes are defined by binning the distribution on the basis of the fraction of the total integral, which is represented by the dashed lines shown in Fig. 4.9. In an analogous way, we can calculate the charged particle multiplicity and determine the centrality classes with Glauber model simulations, in which the average geometrical parameters (N_{part} and N_{coll}) for each centrality bin can be also calculated.

In the STAR experiment, the efficiency-uncorrected charged particle multi-
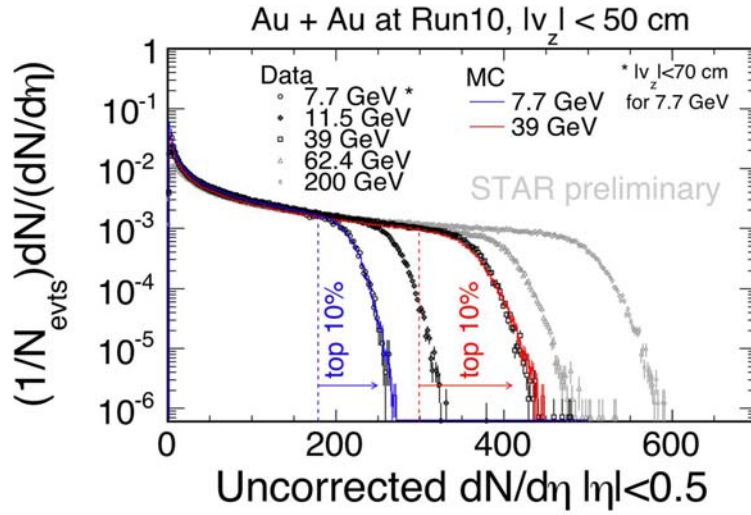
Figure 4.10: Comparison of refmult from 7.7 to 200 GeV at Run10. Note: $|V_z| < 70$ cm for 7.7 GeV. The blue and red are refmult distributions from Monte-Carlo simulation for 7.7 and 39 GeV, respectively.

plicity ($dN_{ch}/d\eta$), which is also called reference multiplicity (refmult) measured by the Time Projection Champer (TPC) at mid-rapidity ($|\eta| < 0.5$) combined with Glauber model simulations is used for centrality determination. Fig. 4.10 shows the comparison of refmult from 7.7 GeV to 200 GeV from Run 10. The blue and red curves in Fig. 4.10 are calculated from Monte-Carlo simulations by convoluting the negative binomial distribution with charged particle multiplicity obtained by using a two component model [105]. The multiplicity from two the component model can be expressed as:

$$\frac{dN_{ch}}{d\eta} = \mu \times [(1-x)N_{part} + xN_{coll}] \tag{4.1}$$

, where μ fluctuates event-by-event according to negative binomial distribution with mean value $< \mu >$ equal to multiplicity in p + p collision ($< \mu > = n_{pp}$), x is the fraction of the hard component, and the N_{part} and N_{coll} are obtained from Glauber model simulations. The n_{pp} and x are treated as free parameters in the simulation and can be determined by fitting the measured $dN_{ch}/d\eta$ with the results from Monte-Carlo simulations.

Table 4.5: Centrality information for Au+Au, Cu+Cu and d+Au collisions.

		Centrality	0-5%	5-10%	10-20%	20-30%	30-40%	40-50%	50-60%	60-70%	70-80%
Run10 Au+Au	200	Refmul	>441	>375	>266	>182	>118	>72	>41	>21	>10
		Npart	350	301	236	168	116	76	48	27	14
	39	Refmul	>316	>265	>185	>125	>81	>50	>28	>15	>7
		Npart	343	293	230	163	113	75	47	28	15
	11.5	Refmul	>221	>184	>127	>86	>56	>34	>19	>10	>5
		Npart	339	289	226	160	110	73	45	26	14
	7.7	Refmul	>185	>154	>106	>72	>46	>28	>16	>8	>4
		Npart	338	289	227	161	111	73	45	26	14
Run 1 Au+Au	130	Centrality	0-6%	6-11%	11-18%	18-26%	26-34%	34-45%	45-58%	58-85%	N/A
		Refmul	>416	>367	>285	>216	>162	>104	>56	>10	N/A
		Npart	344	289	237	188	142	101	61	23	N/A
Run 2 Au+Au	19.6	Centrality	0-10%	10-30%		30-50%		50-70%		70-100%	
		Refmul	>236	>116		>47		>13		>1	
		Npart	312	188		85		32		9	
Run 4 Au+Au	200	Refmul	>519	>440	>318	>221	>149	>95	>56	>30	>13
		Npart	352	299	235	167	116	77	48	27	14
	62.4	Refmul	>372	>312	>221	>153	>101	>64	>37	>19	>8
		Npart	347	293	229	162	112	74	46	26	13
Run 5 Cu+Cu	22.4	Refmul	>85	>71	>50	>34	>23	>15	>9	N/A	N/A
		Npart	102	91	73	53	38	26	17	N/A	N/A
	62.4	Centrality	0-10%		10-20%	20-30%	30-40%	40-50%	50-60%	N/A	N/A
		Refmul	>100		>70	>48	>32	>21	>13	N/A	N/A
		Npart	96		72	52	36	25	16	N/A	N/A
	200	Refmul	>138		>97	>66	>45	>29	>18	N/A	N/A
		Npart	99		75	54	38	26	17	N/A	N/A
Run 3 d+Au	200	Centrality	0-20%			20-40%			40-100%		
		Refmul	>16			>9			>0		
		Npart	16			11			5		

Finally, we list the detail of centrality information for Au+Au, Cu+Cu and d+Au collisions in the table 4.5.

4.3   Particle Identification

Stable particles, such as protons, pions and electrons, photons, can be identified by determining their mass or the way they interact, the two characteristic properties of particles. Traditionally, the leptons and photons can be identified by measuring their interaction patterns, which is different from hadrons. Fig. 4.11 shows a traditional particle physics experiment that the different detectors stacked in layers embedding in a magnetic field and the particles go through from inner layers to outer layers, which are tracking system, electromagnatic (EM) calorimeter, hadron calorimeter and a muon system. Momentum and
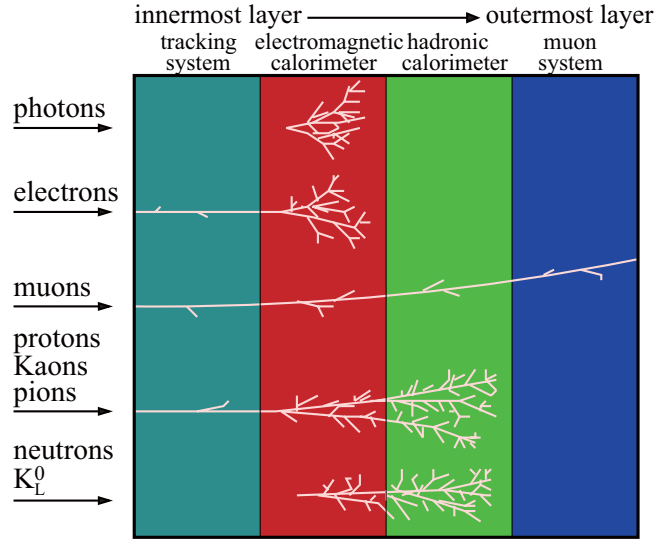
Figure 4.11: Illustration of particle identification by interaction pattern. The figure is taken from [106].

charge sign of charged particles can be determined by measuring the curvature and direction of the the tracks in the detector.

To identify hadrons and leptons unambiguously, their charge and mass have to be determined by measuring momentum and velocity simultaneously. Usually, the measured quantities, such ionization energy loss per unit track length (dE/dx) and total energy of particle are shown as a function of momentum, velocity and/or mass. The formula of energy loss per unit track length (dE/dx) was obtained by scattering theory [107]:

$$-\frac{dE}{dx} = Z \cdot \frac{4\pi r_e^2 m_e c^2 N_A}{A} \cdot \frac{z^2}{\beta^2} \cdot \left[\frac{1}{2} \ln \left(\frac{2m_e c^2 \beta^2 T_{\max}}{I^2}\right) - \beta^2 - \frac{\delta(\beta\gamma)}{2}\right] \quad (4.2)$$

, where T_{max} is the maximum kinetic energy which can be imparted to a free electron in a single collision between 10 and 100 KeV. Other variables are defined in the Table 4.6. The $4\pi r_e^2 m_e c^2 N_A/A = 0.307075$ MeV $\cdot$ g^{-1} $\cdot$ cm^2, with $A = 1$ g $\cdot$ mol^{-1}. Fig. 4.12 shows the ionization energy loss of positive muons in copper
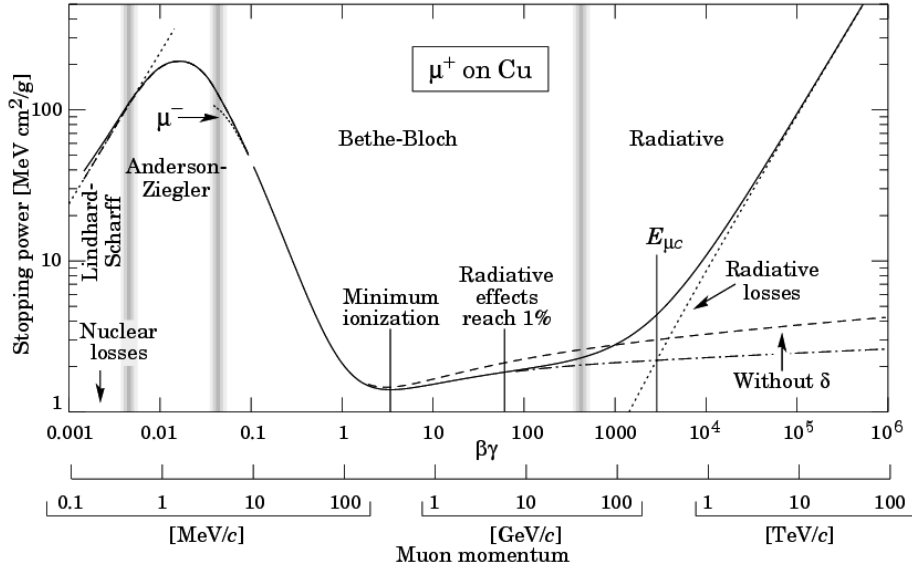
Figure 4.12: Ionization Energy Loss of μ^+ in copper. The figure is taken from [107].

as a function of $\beta\gamma = p/Mc$. In the low energy region, the average energy loss decreases as $1/\beta^2$ and reaches a broad minimum of ionization at $\beta\gamma \sim 4$. Then, the average energy loss begins to rise roughly proportional to $log(\beta\gamma)$, which is so called the relativistic rise. The rise is reduced at higher momenta by the density effect correction $\delta(\beta\gamma)$.

In the STAR experiment, the TPC is the main tracking detector, in which the momentum, trajectory and ionization energy loss (dE/dx) of charged particles can be measured. In addition to momentum, the ionization energy loss measured in the TPC can be used to identify those charged particles. Fig. 4.13 shows the ionization energy loss for protons, kaons, pions, *etc.*, as a function of particle momenta, which are measured by STAR TPC and can be used to identify charged particles. The energy resolution of the ionization energy loss measurement σ_E is the standard deviation of the gaussian distribution for the truncated mean values and is proportional to the energy deposit δ_E. The separation power for two particles A and B with different mass but the same momentum can be

Table 4.6: Definition of sympol in Bethe-Bloch formula

Quantities	Definition	Value or Unit
dE/dx	Ionization energy loss per unity length	$MeV \cdot g^{-1} \cdot cm^2$
x	$x = \rho L$	$g \cdot cm^{-2}$
ρ	Density of the absorber	$g \cdot cm^{-3}$
L	Length	cm
$\beta = \nu/c$	Reduced velocity of particle	N/A
$m_e c^2$	Electrom mass$\times c^2$	$0.510998918(44) MeV$
T	Kinetic Energy of particle	MeV
r_e	Classical electron radius, $r_e = \frac{e^2}{4\pi\epsilon_0 m_e c^2}$	$2.817940325(28) fm$
I	Mean excitation energy	eV
N_A	Avogadro's number	$6.0221415(10) \times 10^{23} mol^{-1}$
Z	Atomic number of absorber	N/A
A	Atomic mass of absorber	$g \cdot mol^{-1}$
z	Charge number of particle	N/A
$\delta(\beta\gamma)$	Density effect correction to dE/dx	N/A
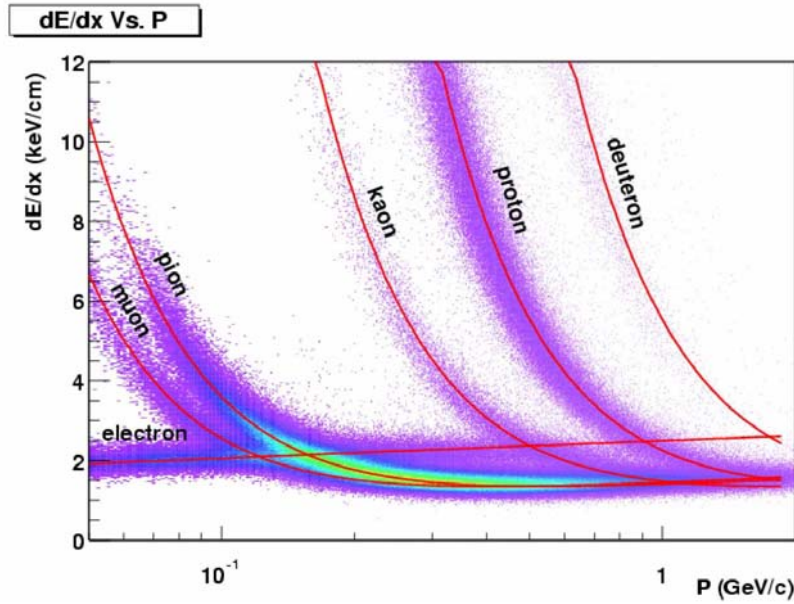
Figure 4.13: Particle identification with ionization energy loss (dE/dx), which is measured by STAR Time Projection Chamber (TPC). The solid lines in the figure are expectation line from bethe-bloch formula.
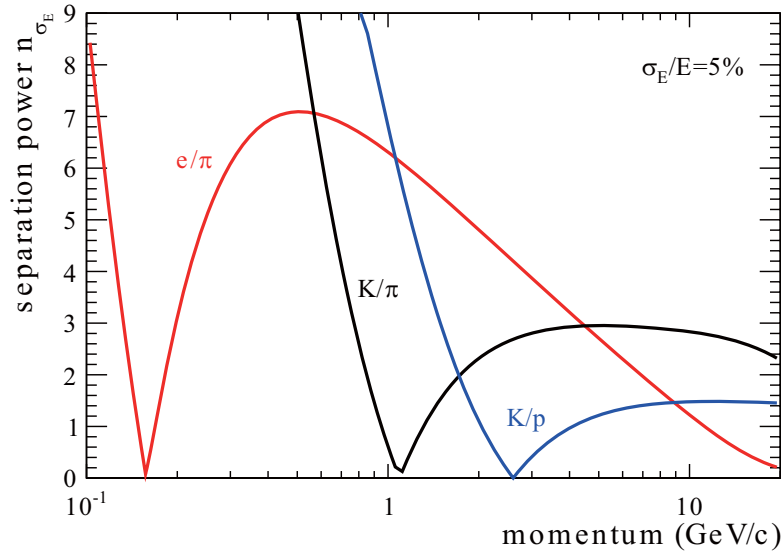
Figure 4.14: Separation power with TPC dE/dx particle identification.

calculated as:

$$n_{\sigma_E} = \frac{\delta_A - \delta_B}{< \sigma_{A,B} >} \tag{4.3}$$

, where the $< \sigma_{A,B} >$ is the average of the two resolutions $< \sigma_{A,B} > = (\sigma_A + \sigma_B)/2$. The relative energy resolution for each particle we used is $\sigma_E/E = 5\%$. The separation power for different particles as a function of momentum is shown in Fig. 4.14.

To ensure good gaussian distributions, another variable is constructed to identify particles in the STAR experiment, which is defined as:

$$Z = \frac{\log[(dE/dx)|_{measure} / (dE/dx)|_{theory}]}{\sigma_E} \tag{4.4}$$

, where the σ_E represents the energy resolution. Since we don't know the particle velocity to calculate the theory value of dE/dx, we may obtain several Z values by assuming the the particle type, such as proton, pion, kaon, electron, *ect..* In Fig. 4.15, we show the dE/dx as a function of rigidity for protons, kaons,
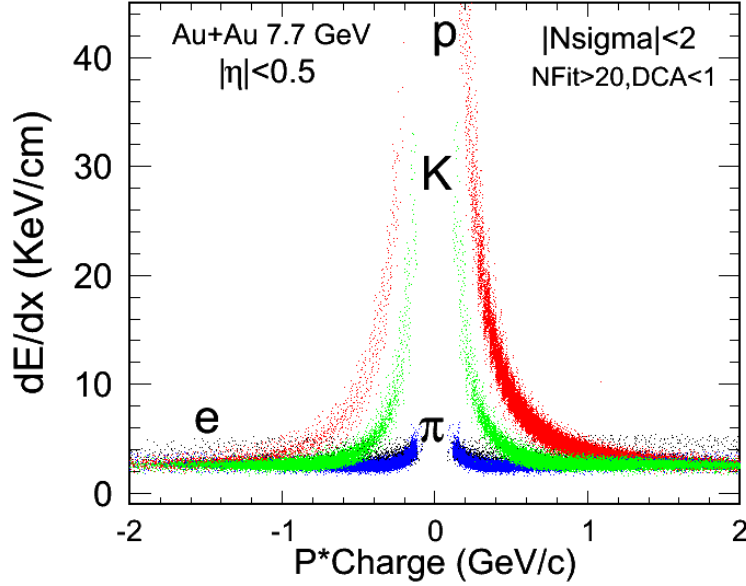
Figure 4.15: dE/dx versus rigidity for Au+Au collisions at $\sqrt{s_{\mathrm{NN}}}$=7.7 GeV.

pions and electrons after applying the cut $|Z| < 2$, number of points used in fit procedure larger than 20 and distance of closest approach smaller than 1 cm. We find that the band for protons, kaons, pions are well separated. Fig. 4.16 shows the Z variable distributions by assuming that the particle is a proton within $0.4 < p_T < 0.5$ GeV/c for Au+Au 0-5% centrality collisions at $\sqrt{s_{\mathrm{NN}}}$=7.7 GeV. The dashed lines shown in Fig. 4.16 represent a multi-gaussian fit to the Z value. From left to right, those dashed lines denote pions, electrons, kaons and protons, respectively.

In our higher moments of net-proton distribution analysis, we select protons and anti-protons event-by-event by using cut $|Z_p| < 2$ within transverse momenta $0.4 < p_T < 0.8$ GeV/c and rapidity $-0.5 < y < 0.5$. Those cuts allows us to get a high purity of the proton and anti-proton sample and similar detection efficiency between protons and anti-protons.

Another detector used to identify particles in our analysis is the Time of flight

nSigmaProtonPos_pT0.5_b1	
Entries	2184661
Mean	-3.066
RMS	5.849
χ^2 / ndf	1204 / 139
p	8328 $\pm$ 23.5
π	4.043e+004 $\pm$ 9.221e+001
e	2.013e+004 $\pm$ 1.467e+001
K	4720 $\pm$ 110.9
$\sigma_{\pi,e}$	1.498 $\pm$ 0.003
dσ(p)	0.1007 $\pm$ 0.0023
d$\sigma(\pi$-p)	-6.808 $\pm$ 0.004
dσ(e-π)	1.718 $\pm$ 0.020
dσ(K-e)	1.23 $\pm$ 0.03
σ_K	1.24 $\pm$ 0.01
σ_p	0.9985 $\pm$ 0.0030
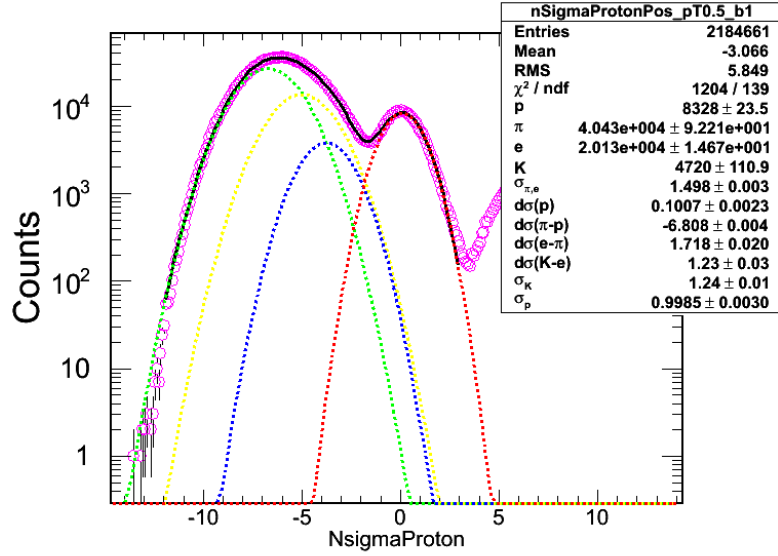
Figure 4.16: NsigmaProton (Z) distribution within $0.4 < p_T < 0.5$ GeV/c for Au+Au central collisions at $\sqrt{s_{\mathrm{NN}}}$=7.7 GeV.
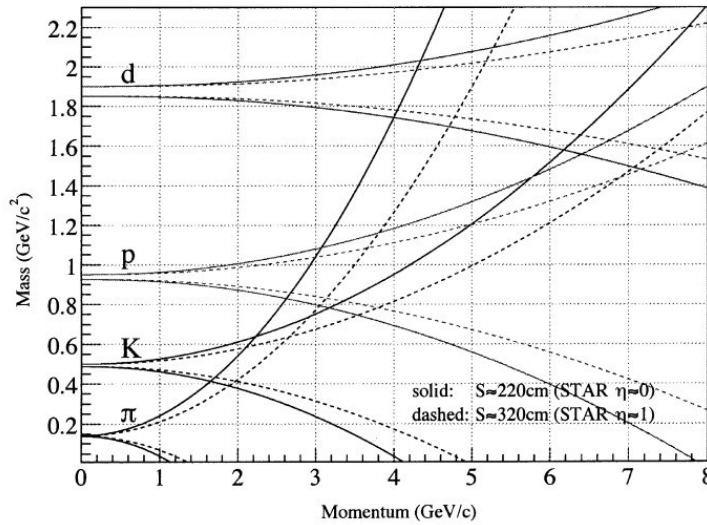
Figure 4.17: The momentum dependence of the particle identification capabilities of a TOF system with a timing resolution of 100 ps in the STAR geometry and with the STAR TPC's resolution on the track momentum and path length. The figure is taken from [84].

98

detector (TOF), which measures the flight time of a particle from the primary vertex of the collision. Once the time of flight and path length information are obtained, we can directly calculate the velocity of the particles and their mass.

$$\beta \;=\; \frac{\nu}{c} = \frac{L}{ct} \tag{4.5}$$

$$m^2 \;=\; (\frac{1}{\beta^2} - 1) \times p = (\frac{c^2 t^2}{L^2} - 1) \times p \tag{4.6}$$

Then, the mass resolution of a TOF measurement is given by:

$$\frac{dm}{m} = \frac{dp}{p} + \gamma^2(\frac{dt}{t} + \frac{dL}{L}) \tag{4.7}$$

By assuming the time resolution $\Delta_t = 100ps$ and path length $\delta_L/L = 0.2\%$ and
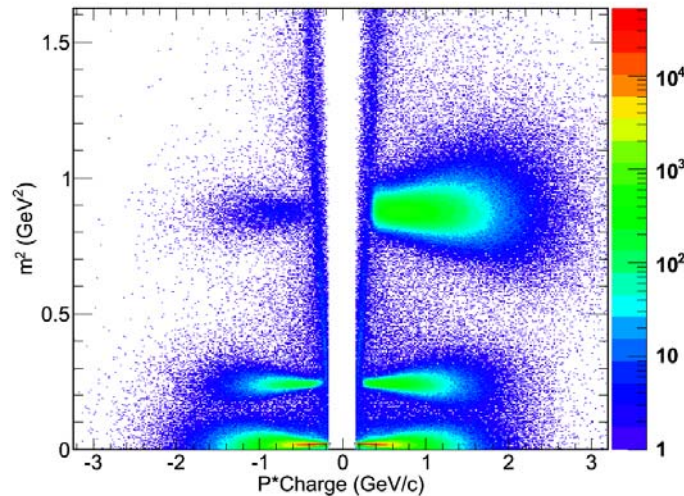
Figure 4.18: Mass square versus rigidity for Au+Au collisions at $\sqrt{s_{\mathrm{NN}}} = 7.7$ GeV within mid-rapidity.

momentum resolution $\delta_p/p = 1.3\%$, we have the mass separation shown in the Fig. 4.17. The momentum at which an upper line for a particle touches the lower line for another particle is the maximum momentum for which 2σ PID is possible via STAR TOF with a $100ps$ time resolution assumption. Fig. 4.18

shows the mass square as a function of rigidity for Au+Au collision at $\sqrt{s_{\mathrm{NN}}}$=7.7 GeV within mid-rapidity. In our analysis, we use mass square cut $0.8 < m^2 < 1$ GeV^2/c^4 to select proton and anti-proton within the p_T range $0.2 < p_T < 3$ GeV/c.

Finally, we summarize the track quality cut and PID cut in the table 4.7 at the end of this sub-section.

Table 4.7: Track Quality and PID Cut

Track Quality Cut	TPC PID Cut	TOF PID Cut
$Dca<$ 1cm		
$NFitPts>20$	$\lvert Z_p\rvert<2$	$0.8 < m^2 < 1(GeV^2/c^4), \lvert Z_p\rvert < 3$
$NFitPts/NFitPoss > 0.52$		

4.4 Centrality Bin Width Effect

The centralities in our analysis are defined as the fraction of total hadronic cross section and determined by the uncorrected reference charged particle multiplicity (refmult) $dN_{ch}/d\eta$ measured at mid-rapidity ($\lvert y\rvert < 0.5$) by the TPC in the STAR experiment. Before calculating various moments of net-proton distributions for one centrality, such as $0 - 5\%$, $5 - 10\%$, we should consider the so called Centrality Bin Width Effect (CBWE) arising from impact parameter fluctuations due to the finite centrality bin width. We must correct for this effect, as it may cause a dramatically different centrality dependence.

To formulate and demonstrate the centrality bin width effect, we write the event-by-event net-proton distributions in one centrality as:

$$P(N) = \sum_i \omega_i f^{(i)}(N), (\sum_i \omega_i = 1) \qquad (4.8)$$

, where the ω_i and $f^{(i)}(N)$ are the weight and the net-proton distribution for i^{th}

impact parameter. The various order cumulants for the distribution $P(N)$ can be expressed as:

$$C_{1,N} = \sum_i \omega_i C_{1,N}^i = \sum_i \omega_i < N >_i \tag{4.9}$$

$$C_{2,N} = (\sum_i \omega_i C_{2,N}^i) + C'_{2,C_{1,N}^i} \tag{4.10}$$

$$C_{3,N} = (\sum_i \omega_i C_{3,N}^i) + C'_{3,C_{1,N}^i} + 3 \times C'_{1,C_{1,N}^i,1,C_{2,N}^i} \tag{4.11}$$

$$
\begin{aligned}
C_{4,N} = {} & (\sum_i \omega_i C_{4,N}^i) + C'_{4,C_{1,N}^i} + 4 \times C'_{1,C_{1,N}^i,1,C_{3,N}^i} \\
& + 6 \times C'_{1,(C_{1,N}^i)^2,1,C_{2,N}^i} - 12 \times (C'_{1,C_{1,N}^i})(C'_{1,C_{1,N}^i,1,C_{2,N}^i}) \\
& - 3 \times (C'_{2,C_{1,N}^i})^2 + 3 \times C'_{2,C_{2,N}^i}
\end{aligned}
\tag{4.12}
$$

, where the $C_{k,N}^i$ ($k = 1, 2, 3, 4$) are the kth order cumulant for the net-proton distributions $f^{(i)}(N)$; the $C'_{k,X}$ ($X = C_{m,N}^i$, $k, m = 1, 2, 3, 4$) are k^{th} order cutmulant for random variable $X = C_{m,N}^i$ under the discrete probability distribution $Prob(X) = \omega_i$; the $C'_{1,X,1,Y} = < XY > - < X >< Y >$ ($X = C_{k,N}^i$, $k = 1, 2, 3, 4$) are the first order joint cumulant for random variable X, Y under the discrete probability distribution $Prob(X, Y) = \omega_i$. We may find that the higher order cumulants $C_{k,N}$ ($k = 1, 2, 3, 4$) can be expressed by the addition of two parts, one is the weighted average of the same order cumulant of each sub-distribution $f^{(i)}(N)$, and the other part is the cumulant of lower order cumulant under the discrete weighted distributions, which stems from the fluctuation of impact parameters within the centrality and results in the centrality bin width effect.

Experimentally, the most finer centrality bin is determined by a single uncorrected reference multiplicity value (refmult) measured by TPC. Generally, we usually report our results for a wider centrality bin, such as $0-5\%, 5-10\%,$...etc., to reduce the statistical fluctuations.

To eliminate or reduce the centrality bin width effect, we have developed two

methods (described below) to calculate the various moment.

1. The method one is to calculate the various moments refmult by refmult in one wider centrality bin, such as $0 - 5\%$, and weighted averaged by the number of events in each refmult in that centrality bin:

$$\sigma = \frac{\sum\limits_{r} n_r \sigma_r}{\sum\limits_{r} n_r} = \sum\limits_{r} \omega_r \sigma_r \qquad (4.13)$$

$$S = \frac{\sum\limits_{r} n_r S_r}{\sum\limits_{r} n_r} = \sum\limits_{r} \omega_r S_r \qquad (4.14)$$

$$\kappa = \frac{\sum\limits_{r} n_r \kappa_r}{\sum\limits_{r} n_r} = \sum\limits_{r} \omega_r \kappa_r \qquad (4.15)$$

,where the n_r is the number of events in r^{th} refmult and the corresponding weight $\omega_r = n_r / \sum\limits_{r} n_r$, the σ_r, S_r, κ_r are the moments calculated in each refmult. Then, the corresponding error calculations should also be the weighted average by the number of events in each refmult within one centrality as:

$$\sigma_Y = \sqrt{\sum\limits_{i} \omega_i^2 (\sigma_x^{(i)})^2} \qquad (4.16)$$

where the ω_i is the weight in i^{th} refmult and $\sigma_x^{(i)}$ is the error of the moment x in i^{th} refmult. The error calculation for various moments can be found in the Appendix.

2. The method two is to calculate the various cumulants refmult by refmult in one wider centrality bin, such as $0 - 5\%$, and weighted averaged by the

number of events in each refmult in that centrality bin as:

$$C_2 \;=\; \frac{1}{\sum\limits_r n_r} \sum_r n_r \sigma_r^2 = \sum_r \omega_r \sigma_r^2 \tag{4.17}$$

$$C_3 \;=\; \frac{1}{\sum\limits_r n_r} \sum_r n_r S_r \sigma_r^3 = \sum_r \omega_r S_r \sigma_r^3 \tag{4.18}$$

$$C_4 \;=\; \frac{1}{\sum\limits_r n_r} \sum_r n_r \kappa_r \sigma_r^4 = \sum_r \omega_r \kappa_r \sigma_r^4 \tag{4.19}$$

Then, the various moments can be calculated as :

$$\sigma^2 \;=\; C_2 = \sum_r \omega_r \sigma_r^2 \tag{4.20}$$

$$S \;=\; \frac{C_3}{C_2^{3/2}} = \frac{\sum\limits_r \omega_r S_r \sigma_r^3}{(\sum\limits_r \omega_r \sigma_r^2)^{3/2}} \tag{4.21}$$

$$\kappa \;=\; \frac{C_4}{C_2^2} = \frac{\sum\limits_r \omega_r \kappa_r \sigma_r^4}{(\sum\limits_r \omega_r \sigma_r^2)^2} \tag{4.22}$$

,where the n_r is the number of events in the rth refmult bin and the corresponding weight $\omega_r = n_r / \sum\limits_r n_r$, the σ_r, S_r, κ_r are the moments calculated in each refmult. The error calculations are similar as in method one.

Both the two methods have been tested and can effectively remove the Centrality Bin Width Effect (CBWE). The method one is used in this thesis.

4.5   Superposition of Identical Independent Emission Sources

To understand the centrality dependence of various moments (M, σ, S, κ), we assume the colliding system consist of many *Identical Independent Emission Sources (IIES)* and the final multiplicity of particles is the sum of the multiplicities from each individual emission source [108]. The relation between various

moments and the number of emission sources for the ith centrality can be expressed as:

$$M_i \;=\; N_i \times M(x), \sigma_i^2 = N_i \times \sigma^2(x) \tag{4.23}$$

$$S_i \;=\; \frac{S(x)}{\sqrt{N_i}}, \kappa_i = \kappa(x)/N_i \tag{4.24}$$

where $M_i, \sigma_i, S_i, \kappa_i \; (i = 1, 2, ...n)$ are the moments extracted from the multiplicity distribution of the ith centrality, N_i is the number of emission sources in the ith centrality. $M(x), \sigma(x), S(x), \kappa(x)$ are the parent moments of the multiplicity distributions for each emission source. From Equs .(16) and (17), we obtain:

$$\frac{M_i}{\sum\limits_{i=1}^{n} M_i} \;=\; \frac{\sigma_i^2}{\sum\limits_{i=1}^{n} \sigma_i^2} = \frac{N_i}{\sum\limits_{i=1}^{n} N_i} \tag{4.25}$$

$$\frac{1/S_i^2}{\sum\limits_{i=1}^{n} (1/S_i^2)} \;=\; \frac{1/\kappa_i}{\sum\limits_{i=1}^{n} (1/\kappa_i)} = \frac{N_i}{\sum\limits_{i=1}^{n} N_i} \tag{4.26}$$

The equ. (18) and (19) show the connection between the number of emission sources and the various moments of multiplicity distributions. To obtain the centrality dependence of those moments, we fit the normalized mean value $M_i/\sum\limits_{i=1}^{n} M_i$ with function $f(<N_{part}>_i)$, where $<N_{part}>_i$ is the average number

of participants in i^{th} centrality. Then, we obtain:

$$M_i = f(<N_{part}>_i)(\sum_{i=1}^{n} M_i) \tag{4.27}$$

$$\sigma_i = \sqrt{f(<N_{part}>_i)(\sum_{i=1}^{n} \sigma_i^2)} \tag{4.28}$$

$$S_i = \frac{1}{\sqrt{f(<N_{part}>_i)(\sum_{i=1}^{n} 1/S_i^2)}} \tag{4.29}$$

$$\kappa_i = \frac{1}{f(<N_{part}>_i)(\sum_{i=1}^{n} 1/\kappa_i)} \tag{4.30}$$

Thus, the centrality dependence of various moments can be predicted in equ. (4.27)-(4.30) by introducing in the $IIES$ assumption. Generally, the mean value M_i is proportional to the $<N_{part}>_i$, then we have $M_i = \alpha \times <N_{part}>_i$ and $f(<N_{part}>_i) = M_i/\sum_{i=1}^{n} M_i = <N_{part}>_i / \sum_{i=1}^{n} <N_{part}>_i$. When the higher moments, such as skewness and kurtosis, evolve from peripheral to central, they are approaching to zero, which can also be understood by the distributions approach to gaussian distributions according to Central Limit Theorem (CLT). From equ. (4.27)-(4.30), it also follows that the moment products, $S\sigma$ and $\kappa\sigma^2$ are constant as a function of $<N_{part}>$.

4.6 Systematic Uncertainties

To evaluate the systematic uncertainties in our higher moment analysis, we varied some basic track quality cuts as well as PID cut, such as distance of closest approach (dca) to the primary vertex, number of points used to fit the trajectory of each track (number of fit points) and the Z variable of ionization energy loss per unit length (dE/dx) for proton measured in the TPC. The dca mainly controls the fraction of background protons which are knocked out from

the beam pipe by other particles. The selection of a sufficiently large number of fit points can suppress track splitting in the TPC. The purity of the proton samples can be controlled by the Z variable of the ionization energy loss for the protons.
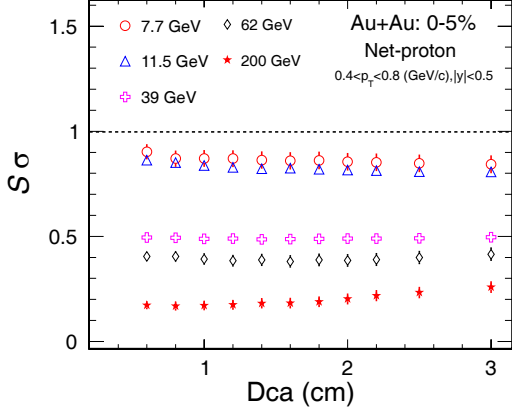
Figure 4.19: $S\sigma$ of net-proton distributions as a function of Dca for Au+Au central collisions $(0 - 5\%)$ at $\sqrt{s_{\mathrm{NN}}} = 7.7, 11.5, 39, 62.4$ and 200 GeV.
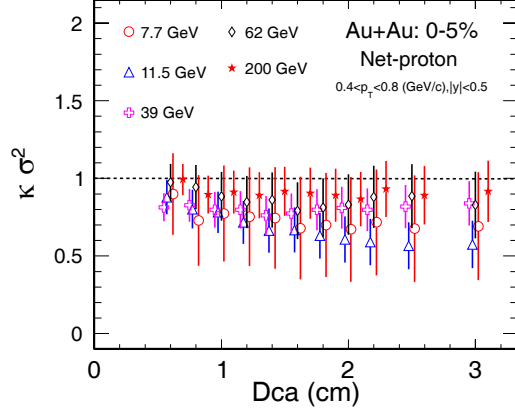
Figure 4.20: $\kappa\sigma^2$ of net-proton distributions as a function of Dca for Au+Au central collisions $(0 - 5\%)$ at $\sqrt{s_{\mathrm{NN}}} = 7.7, 11.5, 39, 62.4$ and 200 GeV.
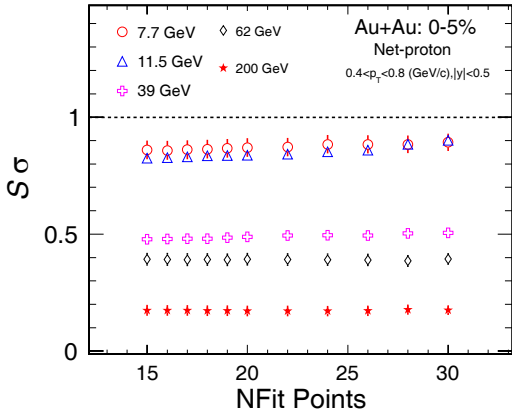
Figure 4.21: $S\sigma$ of net-proton distributions as a function of number of fit points for Au+Au central collisions $(0 - 5\%)$ at $\sqrt{s_{\mathrm{NN}}} = 7.7, 11.5, 39, 62.4$ and 200 GeV.
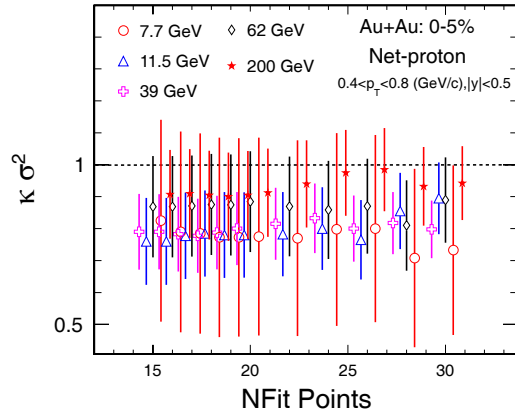
Figure 4.22: $\kappa\sigma^2$ of net-proton distributions as a function of number of fit points for Au+Au central collisions $(0 - 5\%)$ at $\sqrt{s_{\mathrm{NN}}} = 7.7, 11.5, 39, 62.4$ and 200 GeV.

Figs. 4.19 to 4.24 show the $S\sigma$ and $\kappa\sigma^2$ of net-proton distributions as a function of those three track cut conditions for Au+Au central collisions $(0-5\%)$
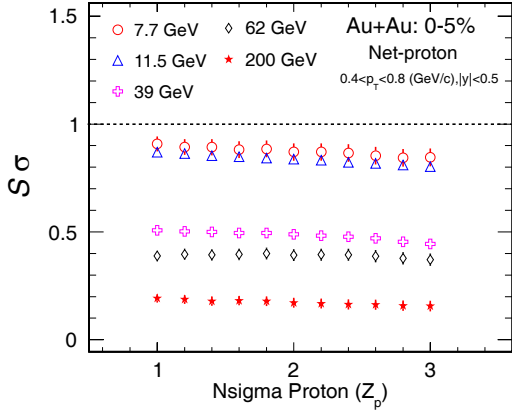
Figure 4.23: $S\sigma$ of net-proton distributions as a function of Nsigma Proton (Z_p) for Au+Au central collisions $(0-5\%)$ at $\sqrt{s_{\mathrm{NN}}} = 7.7$, 11.5, 39, 62.4 and 200 GeV.
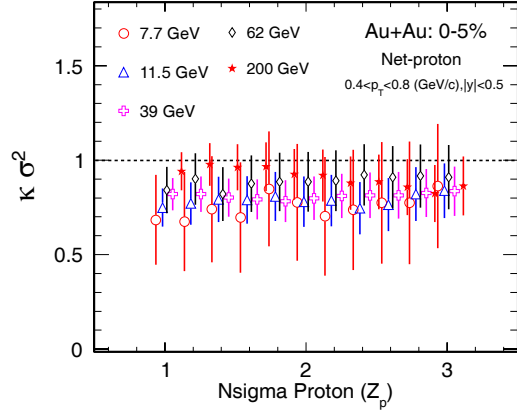
Figure 4.24: $\kappa\sigma^2$ of net-proton distributions as a function of Nsigma proton (Z_p) for Au+Au central collisions $(0-5\%)$ at $\sqrt{s_{\mathrm{NN}}} = 7.7$, 11.5, 39, 62.4 and 200 GeV.

at $\sqrt{s_{\mathrm{NN}}} = 7.7$, 11.5, 39, 62.4 and 200 GeV. We find that the $S\sigma$ and $\kappa\sigma^2$ of net-proton distributions have weak dependence on those three track cut conditions. The systematic uncertainties are evaluated by varying the above three cuts as $Dca < 1.2cm, NFitPts > 24, |Z_p| < 1.8$ and can be calculated as:

$$\frac{\delta Y}{Y} = \sqrt{(\frac{Y_1 - Y}{Y})^2 + (\frac{Y_2 - Y}{Y})^2 + (\frac{Y_3 - Y}{Y})^2} \tag{4.31}$$

, where the Y denotes the vaule of the observable that under the default cuts, the Y_i $(i = 1, 2, 3)$ are the values obtained with a new set of the track quality cuts.

CHAPTER 5

Results

In this chapter, we will present beam energy and system size dependence for the various moments (M, σ, S, κ) as well as moment products $(\kappa\sigma^2, S\sigma)$ of net-proton distributions for Au+Au collisions at $\sqrt{s_{\mathrm{NN}}} = 7.7, 11.5, 19.6, 39, 62.4, 130, 200$ GeV, Cu+Cu collisions at $\sqrt{s_{\mathrm{NN}}} = 22.4, 62.4, 200$ GeV, d+Au collisions at $\sqrt{s_{\mathrm{NN}}} = 200$ GeV and p+p collisions at $\sqrt{s_{\mathrm{NN}}} = 62.4, 200$ GeV. The protons and anti-protons are identified by the TPC detector in the STAR experiment within $0.4 < p_T < 0.8$ GeV/c and $|y| < 0.5$. First, we will show the typical event-by-event net-proton multiplicity distributions from different colliding systems. Then we studied the centrality as well as energy dependence of various moments and moment products. The statistical and systematic error are shown separately by lines and brackets, respectively. We also studied the phase space acceptance effect shown in the last sub-section.

5.1 Event-by-Event Net-proton Multiplicity Distributions

Event-by-event net-proton multiplicity distributions for various colliding systems measured within $0.4 < p_T < 0.8$ GeV/c and $|y| < 0.5$ are shown in Fig. 5.1. The Au+Au, Cu+Cu and d+Au 200 GeV from central to peripheral centralities are shown in panel (a), (c) and (d), respectively. The minimum bias results for p+p 62.4 and 200 GeV are shown in panel (b). Going from peripheral to central collisions, it is found that the distributions become wider and more symmetric for central collisions.
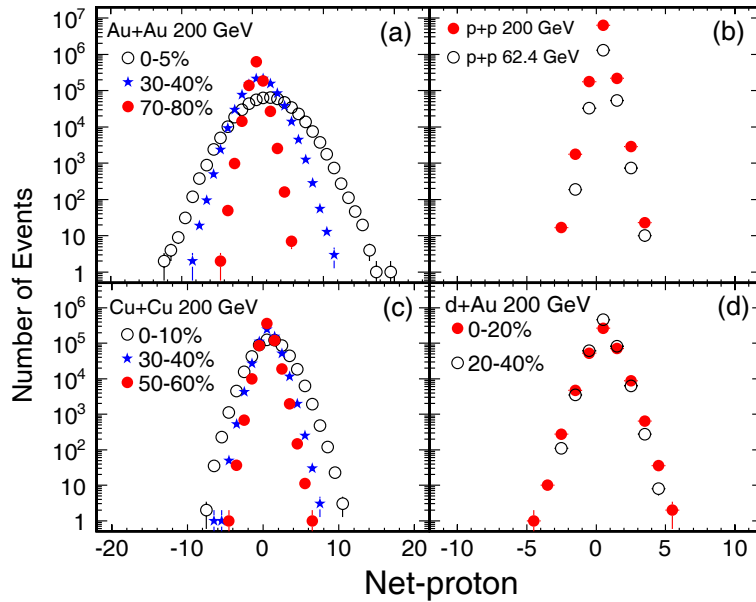
Figure 5.1: Typical event-by-event net-proton multiplicity distributions for p+p, d+Au, Cu+Cu and Au+Au collisions.

In Fig. 5.2, we show the net-proton distributions for Au+Au central collisions $(0-5\%, 19.6\text{ GeV}: 0-10\%)$ at $\sqrt{s_{\text{NN}}} = 7.7$, 11.5, 19.6, 39, 62.4 and 200 GeV.

5.2 Centrality (N_{part}) Dependence of Moments and Moment Products of Net-proton Distributions

The centrality (N_{part}) dependence for Au+Au collision at $\sqrt{s_{NN}}$=7.7, 11.5, 39, 62.4 and 200 GeV are shown in Fig. 5.3. We find that M and σ increase with N_{part} monotonically, while S and κ decrease with N_{part}. The M and S have stronger energy dependence than that of σ and κ, indicating that the net-proton distributions become more symmetric for more central collision and higher energies.

The centrality (N_{part}) dependence for various moments (M, σ, S, κ) of net-
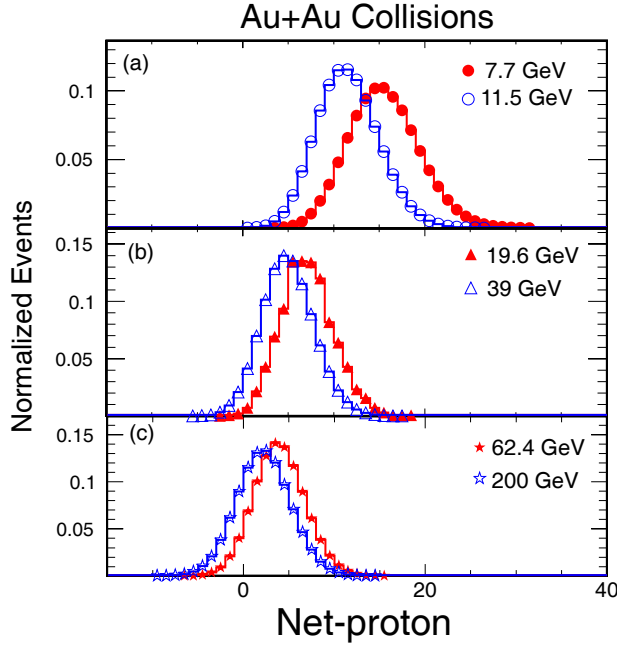
Figure 5.2: Typical event-by-event net-proton multiplicity distributions for Au+Au central collisions at $\sqrt{s_{\mathrm{NN}}}$ = 7.7, 11.5, 39, 62.4, 200 GeV.

proton multiplicity distributions from Cu+Cu collision at $\sqrt{s_{NN}}$=22.4, 62.4 and 200 GeV, d+Au collision at $\sqrt{s_{NN}}$=200 GeV and p+p collision at $\sqrt{s_{NN}}$=62.4 and 200 GeV is shown in the Fig. 5.4. The dashed lines in the Fig. 5.3 and Fig. 5.4 represent the expectations from Central Limit Theorem (CLT) when assuming the superposition of many identical and independent particle emission sources in the system. Those dashed lines are obtained in the following procedures. First, the mean values are fitted with a linear function,$f(N_{part}) = C \times N_{part}$. Thus, the CLT values for σ, S, κ can be evaluated by introducing the linear function from the fit of mean values. In Fig. 5.3 and 5.4, the centrality dependence of various moments can be well described by the dashed lines expected from CLT. Especially in Fig. 5.4, the various moments of p+p and d+Au collisions follow the CLT lines of Cu+Cu collision at the corresponding energy very well. This also supports the identical independent emission sources assumption.
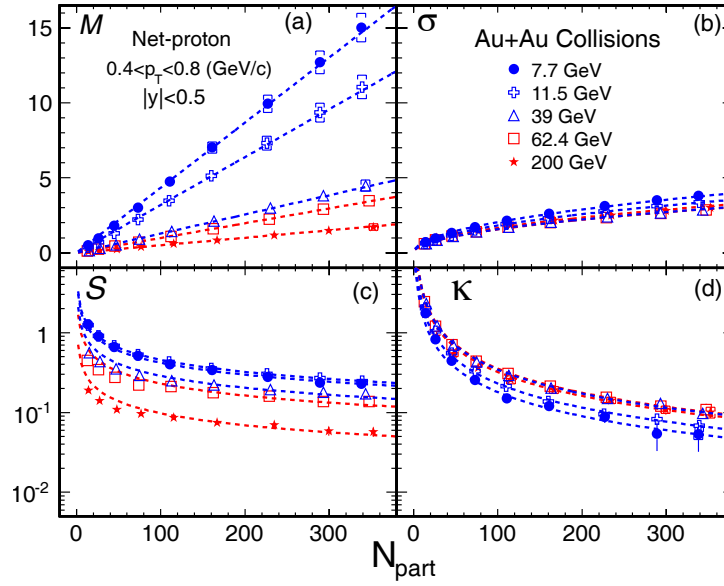
Figure 5.3: Centrality dependence of various moments of net-proton multiplicity distributions for Au+Au collisions at $\sqrt{s_{\mathrm{NN}}}$ = 7.7, 11.5, 39, 62.4, 200 GeV. The dash lines shown in the figure are expectation lines from Central Limit Theorem (CLT).

Fig. 5.5 shows the centrality dependence of moment products $S\sigma$ and $\kappa\sigma^2$ of net-proton distributions, which are directly related to the baryon number susceptibility ratio in Lattice QCD and HRG models as $\kappa\sigma^2 = \chi_B^{(4)}/\chi_B^{(2)}$ and $S\sigma = \chi_B^{(3)}/\chi_B^{(2)}$, for p+p, Cu+Cu and Au+Au collisions at various energies. $S\sigma$ shows a weak increase with centrality, while the $\kappa\sigma^2$ shows no centrality dependence. They are also smaller than their Poisson statistical values, predicted from HRG model. As the the baryon chemical potential over temperature ratio increases with the centrality, the $S\sigma$ also slightly increase with centrality (N_{part}).

5.3   Energy Dependence of the Moment Products($S\sigma$, $\kappa\sigma^2$)

In Fig. 5.6, we show the energy dependence of the $S\sigma$ and $\kappa\sigma^2$ of net-proton distributions for most central Au+Au collisions ($0 - 5\%$, 19.6 GeV: $0 - 10\%$,
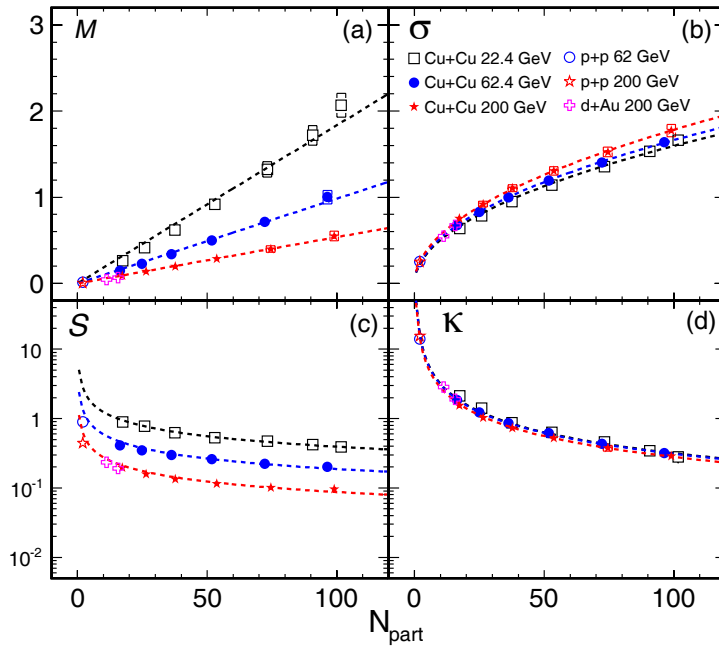
Figure 5.4: Centrality dependence of various moments of net-proton multiplicity distributions for Cu+Cu collisions at $\sqrt{s_{NN}} = 22.4$, 62.4 and 200 GeV, d+Au collisions at $\sqrt{s_{NN}} = 200$ GeV and p+p collisions at $\sqrt{s_{NN}} = 62.4$ and 200 GeV. The dash lines shown in the figure are expectation lines from Central Limit Theorem (CLT).

130 GeV: $0 - 6\%$). Lattice QCD and HRG model calculations [57, 58] are also shown for comparison. The Lattice QCD results are calculated for time extent $N_\tau = 6$ and phase transition temperature $T_c = 175$ MeV. The red dashed lines of the HRG model in the upper panel and lower panels are evaluated by $S\sigma = tanh(\mu_B/T)$ and $\kappa\sigma^2 = 1$, respectively, where the μ_B/T ratio at chemical freeze-out is parameterized as a function of colliding energy based on reference [110]. The corresponding baryon chemical potential (μ_B) at chemical freeze-out for each energy is shown in the upper band of the Fig. 5.6. We find that the moment products ($\kappa\sigma^2$ and $S\sigma$) of Au+Au collisions at $\sqrt{s_{NN}} = 200, 130, 62.4$ GeV are consistent with Lattice QCD and HRG model calculations. The $S\sigma$ and $\kappa\sigma^2$ for Au+Au collisions at $\sqrt{s_{NN}} = 39, 19.6, 11.5$ and 7.7 GeV deviate from HRG model
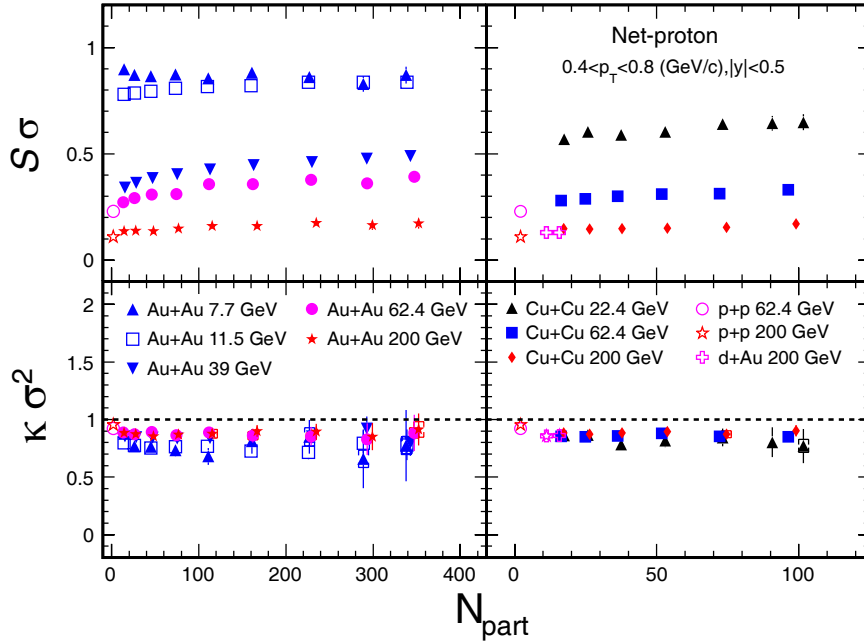
Figure 5.5: Moment products ($\kappa\sigma^2$ and $S\sigma$) of net-proton distributions for Au+Au, Cu+Cu, d+Au and p+p collisions.

calculations. Those deviations could be linked to the chiral phase transition and QCD critical point. Surprisingly, $\kappa\sigma^2$ from Lattice QCD calculations at $\sqrt{s_{\text{NN}}} = 19.6$ GeV show a negative value. This gives us a hint that there might be non-monotonic behavior between 39 GeV and 11.5 GeV. However, due to the limited statistics, the statistical errors of experimental data are large at 19.6 GeV. To confirm the trend between 39 and 11.5 GeV, the STAR currently is running to take more data at 19.6 GeV. Interestingly, as shown in Fig. 5.7, recent linear σ model calculations demonstrate that the forth order cumulant of the fluctuations for σ field will be universally negative, when the QCD critical point is approached from cross-over side [109]. It will cause the measured $\kappa\sigma^2$ as well as kurtosis (κ) of net-proton distributions to be smaller than their Poisson values.

In Fig. 5.8, we show energy dependence of $\kappa\sigma^2$ and $S\sigma$ from central ($0 - 5\%$,
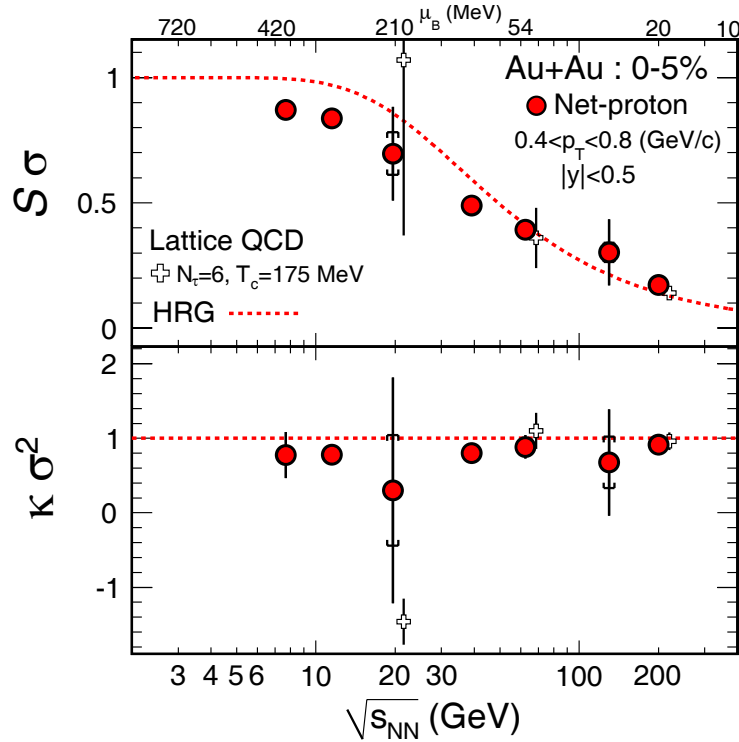
Figure 5.6: Energy dependence of moment products ($\kappa\sigma^2$ and $S\sigma$) of net-proton distributions for central Au+Au collisions ($0 - 5\%$, 19.6 GeV: $0 - 10\%$, 130 GeV: $0 - 6\%$). The red dashed lines denote the HRG model calculations, in which the $S\sigma = tanh(\mu_B/T)$ and $\kappa\sigma^2 = 1$. The empty markers denote the results calculated from Lattice QCD.

19.6 GeV: $0 - 10\%$, 130 GeV: $0 - 6\%$) to peripheral ($70 - 80\%$, 19.6 GeV: $70 - 100\%$, 130 GeV: $58 - 85\%$) collisions. It can be found that the data show little centrality dependence for all energies. The $S\sigma$ over HRG model ratios are shown in the bottom panel of the Fig. 5.8.

Fig. 5.9 shows the energy dependence of $\kappa\sigma^2$ and $S\sigma$ for Cu+Cu central collisions. The red dashed lines in the figure are obtained from the HRG model by using the formula $S\sigma = tanh(\mu_B/T)$, where the μ_B and T are from thermal model fits of the particle ratios. We find that our experimental data is consistent with HRG model expectations for $S\sigma$ of net-proton distributions. While the
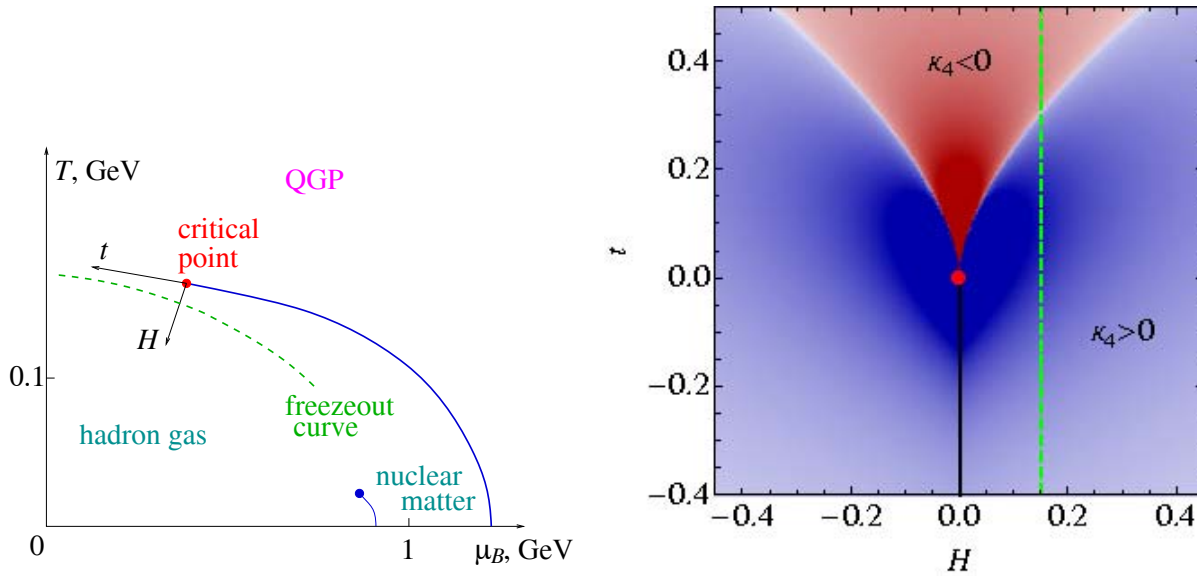
Figure 5.7: Left panel : A sketch of the phase diagram of QCD with the freezeout curve and a possible mapping of the Ising coordinates t and H. Right panel : The density plot of the function $\kappa_4(t, H)$ from the linear parametric model, the $\kappa_4 < 0$ region is red, the $\kappa_4 > 0$ is blue. κ_4 is the forth order cumulant. The green dashed lines in left panel and right panel denote the freeze out lines. The figures are taken from [109].

$\kappa\sigma^2$ deviates from HRG model calculations and monotonically decrease as the collision energy decreases.

5.4   Charged Particle Density $(dN_{ch}/d\eta)$ Scaling of $S\sigma$

As shown in Fig. 5.10, the baryon chemical potential (μ_B) at chemical freeze-out, which is extracted from the thermal model fit of particle ratios, scale with the charged particle density $(dN_{ch}/d\eta)$ at mid-rapidity for fixed colliding energies [111]. The scaling properties of μ_B combined with the moment product $S\sigma = tanh(\mu_B/T)$ from HRG model can give a hint of scaling properties of $S\sigma$ of net-proton distributions with respected to the $dN_{ch}/d\eta$. To verify this, we plot $S\sigma$ of net-proton distributions for various colliding systems including Au+Au collisions at $\sqrt{s_{\mathrm{NN}}} = 62.4$ and 200 GeV, Cu+Cu collisions at $\sqrt{s_{\mathrm{NN}}} = 22.4$, 62.4 and 200
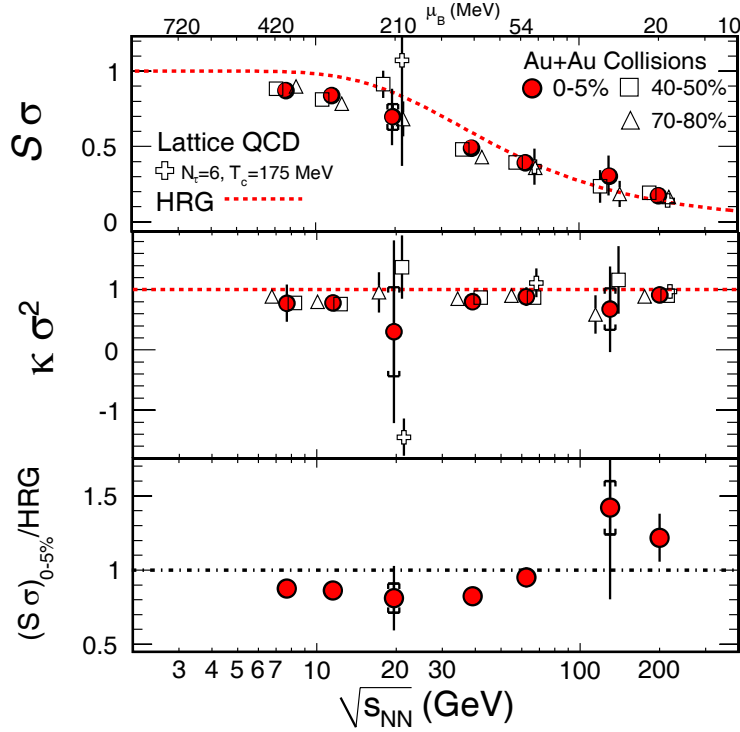
Figure 5.8: Energy dependence of moment products ($\kappa\sigma^2$ and $S\sigma$) of net-proton distributions for Au+Au collisions central ($0 - 5\%$, 19.6 GeV: $0 - 10\%$, 130 GeV: $0 - 6\%$) to peripheral ($70 - 80\%$, 19.6 GeV: $70 - 100\%$, 130 GeV: $58 - 85\%$) collisions. The mid-central for 19.6 GeV is $30 - 50\%$.

GeV, d+Au and p+p collisions at $\sqrt{s_{\mathrm{NN}}} = 200$ GeV, as a function of $dN_{ch}/d\eta$ in the Fig. 5.11 with double logarithm axis.

It is obvious that for a fixed colliding energy, such as $\sqrt{s_{NN}} = 200$ GeV, the moment products of $S\sigma$ of net-proton distributions for different system size the p+p, d+Au, Cu+Cu and Au+Au collisions have power law dependence on the charged particle density ($dN_{ch}/d\eta$). Thus, we fit the $S\sigma$ of net-proton distributions for various colliding systems with double power law formula:

$$S\sigma(dN_{ch}/d\eta, \sqrt{s_{NN}}) = \alpha \times (dN_{ch}/d\eta)^\beta \times (\sqrt{s_{NN}})^\gamma \qquad (5.1)$$
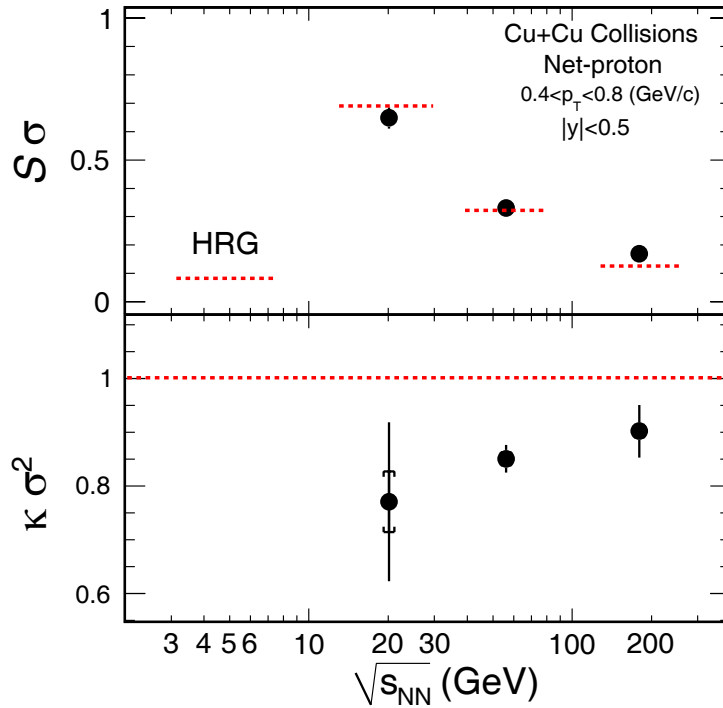
Figure 5.9: Energy dependence of moment products ($\kappa\sigma^2$ and $S\sigma$) of net-proton distributions for Cu+Cu central collisions ($0 - 10\%$, 22.4 GeV: $0 - 5\%$). The dashed lines shown in the figures are from HRG model calculations, in which $S\sigma = tanh(\mu_B/T)$ and $\kappa\sigma^2$=1.

The fitting results are shown in the Table. 5.1. The $S\sigma$ can be well described by the power law formula $S\sigma = \frac{11}{3} \times (\frac{1}{s^4}\frac{dN_{ch}}{d\eta})^{\frac{1}{12}}$, where the s is the square of the center of mass energy. For high energy heavy ion collisions the temperature is approximately constant and the ratio $\mu_B/T << 1$, thus we have the approximation $\mu_B/T \sim tanh(\mu_B/T) = S\sigma = \frac{11}{3} \times (\frac{1}{s^4}\frac{dN_{ch}}{d\eta})^{\frac{1}{12}}$. This denotes the relation between μ_B/T and the charged particle density and colliding energy for high energy nuclear collisions. Thus, based on the event-by-event fluctuation observable $S\sigma$ of net-proton distributions, we can predict the scaling properties of the thermodynamic parameter μ_B/T as shown in Fig. 5.10.

Multiplicity fluctuations and inclusive yields are two basic properties in high
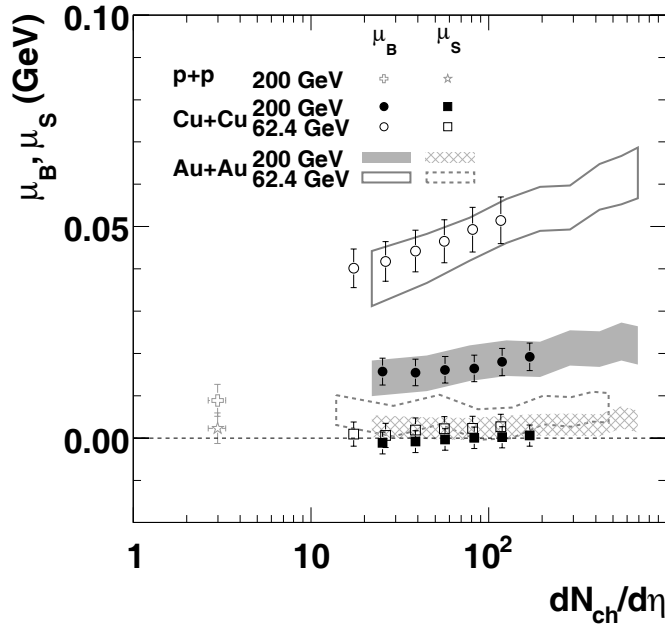
Figure 5.10: Scaling Properties of Chemical Potential: μ_B and μ_S versus $dN_{ch}/d\eta$

energy heavy ion collisions. For a thermal system, both the fluctuations and yields should be described by the thermodynamic parameters (μ_B and T), which completely determine the properties of the thermal system. The fluctuation observable $S\sigma$ of most central net-proton distributions versus thermodynamic parameter μ_B/T ratio, which is extracted from the thermal model fit of the particle ratio, is shown in the Fig. 5.12 for various colliding systems. Lattice

Table 5.1: Fitting parameters for $S\sigma$ as a function of $dN_{ch}/d\eta$

Parameters	Value	Approx.
χ^2/ndf	34.08/37	0.92
α	3.669±0.1358	$\frac{11}{3}$
β	0.0853±0.003927	$\frac{1}{12}$
γ	-0.6796±0.00693	$-\frac{2}{3}$
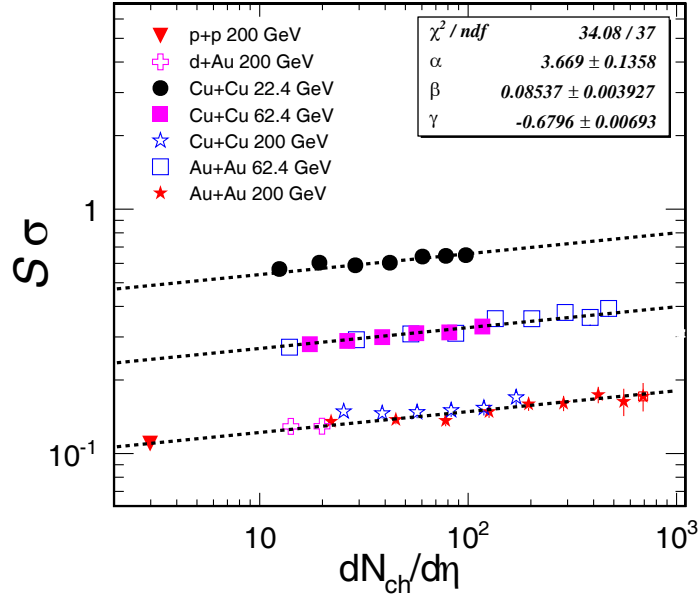
Figure 5.11: $S\sigma$ of net-proton distributions as a function of charged particle density at mid-rapidity $(dN_{ch}/d\eta)$ for various colliding systems. The dashed lines in the figures is the fitting lines.

QCD calculations with $N_\tau = 6$ and $T_c = 175$ MeV and the HRG model relation $S\sigma = tanh(\mu_B/T)$ are also shown in Fig. 5.12 for comparison.

We find that high energy heavy ion collisions, such as Au+Au and Cu+Cu collisions, are consistent with Lattice QCD and HRG model calculations, while the elementary p+p collision deviate from the HRG model calculations. In addition to the perfect description of the particle yields by the thermal model, the agreement of higher order fluctuations with thermal model predications provide further evidence that the colliding system has achieved thermalization in high energy heavy ion collision.

To investigate the behavior of the mid-central and peripheral collisions, the centrality dependence $(dN_{ch}/d\eta)$ of the $S\sigma$ over HRG model ratio is shown in Fig. 5.13 for various colliding systems. We find that even in peripheral collisions the $S\sigma$ of net-proton distributions for high energy heavy ion collisions data
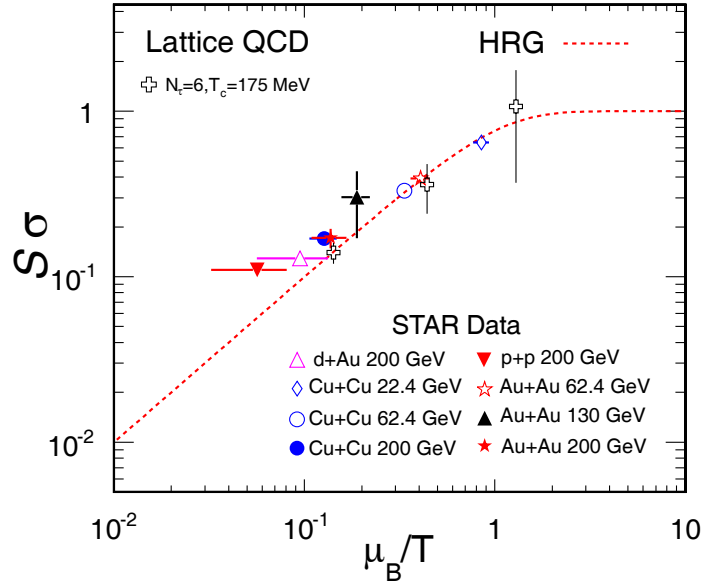
Figure 5.12: $S\sigma$ of net-proton distributions as a function of baryon chemical potential over temperature ratio (μ_B/T) for various colliding systems. The red dashed line in the figures is the result of the HRG model. Lattice QCD results with $N_\tau = 6$ and $T_c = 175$ MeV are also shown in the figure.

are consistent with the HRG model calculations. The p+p data shows some deviations but with large errors.

5.5 Scale for the QCD Phase Diagram

Lattice QCD results for $\kappa\sigma^2$ and $S\sigma$ are obtained for dimensionless parameters T/T_c and μ_B/T, where T_c is the transition temperature at $\mu_B = 0$. For a given value of energy $(\sqrt{s_{\rm NN}})$, the experimental observables are calculated at the corresponding chemical freeze-out, characterized by T and μ_B. Thus, comparison of experiment and theory requires a choice of the scale, T_c. By varying this scale to obtain the best fit between the QCD predications and the experimental measurements, we are able to determine the T_c. This is the first direct comparison between results from a heavy ion experiment and lattice QCD of strongly
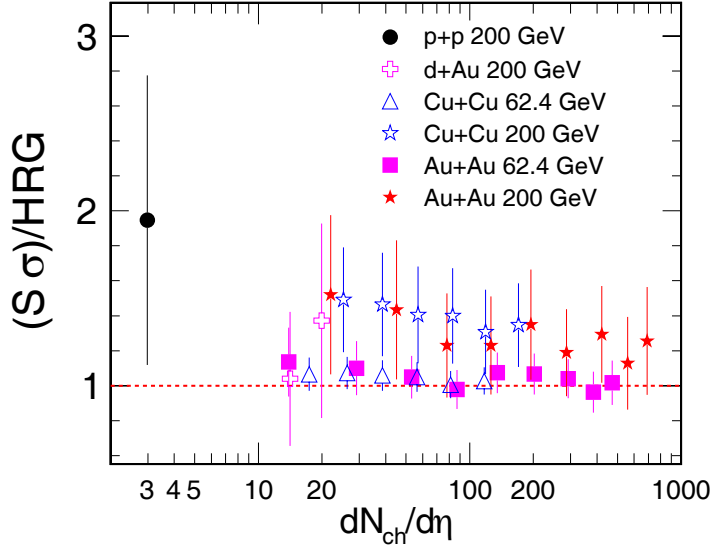
Figure 5.13: $S\sigma$ of net-proton distributions over HRG calculations ratio as a function of charged particle density at mid-rapidity $(dN_{ch}/d\eta)$ for various colliding systems within $0.4 < p_T < 0.8$ GeV/c and $|y| < 0.5$.

interacting bulk matter. The observable that we choose for comparison is $\kappa\sigma/S$. The lattice computation of the $\kappa\sigma/S$ has the smallest systematic uncertainties among the three explored here ($\kappa\sigma^2$, $S\sigma$, $\kappa\sigma/S$), and thus is the best quantity to use to constrain T_c.

Figure 5.14 (left panel) shows the comparison of $\kappa\sigma/S$ between experimental results from Au ion collisions and lattice QCD predictions. The information here is that we have shown lattice predictions obtained with different values of T_c. The errors shown on the experimental data points are statistical (lines) and systematic (brackets) errors [56]. The systematic errors were estimated by varying the following requirements for $p(\bar{p})$ tracks: track quality cuts used in track reconstruction, and the $p(\bar{p})$ identification criteria. The errors bars on the lattice predictions are statistical errors on the lattice computation with cutoff of $1/a \simeq 960-1000$ MeV. The lattice spacing effects and the effect of tuning the bare quark mass are the main sources of remaining uncertainties in the predictions.
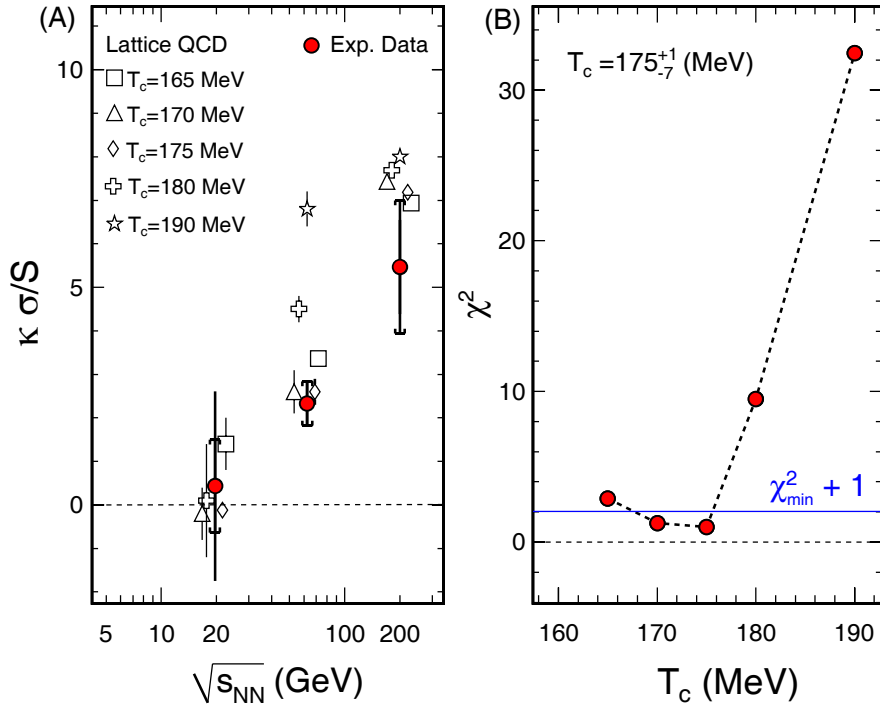
Figure 5.14: Comparison of $\kappa\sigma/S$ from experiment and lattice predictions, and the extraction of T_c. (A): $\kappa\sigma/S$ of net-proton distribution measured in collisions of Au ions at varying $\sqrt{s_{NN}}$ and with an impact parameter of less than 3 fm. This is compared to lattice QCD predictions with cutoff $1/a \simeq 960 - 1000$ MeV for the corresponding ratio of susceptibilities extrapolated to the freeze-out conditions using different values of T_c. The lattice results at each $\sqrt{s_{NN}}$ are slightly shifted for clarity in presentation. (B): The comparison of experimental data and lattice QCD predictions, shown through χ^2 as a function of T_c using the definition given in Equ. 5.3. This yields the estimate of T_c and its errors as discussed in the text.

These are not parameterized as systematic uncertainties. However, it is known that their effect is small at the two highest values of $\sqrt{s_{\mathrm{NN}}}$ [57].

In order to arrive at a quantitative estimate of the scale parameter T_c we perform a standard statistical analysis. For each value of T_c we compute, as usual,

$$\chi^2(T_c) = \sum_{\sqrt{s_{NN}}} \frac{[\mathrm{m}_3^{\mathrm{expt}}(\sqrt{s_{NN}}) - \mathrm{m}_3^{\mathrm{QCD}}(\sqrt{s_{NN}}, T_c)]^2}{\mathrm{Error}_{\mathrm{expt}}^2 + \mathrm{Error}_{\mathrm{QCD}}^2} \tag{5.2}$$

where $m_3 = \kappa\sigma/S$. The lattice predictions are obtained for a grid of T_c spaced by 5-10 MeV. Closer spacing of this grid would require computations which are beyond the scope of this study. The minimum of χ^2, corresponding to the most probable value of the parameter being estimated, occurs at $T_c = 175$ MeV. The standard errors on the parameter are the values of T_c for which χ^2 exceeds the minimum value by unity. It is clear from Figure 5.14 (right panel) that this is bounded by $+5$ and -10. A piece-wise linear interpolation between the grid points yields the more reliable error estimate, $+1$ and -7. By comparing different interpolation schemes we estimate find that the error estimate is stable. As a result we conclude that

$$T_c = 175^{+1}_{-7} \ \mathrm{MeV}. \tag{5.3}$$

The error estimates include systematic and statistical errors on experimental data but only statistical errors on the lattice QCD computations. The result in Equ. 5.3 is compatible with current indirect estimates of T_c which come from setting the scale of thermal lattice QCD computations via hadronic observables. This provides a first check in bulk hot and dense matter for the standard model of particle physics.

5.6   Phase Space Acceptance Study

The Lattice QCD and HRG model calculations of high order moments of net-proton fluctuations are based on the grand canonical ensemble framework. To make sure the applicable of grand canonical ensemble in heavy ion collision, it requires that the considering sub-system size should be small enough comparing with the rest parts of the collision system, which can be seen as a heat bath. Nevertheless, the phase space coverage of the sub-system should not be too small, otherwise we are losing physics information and only with statistical fluctuations observed [112, 113].

On the other hand, in grand canonical ensemble the baryon number fluctuate event-by-event and only are conserved on average. While in the heavy ion collisions, the net-baryon number are exactly conserved in each event, which could suppress the net-baryon number fluctuations. This is so called baryon number conservation effect in heavy ion collision. Although, the net-proton is not conserved quantity, protons will still contribute a large amount to the total baryon number, especially in the low energy heavy ion collision. When we tune down the colliding energy, due to baryon stopping, larger fraction of the total baryon number, which is mostly carried by protons, will be observed at low energy than at high energy. A natural question that people may ask is how the effect of phase space acceptance affect our higher moment of net-proton distributions as well as the comparisons to the HRG model and Lattice QCD calculations. To address those questions, we have studied the transverse momentum coverage as well as rapidity window size dependence of the higher moments of net-proton distributions. The results will be shown in the following sub-sections.

5.6.1   Transverse Momentum (p_T) Acceptance Dependence

We have investigated the p_T acceptance dependence of the higher moments of net-proton distributions. To extend our p_T coverage, we will use the Time of Flight (TOF) detector to identify the protons and anti-protons in event-by-event bias with Run 10 Au+Au collision data ($\sqrt{s_{\mathrm{NN}}}$ = 7.7, 11.5, 39 and 200 GeV).

To remove background events for low energy data ($\sqrt{s_{\mathrm{NN}}}$ = 7.7, 11.5, 39 GeV), such as out of time events, beam pipe evens, we have applied some event bias quality cuts on the data sets. Fig. 5.15 shows the TOF matched track multiplicity as a function of reference multiplicity for Au+Au collisions at $\sqrt{s_{\mathrm{NN}}}$ = 7.7, 11.5, 39 GeV. In addition to requiring events with the number of matched tracks larger than zero, we also apply a cut where only events above the straight lines shown in the Fig. 5.15 are used.

In Run 10 Au+Au 39 and 200 GeV, the Vertex position detector (Vpd) is also used to measure the start time for time-of-flight measurements and determine the z-coordinate of the collision vertex via the time difference between east and west Vpd detector ($VpdVz$) for its good time resolution performance. Since the start time is important for TOF particle identification, we require the $|Vz - VpdVz| <$ 3 cm to suppress the pile-up events and select good timing events, which have good starting time. In Fig. 5.16, we show the difference between z-coordinate of primary vertex (Vz) determined by global fitting of the tracks in TPC and z-coordinate of the collision vertex measured by Vpd ($VpdVz$).

Fig. 5.17 shows the TOF matching efficiency for proton, kaon and pion, which is defined as:

$$TOF_{eff}(x) = \frac{N_{tracks}(TOFMatching, |y| < 0.5)}{N_{tracks}(|Z_x| < 2, |y| < 0.5)} \tag{5.4}$$

, where $x =$proton,kaon,pion and Z_x is the logarithm of the measured $\langle dE/dx \rangle$ divided by the theoretical expectation for ionization energy loss of the corre-
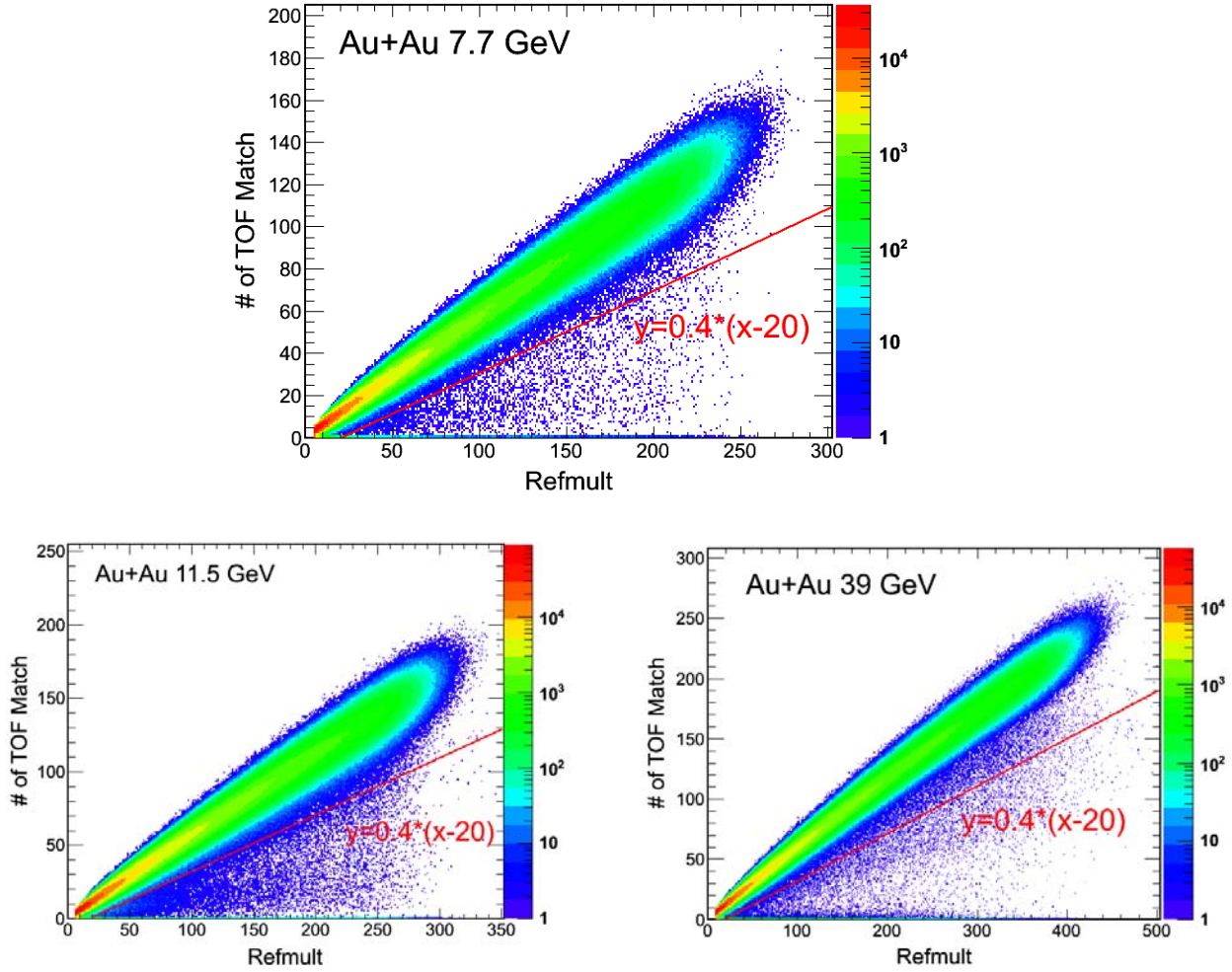
Figure 5.15: TOF matched track multiplicity as a function of reference multiplicity for Au+Au collisions at $\sqrt{s_{\mathrm{NN}}} = 7.7$, 11.5, 39 GeV. The straight lines in the figures are the boundary condition for the event selection.
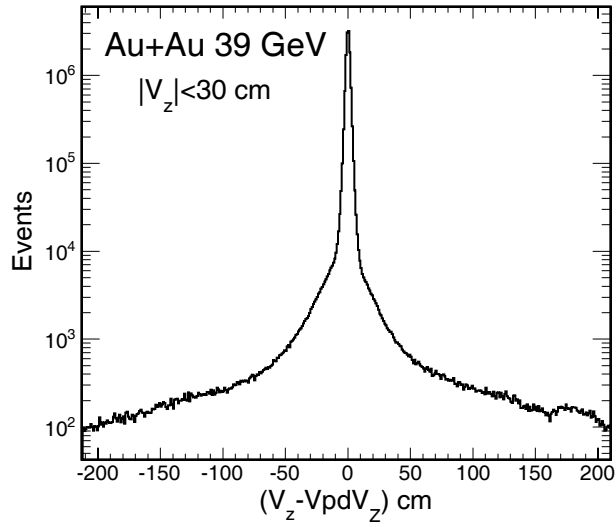
Figure 5.16: Difference between z-coordinate of primary vertex (Vz) and z-coordinate of the collision vertex measured by Vpd ($VpdVz$).
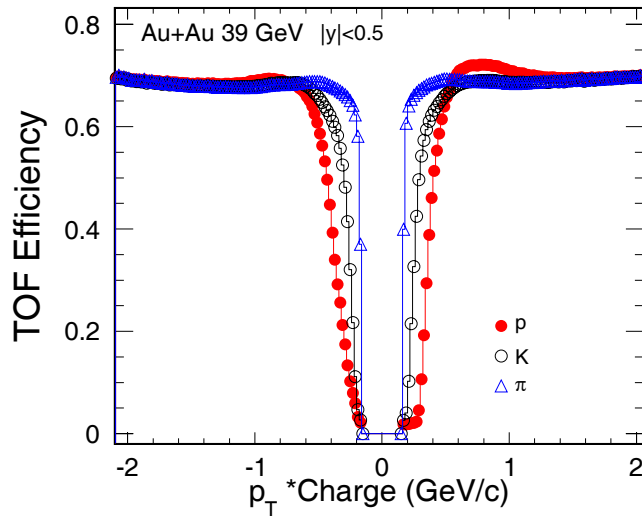
Figure 5.17: TOF matching efficiency for proton, kaon and pion in Au+Au 39 GeV.

sponding particle type x. Due to decay effects and particle scattering with the materials, the TOF efficiency for low p_T protons, kaons and pions is with the order of $TOF_{eff}(p) < TOF_{eff}(k) < TOF_{eff}(\pi)$. The TOF matching efficiency increase with transverse momentum (p_T) and saturates at about 70% with $p_T = 0.6$ GeV/c. For TOF PID, the mass square ($0.8 < m^2 < 1$ GeV/c^2) and Z_p ($|Z_p| < 3$) are used to identify protons and anti-protons.
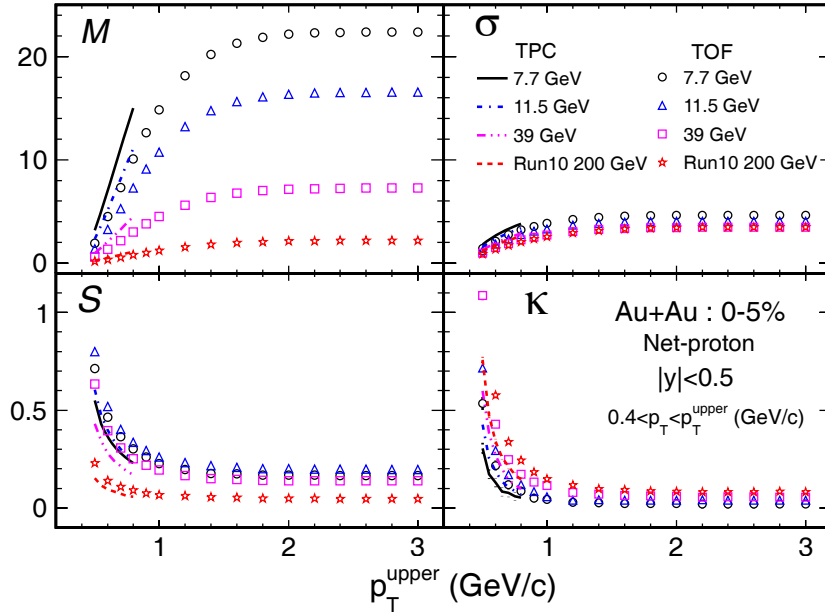
Figure 5.18: Various moments (M, σ, S, κ) of net-proton distributions with TPC (lines) and TOF PID as a function of p_T coverage for Run 10 Au+Au central collisions at $\sqrt{s_{NN}} = 7.7$, 11.5, 39 and 200 GeV.

Various moments (M, σ, S, κ) of net-proton distributions with TPC and TOF PID as a function of p_T coverage for Run 10 Au+Au collisions at $\sqrt{s_{NN}} = 7.7$, 11.5, 39 and 200 GeV are shown in Fig. 5.18. We can see that M and σ are increase with the extended p_T coverage, while the S and κ are decreasing monotonically. All of the moments saturate at $p_T^{upper} \sim 2$ GeV/c. As shown in the Chapter III, due to detector efficiency effects, the M, σ (S, κ) measured by

TPC are expected larger (smaller) than those measured by TOF.
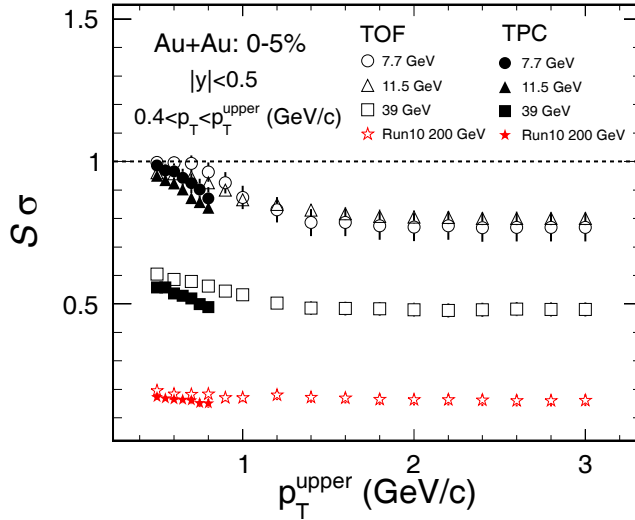
Figure 5.19: $S\sigma$ of net-proton distributions with TPC and TOF PID as a function of p_T coverage for Run 10 Au+Au central collisions at $\sqrt{s_{\mathrm{NN}}} = 7.7$, 11.5, 39 and 200 GeV.

The corresponding moment products $S\sigma$ and $\kappa\sigma^2$ are shown in the Fig. 5.19 and Fig. 5.20. The $S\sigma$ and $\kappa\sigma^2$ of net-proton distributions for low energy Au+Au collisions at $\sqrt{s_{\mathrm{NN}}} = 7.7$, 11.5 and 39 GeV measured by TPC and TOF decrease with increasing p_T coverage and saturate at about $p_T \sim 1$ GeV/c, while there is almost no p_T coverage dependence for Au+Au 200 GeV. One may find that there are some differences between the results measured by TOF and by the TPC. This should result from the fact that the efficiency difference between protons and anti-protons measured by TOF is bigger than measurements by the TPC due to the absorbtion and scattering of anti-protons by materials before reaching TOF.

To further investigate the p_T coverage dependence of the higher moments, the various moments of net-proton distributions with TOF PID within p_T bin width 0.1 GeV/c are shown in Fig. 5.21. As the relative low efficiency at low p_T, the starting p_T bin is chosen to be $0.3 \sim 0.4$ GeV/c. The various moments
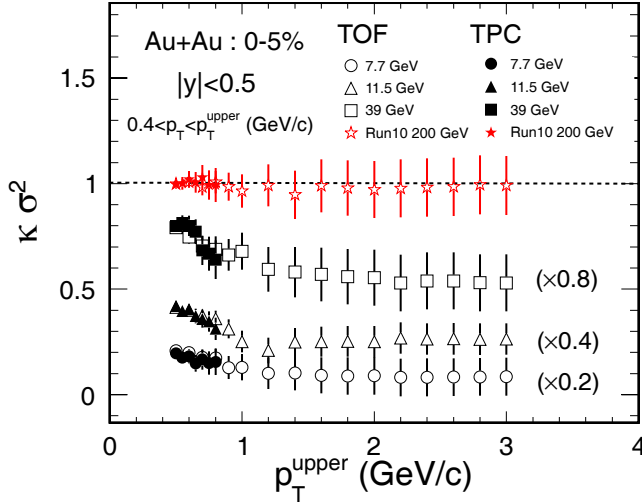
Figure 5.20: $\kappa\sigma^2$ of net-proton distributions with TPC and TOF PID as a function of p_T coverage for Run 10 Au+Au central collisions at $\sqrt{s_{\mathrm{NN}}} = 7.7$, 11.5, 39 and 200 GeV.

of net-protons show non-monotonic dependence on the differential p_T.

The moment products ($\kappa\sigma^2$, $S\sigma$) of net-proton distributions as well as the corresponding HRG model calculations denoted by lines are shown in Fig. 5.22 and Fig. 5.23. For each transverse momentum interval of 0.1 GeV/c, the $\kappa\sigma^2$ and $S\sigma$ are constant and consistent with HRG model calculations. Here, the HRG model results are calculated by the formula $S\sigma = tanh(\mu_B/T)$, which is obtained within the grand canonical ensemble framework. To obtain energy dependence, the μ_B/T ratio is parameterized by collision energy $\sqrt{s_{\mathrm{NN}}}$ via chemical freeze out condition determined by thermal model fits of the experimental particle yield and/or ratio.

5.6.2 Rapidity Window Acceptance Dependence

To ensure the purity and similar efficiency of protons and anti-protons identified by ionization energy loss per unit length (dE/dx) measured by TPC in
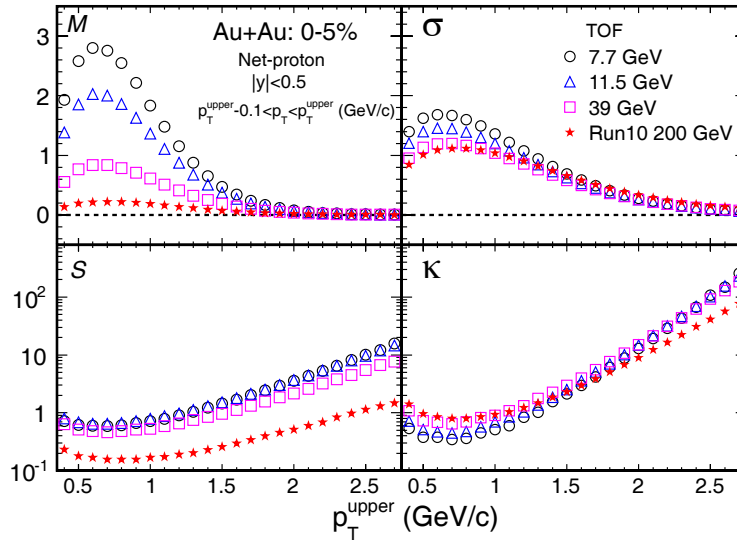
Figure 5.21: Various Moments (M, σ, S, κ) of net-proton distributions as a function of differential p_T coverage with TOF PID for Au+Au central collisions at $\sqrt{s_{\mathrm{NN}}} = 7.7, 11.5, 39, 200$ GeV

STAR experiment, protons and anti-protons are selected within $0.4 < p_T < 0.8$ GeV/c. In addition to the effective TPC η acceptance, $|\eta| < 1$, the proton and anti-proton rapidity acceptance is about $|y| < 0.7$.

Various moments (M, σ, S, κ) of net-proton distributions with TPC PID as a function of rapidity window size $(-\Delta y/2 < y < \Delta y/2)$ for Au+Au central collisions $(0 - 5\%)$ at $\sqrt{s_{\mathrm{NN}}} = 7.7, 11.5, 39, 62.4$ and 200 GeV (Run4) are shown in Fig. 5.24. The mean (M) and width (σ) monotonically increase with increasing rapidity window size, while S and κ decrease with increasing the proton rapidity window size.

Fig. 5.25 and 5.26 respectively show the $S\sigma$ and $\kappa\sigma^2$ of net-proton distributions as a function of the proton rapidity window size for Au+Au central collisions. We find that the $S\sigma$ and $\kappa\sigma^2$ of net-proton distributions have no rapidity window size dependence at high energy ($\sqrt{s_{\mathrm{NN}}}$= 62.4 and 200 GeV)

Figure 5.22: $S\sigma$ as a function of differential p_T with TOF PID for Au+Au central collisions at $\sqrt{s_{\mathrm{NN}}} = 7.7, 11.5, 39, 200$ GeV. The lines in the figures are HRG model calculations for each energy.

Figure 5.23: $\kappa\sigma^2$ as a function of differential p_T with TOF PID for Au+Au central collisions at $\sqrt{s_{\mathrm{NN}}} = 7.7, 11.5, 39, 200$ GeV. The line in the figures is the HRG model calculations.
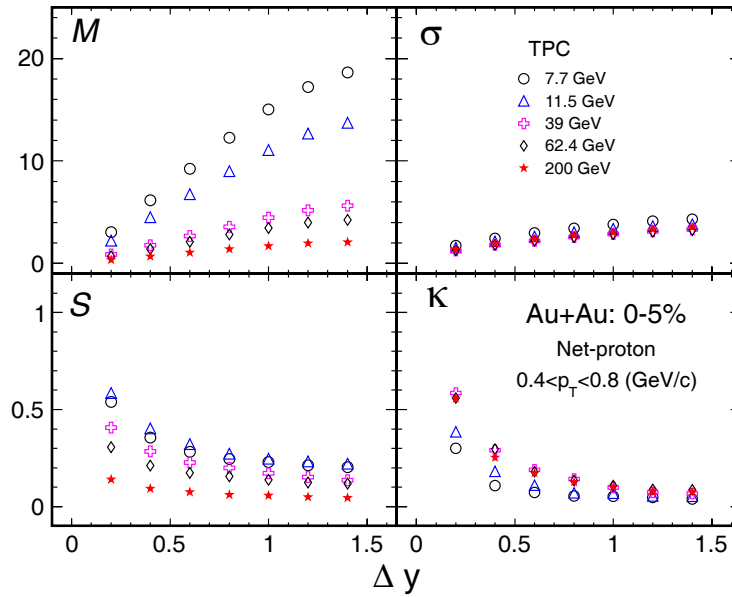
Figure 5.24: Various Moments (M, σ, S, κ) of net-proton distributions as a function of rapidity window size with TPC PID for Au+Au central collisions at $\sqrt{s_{NN}} = 7.7, 11.5, 39, 62.4, 200$ GeV.

Au+Au central collisions while it has a small dependence (within 10%) for low energy ($\sqrt{s_{NN}} = 7.7, 11.5, 39$ GeV).

The rapidity window size dependence results for Cu+Cu central collisions at energies $\sqrt{s_{NN}} = 22.4, 62.4$ and 200 GeV are shown in Fig. 5.27 and 5.28, respectively. The $S\sigma$ of net-proton distributions have no dependence on the rapidity window size while the $\kappa\sigma^2$ decrease (within 10%) with increasing the size of rapidity window and saturate at about $\Delta y \sim 1$.

To extend the phase space coverage, we also use TOF to identify protons and anti-protons within $0.4 < p_T < 2$ GeV/c. Fig. 5.29 and 5.30 show the $S\sigma$ and $\kappa\sigma^2$ of net-proton distributions with TOF PID varying with rapidity window size for Au+Au central collisions. The $S\sigma$ and $\kappa\sigma^2$ for Au+Au central collisions at $\sqrt{s_{NN}} = 7.7, 11.5$ and 39 GeV decrease with increasing rapidity coverage till
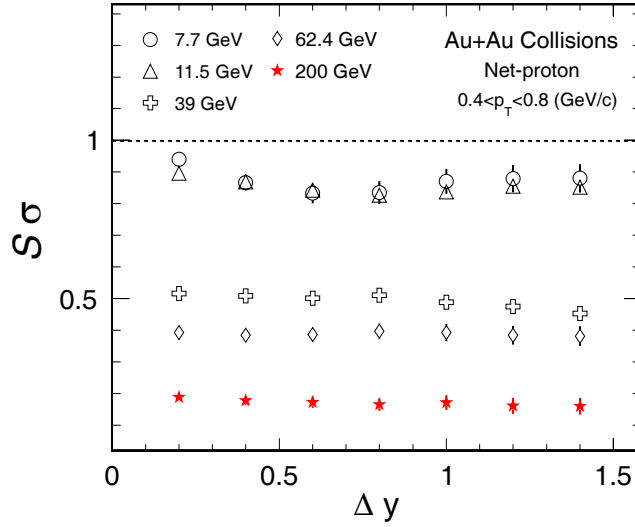
Figure 5.25: Rapidity window size dependence of $S\sigma$ for Au+Au central collisions $(0-5\%)$ at $\sqrt{s_{\mathrm{NN}}} = 7.7, 11.5, 39, 62.4$ and 200 GeV.
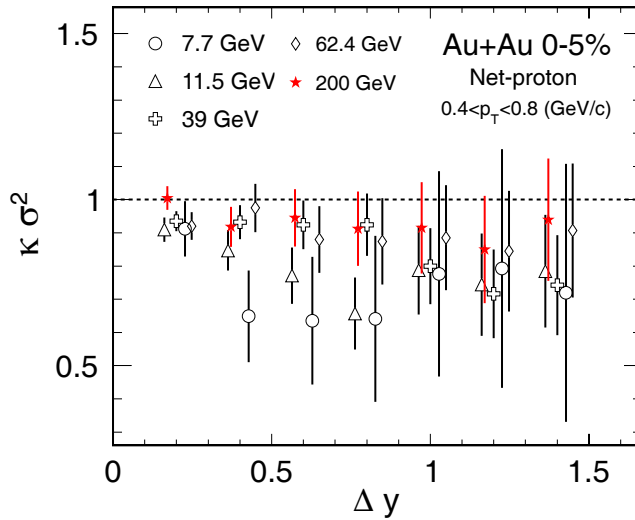
Figure 5.26: Rapidity window size dependence of $\kappa\sigma^2$ for Au+Au central collisions $(0-5\%)$ at $\sqrt{s_{\mathrm{NN}}} = 7.7, 11.5, 39, 62.4$ and 200 GeV.
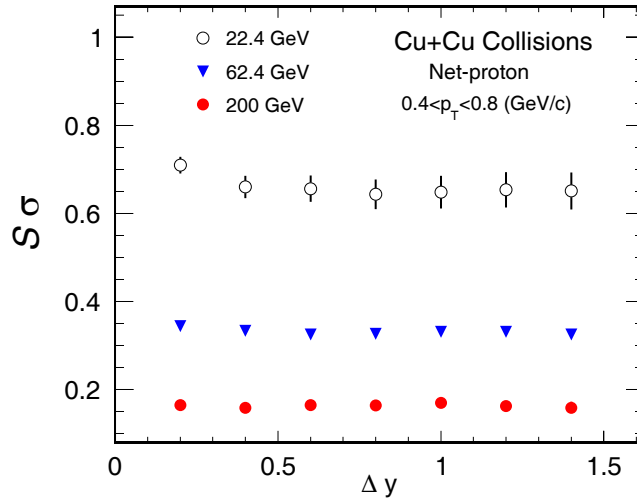
Figure 5.27: Rapidity window size dependence of $S\sigma$ for Cu+Cu central collisions $(0 - 10\%, 22.4 \text{ GeV}: 0 - 5\%)$ at $\sqrt{s_{\mathrm{NN}}} = 22.4, 62.4, 200$ GeV.
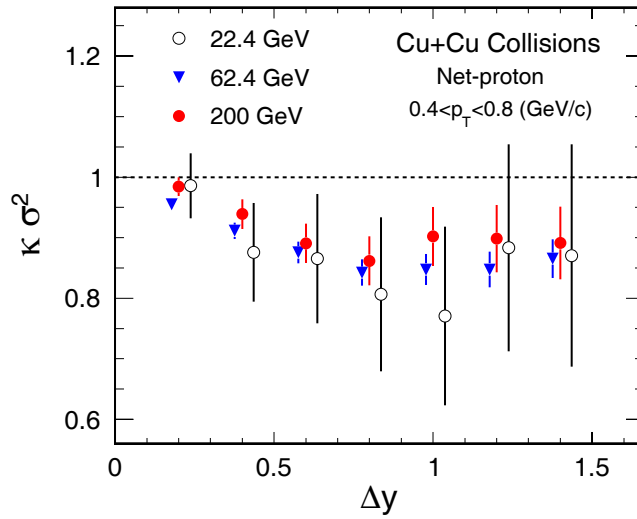
Figure 5.28: Rapidity window size dependence of $\kappa\sigma^2$ for Cu+Cu central collisions $(0 - 10\%, 22.4 \text{ GeV}: 0 - 5\%)$ at $\sqrt{s_{\mathrm{NN}}} = 22.4, 62.4, 200$ GeV.
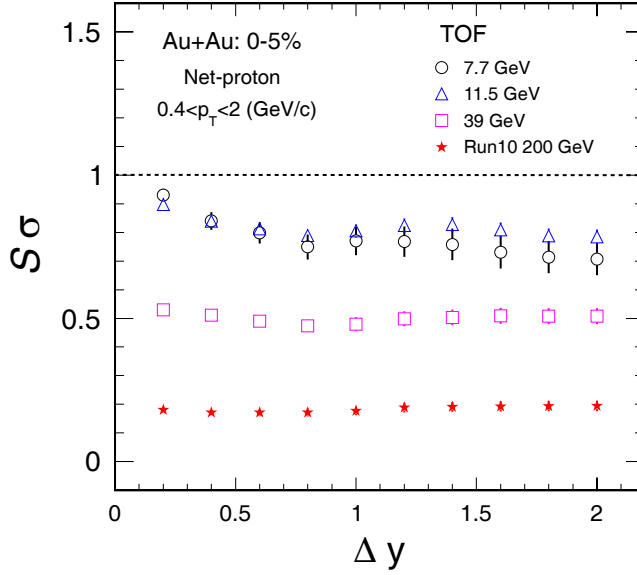
Figure 5.29: Rapidity window size dependence of $S\sigma$ of net-proton distributions with TOF PID for Au+Au central collisions $(0-5\%)$ at $\sqrt{s_{\mathrm{NN}}} = 7.7, 11.5, 39$ and Run10 200 GeV.
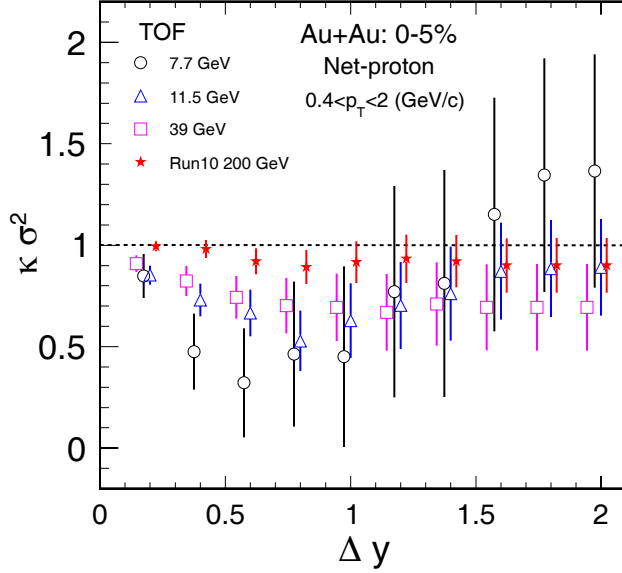
Figure 5.30: Rapidity window size dependence of $S\sigma$ of net-proton distributions with TOF PID for Au+Au central collisions $(0-5\%)$ at $\sqrt{s_{\mathrm{NN}}} = 7.7, 11.5, 39$ and Run10 200 GeV.

$\Delta y \sim 1$, then show a slightly increasing trend. No rapidity size dependence was observed for Au+Au central collision at $\sqrt{s_{\mathrm{NN}}} = 200$ GeV.
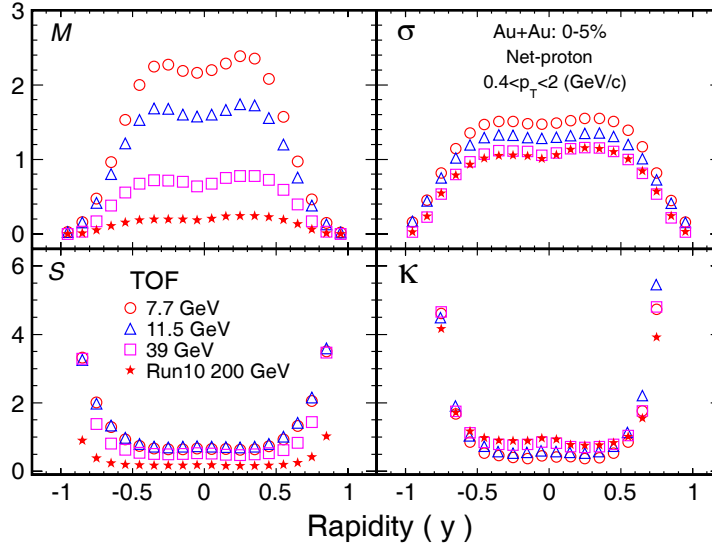
Figure 5.31: Various Moments (M, σ, S, κ) of net-proton distributions as a function of differential rapidity $(\delta y = 0.1)$ with TOF PID for Au+Au central collisions at $\sqrt{s_{\mathrm{NN}}} = 7.7, 11.5, 39, 200$ GeV (Run10).

To better understand the rapidity window size dependence, we also studied the various moments of net-proton distributions as a function of differential rapidity $(\delta y = 0.1)$ with TOF PID for Au+Au central collisions. The results are illustrated in Fig. 5.31. It shows that various moments are almost flat for rapidity interval $\delta y = 0.1$ within mid-rapidity $(|y| < 0.5)$. We observe that in the top left panel of Fig. 5.31, the smaller the colliding energy the higher the mean value of the net-proton distributions. This is due to the larger nuclear stopping power for low energy than that in high energy nuclear collision.

We also plot the $S\sigma$ and $\kappa\sigma^2$ of net-proton distributions for Au+Au central collisions with TOF PID in the Fig. 5.32 and Fig. 5.33. The $S\sigma$ and $\kappa\sigma^2$ show flat results within mid-rapidity and rise at forward rapidity. Due to different baryon
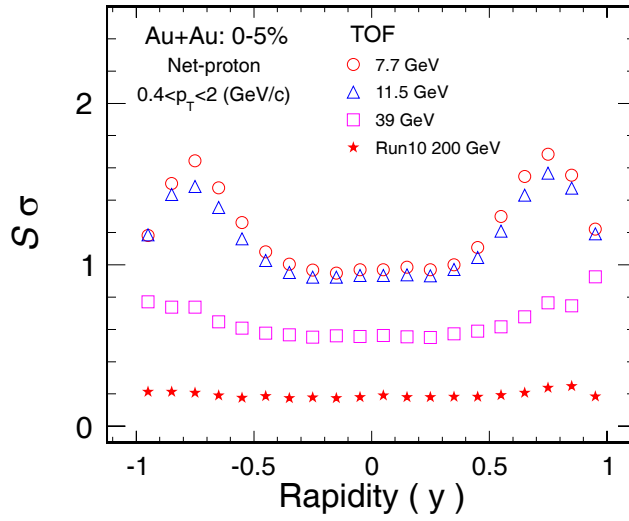
Figure 5.32: Differential rapidity dependence (interval $\delta y = 0.1$) of $S\sigma$ for Au+Au central collisions at $\sqrt{s_{\mathrm{NN}}} = 7.7, 11.5, 39, 200$ GeV (Run10).
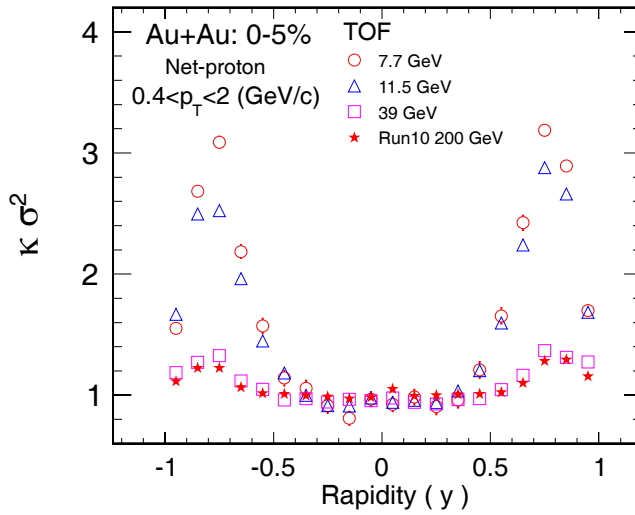
Figure 5.33: Differential rapidity dependence (interval $\delta y = 0.1$) of $\kappa\sigma^2$ for Au+Au central collisions at $\sqrt{s_{\mathrm{NN}}} = 7.7, 11.5, 39, 200$ GeV (Run10).

138

stopping power for different energies, there should be a larger fraction of initial protons for low energy that are transported into the central region than high energy. A large fraction of initial protons (forward rapidity region) may results in non-equilibrium effects which deviate from the HRG model calculations. It also may indicate the our observables are sensitive to non-equilibrium effects.

Based on the study of phase space (p_T and y) coverage dependence (integral and differential) study, we notice that the various moments (M, σ, S, κ) and moment products $(S\sigma, \kappa\sigma^2)$ of net-proton distributions are indeed with the transverse momentum (p_T) and/or rapidity (y) coverage dependence. As the moments (M, σ, S, κ) of net-proton distributions are extensive variables, their values are sensitive to the volume of the system and particle multiplicities in the phase space coverage.

The intensive variable $S\sigma$ and $\kappa\sigma^2$, which are sensitive to the correlation length, are expected to be independent on the volume of the system. From differential p_T and rapidity dependence study, we have found that in the mid-rapidity ($|y| < 0.5$), the $S\sigma$ and $\kappa\sigma^2$ obtained in the differential p_T ($\delta p_T = 0.1$ GeV/c) or rapidity (δy=0.1) are constant and consistent with HRG model calculations. This should be caused by the statistical fluctuations (Poisson statistics) in the relative small phase space coverage. When we extend our coverage of the p_T and/or rapidity (y), the characteristic correlation length and thus physics messages can be probed by our observables. Supposing that the total phase space coverage δp can be divided into phase space segments ($\delta p_1, \delta p_2, \delta p_3...\delta p_i$), then we have:

$$\delta p = \delta p_1 + \delta p_2 + \delta p_3 + ... + \delta p_i \tag{5.5}$$

If each segment is independent (no correlations), we obtain:

$$S\sigma \;=\; \frac{C_3(\delta p)}{C_2(\delta p)} = \frac{\sum\limits_{i=1}^{n} C_3(\delta p_i)}{\sum\limits_{i=1}^{n} C_2(\delta p_i)} = \frac{C_3(\delta p_i)}{C_2(\delta p_i)} \tag{5.6}$$

$$\kappa\sigma^2 \;=\; \frac{C_4(\delta p)}{C_2(\delta p)} = \frac{\sum\limits_{i=1}^{n} C_4(\delta p_i)}{\sum\limits_{i=1}^{n} C_2(\delta p_i)} = \frac{C_4(\delta p_i)}{C_2(\delta p_i)} \tag{5.7}$$

, where the additive property of the cumulants is used. According to Fig. 5.22, Fig. 5.23, Fig. 5.32 and Fig. 5.33, the results for $S\sigma$ and $\kappa\sigma^2$ are constant for different p_T or rapidity segments, but have different values when the $S\sigma$ and $\kappa\sigma^2$ are evaluated in the integral p_T or rapidity coverage. This can be expressed as:

$$S\sigma \;=\; \frac{C_3(\delta p)}{C_2(\delta p)} \neq \frac{\sum\limits_{i=1}^{n} C_3(\delta p_i)}{\sum\limits_{i=1}^{n} C_2(\delta p_i)} = \frac{C_3(\delta p_i)}{C_2(\delta p_i)} \tag{5.8}$$

$$\kappa\sigma^2 \;=\; \frac{C_4(\delta p)}{C_2(\delta p)} \neq \frac{\sum\limits_{i=1}^{n} C_4(\delta p_i)}{\sum\limits_{i=1}^{n} C_2(\delta p_i)} = \frac{C_4(\delta p_i)}{C_2(\delta p_i)} \tag{5.9}$$

, which indicates that the net-proton distributions in each p_T or rapidity segment are correlated with each other and not independent, otherwise the results evaluated in the integral phase space coverage should be the same in the phase space segment. The correlations between net-proton distributions in each phase space segment may be caused by baryon number conservation or other physics mechanism. It should not be the resonance decay effects, because the results in integral phase space coverage for Au+Au 200 GeV are the same as in the differential one.

As we have mentioned, the phase space coverage should not be smaller than the characteristic correlation length of the system, otherwise only statistical fluc-

tuations are probed by our observables and the physics information will be lost. And also the rapidity window should be concentrated at mid-rapidity with one unit ($|y| < 0.5$) to avoid enhancing the fraction of the initial protons thus introducing non-equilibrium effects at low energy. In our main part of data analysis, with the TPC PID, the phase space coverage of rapidity window size $|y| < 0.5$ and p_T coverage $0.4 < p_T < 0.8$ GeV/c is large enough to keep the physics information. Since our observables are sensitive to the correlation length and non-equilibrium effects, we expect that we can observe critical signals even with the baryon number conservation effects present.

CHAPTER 6

Summary and Outlook

The main goal of the higher moments analysis in heavy ion collisions is to probe the bulk properties, such as phase structure and thermalization, of hot dense nuclear matter and test the QCD theory in the non-perturbative region, where it is rarely tested by experiments. As a direct application, for the first time, the higher moments of net-proton distributions have been applied to search for signatures of the QCD critical point, due to the high sensitivity to the correlation length (ξ). In this thesis, the world's first comprehensive and systematic measurements and studies of the beam energy and system size dependence for higher moments (M, σ, S, κ) as well as moment products ($\kappa\sigma^2$, $S\sigma$) of net-proton multiplicity distributions have been presented with a broad energy range and different system sizes, which include Au+Au collisions at $\sqrt{s_{\mathrm{NN}}} = 200$, 130, 62.4, 39, 19.6, 11.5 and 7.7 GeV (including BES energies), Cu+Cu collisions at $\sqrt{s_{\mathrm{NN}}} = 200$, 62.4 and 22.4 GeV, d+Au collisions at $\sqrt{s_{\mathrm{NN}}} = 200$ GeV, p+p collisions at $\sqrt{s_{\mathrm{NN}}} = 200$ and 62.4 GeV.

A characteristic signature for the existence of a QCD critical point would be the non-monotonic dependence of the observations on the collision centrality and/or energy ($\sqrt{s_{\mathrm{NN}}}$). It was found that the centrality dependence of various moments (M, σ, S, κ) are consistent with the expectations evaluated from the Central Limit Theorem (CLT) by assuming superposition of many independent emission sources. The moment product $\kappa\sigma^2$ shows no centrality dependence while $S\sigma$ shows a weak centrality dependence. Then energy dependence is studied by

142

comparing the results from the Au+Au 200 GeV to those from the BES ener-
gies. The moment products $\kappa\sigma^2$ and $S\sigma$ of net-proton distributions from central
Au+Au collisions are consistent with Lattice QCD and HRG model calculations
at high energy (200, 130, 62.4 GeV) while deviating from (smaller than) HRG
model calculations at $\sqrt{s_{\mathrm{NN}}} = 39$, 19.6, 11.5 and 7.7 GeV. The deviations could
potentially be linked to chiral phase transitions and QCD critical point. Surpris-
ingly, Lattice QCD calculations got negative value for $\kappa\sigma^2$ at $\sqrt{s_{\mathrm{NN}}} = 19.6$ GeV.
This is a hint that there might be a non-monotonic behavior between 39 and
11.5 GeV. But the experimental data is with large error bar due to the limited
statistics. Fortunately, this ambiguity can be clarified soon by Run11 19.6 GeV
data with higher statistics. Recent model calculations show that the $\kappa\sigma^2$ value
will always be smaller than its Poisson statistical expectation value 1, when QCD
critical point is approached from the high energy cross-over side.

The mutual agreements between the μ_B/T extracted from thermal model
fits of particle ratio and from the event-by-event fluctuations observable $S\sigma$ of
net-proton distributions provides further evidence of thermalization of the hot
dense matter created in the heavy ion collisions. Further, the $\kappa\sigma^2$ and $S\sigma$ of
net-proton distributions are consistent with Lattice QCD calculations at high
energy, which also indicates thermalization of our system. The deviations of
the $\kappa\sigma^2$ and $S\sigma$ of net-proton distributions for Au+Au central collisions from
HRG model predications at low energies are not well understood. This may
result from the non-applicability of grand canonical ensemble or the appearance
of QCD critical point and chiral phase transitions at low energies. This should
be further investigated.

The experimental study of higher moments of net-proton distributions in
heavy ion collisions opens a new domain and provide an effective way for prob-
ing the bulk properties of nuclear matter. It also provide us a new way to
test the QCD theory in the non-perturbative region. We have determined the

transition temperature T_c at $\mu_B = 0$ by comparing the higher moments experimental data with the first principle lattice QCD calculations. We conclude that, $T_c = 175^{+1}_{-7}$ MeV.

In the future, we can tune the input parameters of various theories and models, such as Lattice QCD and HRG, and the output can be used to fit with our higher moments measurements to constrain fundamental parameters. This is of great significance for nuclear physics and for heavy ion collision physics research.

APPENDIX A

Derivation of Statistical Error Formula

The latest error estimation used in moment analysis can be found in ref. [114]. The following analytical error propagation formula has been proved to be overestimating the statistic errors of the moments.

The definition of various moments (M, σ, S, κ) can be written as :

$$M \quad = \quad < N >= \frac{1}{n} \sum_{i=1}^{n} N_i \tag{A.1}$$

$$\sigma \quad = \quad \sqrt{< (N- < N >)^2 >} \tag{A.2}$$

$$S \quad = \quad \frac{< (N- < N >)^3 >}{\sigma^3} \tag{A.3}$$

$$\kappa \quad = \quad \frac{< (N- < N >)^4 >}{\sigma^4} - 3 \tag{A.4}$$

where random variable N represents the measured quantity, n is the number of events in the event ensemble, N_i is the measured quantities for i^{th} event.

The Standard error propagation formula can be expressed as :

$$f \quad = \quad f(x_1, x_2...x_n) \tag{A.5}$$

$$\sigma(f) \quad = \quad \sqrt{\sum_{i=1}^{n} (\frac{\partial f}{\partial x_i})^2 \sigma_{x_i}^2} \tag{A.6}$$

The random variable f depends on other independent random variables $x_1, x_2...x_n$ and their errors are $\sigma(f)$, $\sigma_{x_1}, \sigma_{x_2}...\sigma_{x_n}$, respectively.

A.1 Mean (M)

The derivative of the mean value (M) with respected to the N_i:

$$\frac{\partial M}{\partial N_i} = \frac{\partial <N>}{\partial N_i} = \frac{1}{n} \tag{A.7}$$

Then we can get the error formula of the mean value :

$$\sigma_M = \sqrt{\sum_{i=1}^{N} (\frac{\partial <N>}{\partial N_i})^2 \sigma_{N_i}^2} = \frac{1}{n} \sqrt{\sum_{i=1}^{N} \sigma_{N_i}^2} \tag{A.8}$$

where σ_M is the error of mean value and the σ_{N_i} is the error of the ith measurements for the variable N.

A.2 Standard Deviation (σ)

The derivative of the standard deviation (σ) with respected to the N_i:

$$\frac{\partial \sigma}{\partial N_i} = \frac{1}{n\sigma}(N_i - <N>) \tag{A.9}$$

Then we can get the error formula of the standard deviation :

$$\sigma_{std} = \sqrt{\sum_{i=1}^{N} (\frac{\partial \sigma}{\partial N_i})^2 \sigma_{N_i}^2} = \frac{1}{n} \sqrt{\sum_{i=1}^{N} \{(\frac{N_i - <N>}{\sigma})^2 \sigma_{N_i}^2\}} \tag{A.10}$$

where σ_{std} is the error of standard deviation and the σ_{N_i} is the error of the ith measurements for the variable N.

A.3 Skewness (S)

Based on the definition of skewness, we have :

$$\frac{\partial S}{\partial N_i} = \frac{1}{\sigma^3}\frac{\partial < (N- < N >)^3 >}{\partial N_i} + (-3)\frac{1}{\sigma^4}\frac{\partial \sigma}{\partial N_i} < (N- < N >)^3 > \qquad (A.11)$$

By introducing the equ. (A.9) into the equ.(A.11), we get :

$$\frac{\partial S}{\partial N_i} = \frac{3}{n\sigma}[(\frac{(N_i- < N >)}{\sigma})^2 - \frac{(N_i- < N >)}{\sigma}S - 1] \qquad (A.12)$$

Thus, the error formula for skewness is :

$$\sigma_S = \sqrt{\sum_{i=1}^{N}(\frac{\partial S}{\partial N_i})^2 \sigma_{N_i}^2} = \frac{3}{n\sigma}\sqrt{\sum_{i=1}^{N}\{[(\frac{(N_i- < N >)}{\sigma})^2 - \frac{(N_i- < N >)}{\sigma}S - 1]^2\sigma_{N_i}^2\}} \qquad (A.13)$$

where σ_S is the error of standard deviation and the σ_{N_i} is the error of the ith measurements for the variable N.

A.4 Kurtosis (κ)

Based on the definition of kurtosis, we have :

$$\frac{\partial \kappa}{\partial N_i} = \frac{1}{\sigma^4}\frac{\partial < (N- < N >)^4 >}{\partial N_i} + \frac{(-4)}{\sigma^5} < (N- < N >)^4 > \frac{\partial \sigma}{\partial N_i} \qquad (A.14)$$

By introducing the equ. (A.9) into the equ.(A.14), we get :

$$\frac{\partial \kappa}{\partial N_i} = \frac{4}{n\sigma}[(\frac{N_i- < N >}{\sigma})^3 - (\kappa + 3)(\frac{N_i- < N >}{\sigma}) - S] \qquad (A.15)$$

Thus, the error formula for kurtosis is :

$$\sigma_\kappa = \sqrt{\sum_{i=1}^{N} (\frac{\partial \kappa}{\partial N_i})^2 \sigma_{N_i}^2} = \frac{4}{n\sigma} \sqrt{\sum_{i=1}^{N} \{[(\frac{N_i - <N>}{\sigma})^3 - (\kappa+3)(\frac{N_i - <N>}{\sigma}) - S]^2 \sigma_{N_i}^2\}} \tag{A.16}$$

where σ_κ is the error of standard deviation and the σ_{N_i} is the error of the ith measurements for the variable N.

A.5 Kurtosis×Variance $(\kappa\sigma^2)$

The derivative of the $\kappa\sigma^2$ with respected to the N_i can be expressed as :

$$\frac{\partial(\kappa\sigma^2)}{\partial N_i} = \sigma^2 \frac{\partial\kappa}{\partial N_i} + 2\kappa\sigma \frac{\partial\sigma}{\partial N_i} \tag{A.17}$$

The error formula for $\kappa\sigma^2$ can be written as :

$$\sigma_{\kappa\sigma^2} = \sqrt{\sum_{i=1}^{n} (\sigma^2 \frac{\partial\kappa}{\partial N_i} + 2\kappa\sigma \frac{\partial\sigma}{\partial N_i})^2 \sigma_{N_i}^2} \tag{A.18}$$

$$= \kappa\sigma^2 \times \sqrt{(\frac{\sigma_\kappa}{\kappa})^2 + (\frac{2\sigma_{std}}{\sigma})^2 + \frac{4}{\kappa\sigma} \sum_{i=1}^{n} \frac{\partial\kappa}{\partial N_i} \frac{\partial\sigma}{\partial N_i} \sigma_{N_i}^2} \tag{A.19}$$

$$= \kappa\sigma^2 \times \sqrt{(\frac{\sigma_\kappa}{\kappa})^2 + (\frac{2\sigma_{std}}{\sigma})^2} \tag{A.20}$$

where the σ_{kappa} and σ_{std} are the errors for kurtosis and standard deviation, respectively, and the σ_{N_i} is the error of the ith measurements for the variable N.

A.6 Skewness×Standard Deviation ($S\sigma$)

The derivative of the $S\sigma$ with respected to the N_i can be written as :

$$\frac{\partial(S\sigma)}{\partial N_i} = \sigma\frac{\partial S}{\partial N_i} + S\frac{\partial \sigma}{\partial N_i} \tag{A.21}$$

The error formula for $S\sigma$ is :

$$\sigma_{S\sigma} = \sqrt{\sum_{i=1}^{n}(\sigma\frac{\partial S}{\partial N_i} + S\frac{\partial \sigma}{\partial N_i})^2\sigma_{N_i}^2} \tag{A.22}$$

$$= S\sigma \times \sqrt{(\frac{\sigma_S}{S})^2 + (\frac{\sigma_{std}}{\sigma})^2 + \frac{2}{S\sigma}\sum_{i=1}^{n}\frac{\partial S}{\partial N_i}\frac{\partial \sigma}{\partial N_i}\sigma_{N_i}^2} \tag{A.23}$$

$$= S\sigma \times \sqrt{(\frac{\sigma_S}{S})^2 + (\frac{\sigma_{std}}{\sigma})^2} \tag{A.24}$$

where the σ_S and σ_{std} are the errors for skewness and standard deviation, respectively, and the σ_{N_i} is the error of the ith measurements for the variable N.

A.7 Discussion

The most important thing of our error calculations is to estimate the error for each independent measured quantity N_i, the σ_{N_i}, $(i = 1, 2..n)$.

Here, we provide two candidate methods to estimate the σ_{N_i}.

1. If $N_i = n_1^i - n_2^i$, we assume the variable n_1 and n_2 distribute as independent Poisson distributions. Then we have the error for measured N_i in each event: $\sigma_{N_i} = n_1^i + n_2^i$. For $e.g.$, the error of net-proton in each event is $\sigma_N = n_p + n_{\bar{p}}$. For this case, we ignore weak correlation between proton and anti-proton in each event due to the particle diffusion and re-scattering within the chosen phase space coverage.

2. As the each N_i, $(i = 1, 2..n)$ comes from the same intrinsic distribution, we can just simply use the standard deviation (σ) of the event-by-event distribution to replace each σ_{N_i}. Hence, we have $\sigma_{N_i} = \sigma$. Then, the above error formula for each moment can be simplified :

$$\sigma_M = \frac{\sigma}{\sqrt{n}} \tag{A.25}$$

$$\sigma_{std} = \frac{\sigma}{\sqrt{n}} \tag{A.26}$$

$$\sigma_S = \frac{3}{\sqrt{n}} \times \sqrt{\kappa + 2 - S^2} \tag{A.27}$$

$$\sigma_\kappa = \frac{4}{\sqrt{n}} \times \sqrt{\frac{< (N- < N >)^6 >}{\sigma^6} - (\kappa + 3)^2 - S^2} \tag{A.28}$$

The error for each moment calculated from method 1 should be larger than the error evaluated from method 2.

APPENDIX B

Presentation and Publication List

<u>Presentations</u>

- *Stopping Effects in U+U Collisions with a Beam Energy of 520 A MeV*
  Hadron Physics Meeting of CSR/LanZhou, Beijing, China, 03/12/2007 - 03/15/2007.

- *Selection of High Baryon Density Events from Random Orientation U+U Collisions*
  QCD and Hadronic Physics, LanZhou, China, 08/23/2007 - 08/28/2007.

- *Stopping Effects in U+U Collisions with a Beam Energy of 520 A MeV* (poster)
  20th International Conference on Ultra-Relativistic Nucleus Nucleus Collisions, India, 02/04/2008 - 02/10/2008.

- *Search for the QCD Critical Point Through Higher Moments of Net-proton Distribution*
  APS/AAPT Joint Meeting, Washington, D.C., USA, 02/13/2010 - 02/16/2010.

- *Search for the QCD Critical Point : Higher Moments of Net-proton Distribution*
  DNP Meeting, Santa Fe, New Mexico, USA, 11/02/2010 - 11/06/2010.

- *Search for the QCD Critical Point : Higher Moments of Net-proton Distribution*

Winter Workshop on Nuclear Dynamics, Winter Park, Coroladuo, USA, 02/06/2011 - 02/13/2011.

Publication List

- S. Gupta, X. F. Luo, B. Mohanty, H. G. Ritter, N. Xu, "Scale for the QCD Phase Diagram of Quantum Chromodynamics.", *Science* **332**, 1525 (2011); *arXiv: 1105.3934.*

- X. F. Luo, "Error Estimation for Moments Analysis in Heavy Ion Collision Experiment", *arXiv: 1109.0593.*

- M. M. Aggarwal *et al.* STAR Collaboration, "Higher Moments of Net-proton Multiplicity Distributions at RHIC.", *Phys. Rev. Lett.* **105**, 22302 (2010). (Principle Author: X. F. Luo, B. Mohanty, T. Nayak).

- X. F. Luo, B. Mohanty, H. G. Ritter, N. Xu, "Energy Dependence of Higher Moments for Net-proton Distributions.", *J. Phys. G: Nucl. Part. Phys.* **37**, 094061, (2010).

- X. F. Luo (for the STAR Collaboration), " Probing the QCD Critical Point with Higher Moments of Net-proton Multiplicity Distributions.", *WWND 2011 Proceedings, arXiv: 1106.2926.*

- X. F. Luo, B. Mohanty, H. G. Ritter, N. Xu, " Search for the QCD Critical Point: Higher Moments of Net-proton Multiplicity Distributions.", *CPOD*

2010 Proceedings, arXiv: 1105.5049.

- X. F. Luo, B. Mohanty, H. G. Ritter, N. Xu, " Search for the QCD Critical Point at NICA: Higher Moments of Net-proton Multiplicity Distributions.", *NICA White Paper 2011.*

- X. F. Luo, M. Shao, C. Li, H. F. Chen, " Signature of QCD Critical Point : Anomalous Transverse Velocity Dependence of Antiproton to Proton Ratio.", *Phys. Lett. B* **673**, 268-271 (2009).

- X. F. Luo, M. Shao, X. Dong, C. Li, " Nuclear Stopping and Sideward-flow Correlation from 0.35 A to 200 A GeV.", *Phys. Rev. C* **78**, 031901 (R) (2008).

- X. F. Luo, M. Shao, C. Li, " Event Selection in CSR-ETF U+U Collision.", *Chinese Physics C* **32(S2)**, 17-20 (2008).

- X. F. Luo, X. Dong, M. Shao, K. J. Wu, C. Li, H. F. Chen, X. H. Shan, " Nuclear Stopping and Collective Flow in CSR/LanZhou Energy Region.", *Quark Matter 2008 Conference Proceeding (Poster)., Indian J. Phys.* **85**, 735-740 (2011).

- X. F. Luo, X. Dong, M. Shao, K. J. Wu, C. Li, H. F. Chen, X. H. Shan, " Stopping Effects in U+U collisions with a Beam Energy of 520 MeV/nucleon.", *Phys. Rev. C* **76**, 044902 (2007).

- K. J. Wu, X. F. Luo, F. Liu, "Simulation for Elliptic Flow of U+U Collisions at CSR Energy Region in Lanzhou.", *High Energy Physics and Nuclear Physics*, **31(07)**, 617-620 (2007).

- Z. G. Xiao, X. Dong, F. Liu, X. F. Luo, K. J. Wu, H. S. Xu, W. L. Zhan," The Equation of State Study in UU Collisions at CSR, Lanzhou", *J. Phys. G: Nucl. Part. Phys.* **34**, S915-S919, (2007).

- H. Agakishiev *et al.*, STAR Collaboration. "Observation of the antimatter helium-4 nucleus.", *Nature* **473**, 353-356 (2011); [arXiv:1103.3312]

- H. Agakishiev *et al.*, STAR Collaboration. "High p_T non-photonic electron production in $p+p$ collisions at $\sqrt{s} = 200$ GeV ", *Phys. Rev. D* **83**, 52006 (2011).

- H. Agakishiev *et al.*, STAR Collaboration. "Measurements of Dihadron Correlations Relative to the Event Plane in Au+Au Collisions at $\sqrt{s_{\mathrm{NN}}} = 200$ GeV", *arXiv: 1010.0690.*

- H. Agakishiev *et al.*, STAR Collaboration. "Strange and Multi-strange Particle Production in Au+Au Collisions at $\sqrt{s_{NN}} = 62.4$ GeV", *Phys. Rev. C* **83**, 24901 (2011).

- M. M. Aggarwal *et al.*, STAR Collaboration. "Measurement of the parity-violating longitudinal single-spin asymmetry for $W^{\pm}$ boson production in polarized proton-proton collisions at $\sqrt{s} = 500$ GeV", *Phys. Rev. Lett.* **106**, 62002 (2011).

- M. M. Aggarwal *et al.*, STAR Collaboration. "Scaling properties at freeze-out in relativistic heavy ion collisions ", *Phys. Rev. C* **83**, 34910 (2010).

- M. M. Aggarwal *et al.*, STAR Collaboration. "An Experimental Exploration of the QCD Phase Diagram: The Search for the Critical Point and the Onset of De-confinement.", *arXiv: 1007.2613.*

- M. M. Aggarwal *et al.*, STAR Collaboration. "Measurement of the Bottom contribution to non-photonic electron production in p+p collisions at *sqrts*=200 GeV.", *Phys. Rev. Lett.* **105**,202301 (2010).

- M. M. Aggarwal *et al.*, STAR Collaboration. "K*0 production in Cu+Cu and Au+Au collisions at $\sqrt{s_{NN}} = 62.4$ GeV and 200 GeV.", *arXiv: 1006.1961.*

- M. M. Aggarwal *et al.*, STAR Collaboration. "Balance Functions from Au+Au, d+Au, and p+p Collisions at $\sqrt{s_{NN}} = 200$ GeV.", *Phys. Rev. C* **82**, 24905 (2010).

- M. M. Aggarwal *et al.*, STAR Collaboration. "Higher Moments of Net-proton Multiplicity Distributions at RHIC.", *Phys. Rev. Lett.* **105**, 22302 (2010).

- M. M. Aggarwal *et al.*, STAR Collaboration. "Azimuthal di-hadron correlations in d+Au and Au+Au collisions at $\sqrt{s_{NN}} = 200$ GeV from STAR.", *Phys. Rev. C* **82**, 24912 (2010).

- M. M. Aggarwal *et al.*, STAR Collaboration. "Pion femtoscopy in p+p collisions at $\sqrt{s}$=200 GeV.", *arXiv: 1004.0925.*

- B. I. Abelev *et al.*, STAR Collaboration. "Longitudinal scaling property of the charge balance function in Au + Au collisions at 200 GeV.", *Phys. Lett. B* **690**, 239 (2010).

- B. I. Abelev *et al.*, STAR Collaboration. "Charged and strange hadron elliptic flow in Cu+Cu collisions at $\sqrt{s_{NN}} = 62.4$ and 200 GeV.", *Phys. Rev.C* **81**, 44902 (2010).

References

[1] E. Rutherford, *Philosophical Magazine, Series 6*, **21**, 669-688 (1911).

[2] D. Iwanenko, *Nature*, **129**, 798 (1932); D. Iwanenko, *Nature*, **133**, 981 (1934).

[3] R. P. Feynman, *High Energy Collisions: Third International Conference at Stony Brook, N.Y. Gordon & Breach. pp. 237. ISBN 978-0677139500.* (1969).

[4] H. Fritzsch, M. Gell-Mann, *arXiv: hep-ph/0208010v1* (2002).

[5] G. Dissertori, I. Knowles, and M. Schmelling, *Quantum Chromodynamics - High Energy Experiments and Theory.*, Oxford Universidy Press (2003).

[6] D. Gross and F. Wilczek, *Phys. Rev. Lett.* **30**, 1343 (1973); H. Politzer, *Phys. Rev. Lett.* **30**, 1346 (1973).

[7] S. Bethke, *arXiv: hep-ph/0908.1135* (2009).

[8] R. Gupta, *arXiv: hep-lat/9807028* (1998).

[9] URL http://en.wikipedia.org/wiki/Color_confinement.

[10] A. Pich, *arXiv: hep-ph/9505231* (1995).

[11] M. A. Stephanov, *PoSLAT2006* **024** (2006),*arXiv:hep-lat/0701002* (2006); M. A. Stephanov, *Int. J. Mod. Phys. A* **20**, 4387 (2005).

[12] M. Cheng, *Phys. Rev. D* **74**, 054507 (2006).

[13] Y. Aoki *et al.*, *Phys. Lett. B* **643**, 46 (2006).

[14] Y. Aoki *et al.*, *Nature* **443**, 675 (2006).

[15] S. Ejiri, *Phys. Rev. D* **78** 074507 (2008); E. S. Bowman, J. I. Kapusta, *Phys. Rev. C* **79**, 015202 (2009).

[16] M. A. Stephanov, *Prog. Theor. Phys. Suppl.* **153**, 139 (2004).

[17] X. F. Luo *et al.*, *Phys. Lett. B* **673**, 268 (2009); B. Mohanty, *Nucl. Phys. A* **830**, 899C (2009); M. M. Aggarwal, *arXiv:1007.2613* (2010).

[18] Z. Fodor and S. D. Katz, *Journal of High Energy Physics* **0404**, 50 (2004).

[19] M. M. Aggarwal, *arXiv:1007.2613* (2010); B. I. Abelev *et al.* STAR Collaboration, *Phys. Rev. C* **81**, 024911 (2010); STAR Internal Note - SN0493, 2009.

[20] Z. Fodor, *PoS LATTICE 2007* **011** (2007), *arXiv:0711.0336* (2007).

[21] K. Kanaya, *PoS LATTICE 2010* **012** (2010), *arXiv:1012.4247* (2010).

[22] G. Endrodi, *PhD thesis*, *arXiv:1104.3730* (2011).

[23] S. Ejiri, *PoS LATTICE 2008* **002** (2008), *arXiv:0812.1534* (2008).

[24] Z. Fodor, S. D. Katz,*Phys. Lett. B* **534**, 87 (2002);.

[25] Philippe de Forcrand and O. Philipsen *Nucl. Phys. B* **642**, 290 (2002).

[26] C. R. Allton1, *et al.*, *Phys. Rev. D* **66**, 074507 (2002); R. V. Gavai, S. Gupta, *Phys. Rev. D* **68**, 034506 (2003).

[27] M. Asakawa *et al.*, *Phys. Rev. Lett.* **103**, 262301 (2009).

[28] A. Barducci, R. Casalbuoni, S. De Curtis, R. Gatto and G. Pettini, *Nucl. Phys. A* **504**, 668 (1989); *Phys. Rev. D* **41**, 1610 (1990).

[29] A. Barducci, R. Casalbuoni, G. Pettini and R. Gatto, *Phys. Rev. D* **49**, 426 (1994).

[30] AJ. Berges and K. Rajagopal, *Nucl. Phys. B* **538**, 215 (1999).

[31] M. A. Halasz, A. D. Jackson, R. E. Shrock, M. A. Stephanov and J. J. M. Verbaarschot, *Phys. Rev. D* **58**, 096007 (1999).

[32] O. Scavenius, A. Mocsy, I. N. Mishustin and D. H. Rischke, *Phys. Rev. C* **64**, 045202 (2001).

[33] N. G. Antoniou and A. S. Kapoyannis, *Phys. Lett. B* **563**, 165 (2003).

[34] Y. Hatta and T. Ikeda, *Phys. Rev. D* **67**, 014028 (2003).

[35] A. Barducci, R. Casalbuoni, G. Pettini and L. Ravagli, *Phys. Rev. D* **72**, 056002 (2005).

[36] S. Roessner, C. Ratti and W. Weise, *arXiv:hep-ph/0609281* (2006).

[37] Z. Fodor and S. D. Katz, *Journal of High Energy Physics* **0203**, 014 (2002).

[38] S. Ejiri, C. R. Allton, S. J. Hands, O. Kaczmarek, F. Karsch, E. Laermann and C. Schmidt, *Prog. Theor. Phys. Suppl.* **153**, 118 (2004).

[39] R. V. Gavai and S. Gupta, *Phys. Rev. D* **71**, 114014 (2005).

[40] R. V. Gavai and S. Gupta, *Phys. Rev. D* **78**, 114503 (2008).

[41] P. de Forcrand and O. Philipsen, *arXiv:hep-ph/0301209* (2003); *Nucl. Phys. B* **673**, 170 (2003); *Nucl. Phys. Proc. Suppl.* **129**, 521 (2004).

[42] J. D. Bjorken, *Phys. Rev. D* **27**, 140 (1983).

[43] P. Braun-Munzinger, K. Redlich and J. Stachel, *arXiv:nucl-th/0304013* (2003).

[44] A. Andronic, P. Braun-Munzinger and J. Stachel, *Nucl. Phys. A* **772**, 167-199 (2005). [*nucl-th/0511071* (2006)].

[45] J. Adams, *et al.*, STAR Collaboration, *Nucl. Phys. A* **757**, 102-183 (2005). [*arXiv:nucl-ex/0501009* (2005)].

[46] Z. B. Tang *et al.*, *Phys. Rev. C* **79**, 051901 (2009).

[47] M. Shao *et al.*, *J. Phys. G: Nucl. Phys.* **37**, 085104 (2010).

[48] Sergei A. Voloshin, Arthur M. Poskanzer, R. Snellings, *arXiv:0809.2949* (2008).

[49] P. F. Kolb and U. Heinz, *arXiv:nucl-th/0305084* (2003).

[50] M. D. Oldenburg, *J. Phys. G: Nucl. Phys.* **31**, S437-S442 (2005). [*arXiv:nucl-ex/0412001*] (2004).

[51] Sergei A. Voloshin , *J. Phys. G: Nucl. Phys.* **34**, S883-S886 (2006). [*arXiv:nucl-ex/0701038*] (2004).

[52] S. S. Shi, *Nucl. Phys. A* **830**, 187c-190c (2009). [*arXiv:0907.2265*] (2009).

[53] C. Adler, *et al.*, STAR Collaboration, *Phys. Rev. Lett.* **89**, 202301 (2002).

[54] C. Y. Wong, *Introduction to High-Energy Heavy-Ion Collisions.*, World Scientic Publishing Co. Pte. Ltd. (1994).

[55] B. I. Abelev, *et al.*, *Phys. Rev. C* **79**, 034909 (2009).

[56] M. M. Aggarwal *et al.* (STAR Collaboration), *Phys. Rev. Lett.* **105**, 022302 (2010).

[57] R. V. Gavai and S. Gupta, *Phys. Lett. B* **696**, 459 (2011).

[58] F. Karsch and K. Redlich, *Phys. Lett. B* **695**, 136 (2011).

[59] Y. Hatta and M. A. Stephanov, *Phys. Rev. Lett.* **91**, 102003 (2003).

[60] M. A. Stephanov *et al.*,*Phys. Rev. D* **60**, 114028 (1999); B. Berdnikov and K. Rajagopal, *Phys. Rev. D* **65**, 105017 (2000).

[61] M. A. Stephanov, *Phys. Rev. Lett.* **102**, 032301 (2009).

[62] C. Athanasiou *et al.*, *Phys. Rev. D* **82**, 074008 (2010).

[63] M. Harrison, T. Ludlam, S. Ozaki, *Nucl. Instrum. Methods A* **499**, 235 (2003).

[64] A. Franz, *et al.*, *Nucl. Instrum. Methods A* **566**, 54 (2006).

[65] K. H. Ackermann, *et al.*, *Nucl. Instrum. Methods A* **499**, 624 (2003).

[66] From my colleague at LBNL Alex Schmah and his wife Maria : 3D Picture of STAR Detector.

[67] A. Shabetai, *Eur. J. Phys. C* **49**, 169 (2007).

[68] J. Kapitan, *arXiv:0806.2266* (2008).

[69] F. Simon, *arXiv:0811.2432* (2008).

[70] M. Beddo, *et al.*, *Nucl. Instrum. Methods A* **499**, 725 (2003).

[71] C. E. Allgower, *et al.*, *Nucl. Instrum. Methods A* **499**, 740 (2003).

[72] M. Shao, *et al.*, *Nucl. Instrum. Methods A* **558**, 419 (2006).

[73] X. Dong, *AIP Conf. Proc.* **865**, 332 (2006).

[74] W. J. Llope, *Nucl. Instrum. Methods A* **241**, 306 (2005).

[75] M. Anderson, *Nucl. Instrum. Methods A* **499**, 659 (2003).

[76] Z. Tang, Ph.D. Thesis, *University of Science and Technology of China* (2009).
http://drupal.star.bnl.gov/STAR/system/files/Tang Zebo.pdf.

[77] S. Eidelman, *Phys. Lett. B* **592**, 1 (2004).

[78] X. Dong, *arXiv:nucl-ex/0509011* (2005).

[79] Z. Xu, *et al.*, *arXiv: nucl-ex/0411001* (2004).

[80] Y. Xu, *et al.*, *arXiv:0807.4303* (2008).

[81] C. Adler, *et al.*, STAR Collaboration, *Phys. Rev. C* **66**, 61901 (2002).

[82] STAR-TOF software documentation.
http://drupal.star.bnl.gov/STAR/system/files/TOFSoftware.2.pdf.

[83] X. P. Zhang, PhD thesis (2010).
http://drupal.star.bnl.gov/STAR/files/xpzhangthesisnew.pdf.

[84] W.J. Llope, *et al.*, *Nucl. Instrum. Methods A* **522**, 252 (2004).

[85] M. Shao, *et al.*, *Nucl. Instrum. Methods A* **492**, 344 (2002).

[86] M. Shao, *et al.*, *Meas. Sci. Technol.* **20**, 025102 (2009).

[87] William Mendenhall, Robert J. Beaver, Barbara M. Beaver, *Introduction to probability and statistics* (2006), twelfth edition, THOMSON BROOKS/COLE.

[88] A. Hald, *International Statistical Review* **68(2)**, 137-153 (2000).

[89] http://en.wikipedia.org/wiki/Skewness.

[90] http://en.wikipedia.org/wiki/Kurtosis.

[91] M. Cheng, *et al.*, *Phys. Rev. D* **79**, 074505 (2009).

[92] A. Tawfik, *Phys. Rev. D* **71**, 054502 (2005).

[93] Szabolcs Borsanyi, *et al.*, *arXiv:1012.5215* (2010).

[94] P. Huovinen, P. Petreczky, *Nucl. Phys. A* **837**, 26-53 (2010).

[95] J. Adams *et al.* STAR Collaboration, *Phys. Rev. C* **71**, 064906 (2005).

[96] B. I. Abelev *et al.*, STAR Collaboration, *Phys. Rev. Lett.* **103**, 092301 (2009).

[97] M. Bleicher *et al.*, *J. Phys. G: Nucl. Phys.* **25**, 1859 (1999).

[98] Z.W. Lin *et al.*, *Phys. Rev. C* **72**, 064901 (2005).

[99] A. Kisiel *et al.*, *Comput. Phys. Commun.* **174**, 669 (2006).

[100] M. Gyulassy *et al.*,*Comput. Phys. Commun.* **83**, 307 (1994).

[101] Alex Schmach, *Talk at STAR UCLA Analysis Meeting* (2010).

[102] R. S. Hollis, *Journal of Physics: Conference Series* **5**, 46-54 (2005).

[103] P. Shukla, *arXiv:nucl-th/0112039* (2001).

[104] Michael L. Miller, Klaus Reygers, Stephen J. Sanders and Peter Steinberg, *Annu. Rev. Nucl. Part. Sci.*, **57**, 205-43 (2007). [*arXiv:nucl-ex/0701025*] (2007).

[105] S. S. Adler *et al.*, *Phys. Rev. C* **71**, 034908 (2005).

[106] Christian Lippmann, *arXiv:1101.3276* (2011).

[107] D. E. Groom and S.R. Klein,
URL http://pdg.lbl.gov/2000/passagerpp.pdf.

[108] X. F. Luo *et al.*, *J. Phys. G: Nucl. Phys.* **37**, 094061 (2010).

[109] M. A. Stephanov, *arXiv:1104.1627* (2011).

[110] J. Cleymans *et al.*, *Phys. Rev. C* **73**, 034905 (2006).

[111] M. M. Aggarwal *et al.*, STAR Collaboration, *arXiv:1008.3133* (2009).

[112] H. Heiselberg,*Physics Reports* **351**, 161 (2001).

[113] S. Jeon and V. Koch, *hep-ph/0304012* (2003); V. Koch, *arXiv:0810.2520* (2008).

[114] X. F. Luo, *arXiv:1109.0593* (2011).